

STEREO 3D-SMS MICROSCOPY OF LARGE SAMPLE VOLUME

Dissertation

zur Erlangung des mathematisch-naturwissenschaftlichen Doktorgrades

”Doctor rerum naturalium”

der Georg-August-Universität Göttingen

im Promotionsprogramm Physik (PROPHYS)

der Georg-August University School of Science (GAUSS)

vorgelegt von

Haugen Mittelstädt, geb. Grefe

aus Martfeld

Göttingen, 2018

Betreuungsausschuss

PD Dr. Alexander Egner, Laser-Laboratorium Göttingen e.V.

Prof. Dr. Jörg Enderlein, III. Physikalisches Institut, Universität Göttingen

Mitglieder der Prüfungskommission

Referent: PD Dr. Alexander Egner, Laser-Laboratorium Göttingen e.V.

Korreferent: Prof. Dr. Jörg Enderlein, III. Physikalisches Institut, Universität Göttingen

Weitere Mitglieder der Prüfungskommission:

Prof. Dr. Hans Hofsäss, II. Physikalisches Institut, Universität Göttingen

Prof. Dr. Wolfram Kollatschny, Institut für Astrophysik, Universität Göttingen

Dr. Florian Rehfeldt, III. Physikalisches Institut, Universität Göttingen

Prof. Dr. Tim Salditt, Institut für Röntgenphysik, Universität Göttingen

Tag der mündlichen Prüfung:

Contents

1	Introduction	1
2	Background of super resolution microscopy	7
2.1	Fluorescence	7
2.1.1	Basic principle	7
2.1.2	Characteristics of switchable fluorophores	10
2.1.3	Emission anisotropy of a dipole	13
2.2	From signal to image - point spread function and resolution	14
2.3	Localization and separation to gain super resolution	16
2.3.1	Super resolution in two dimensions	16
2.3.2	State of the art 3D methods in SMS microscopy	20
2.3.3	Relation of numerical aperture and focal depth	23
3	Stereo 3D-SMS microscopy	25
3.1	Fundamental concept	25
3.1.1	From 2D plane to 3D space by spatial imaging	25
3.1.2	Achieving high isotropic resolution with spatial imaging	29
3.2	Further characteristics	30
3.2.1	Focal shift	30
3.2.2	Diffusion of particles	31
3.3	Practical realization	33
3.3.1	Combination of objectives	33
3.3.2	Mounting of the sample	35
3.3.3	Index matching cover glass	38
3.3.4	Illumination and detection	39
3.3.5	Conversion factor between photons and camera counts	42
3.3.6	Electronic control of the setup	42
3.4	Samples and buffer	45
3.4.1	Fluorescent beads	45
3.4.2	Cells and their preparation	45

3.4.3	Buffer solution for SMS imaging	45
4	Data analysis framework	49
4.1	Simulation of artificial data	49
4.2	Image analysis - from raw data to a 3D-image	50
4.2.1	2D localization of the emitter position	50
4.2.2	Determining the transformation parameters	51
4.2.3	Correlation in case of multiple emitter	52
4.2.4	Final calculation of the most likely emitter position	53
4.2.5	Following a track	53
5	Stereo 3D-SMS: Characterization and first imaging examples	55
5.1	Comparison of the theoretically calculated and the actually measured PSF	55
5.2	Stability of the setup	58
5.3	Focal shift of the bottom objective lens	59
5.4	Calculating the Electron Multiplying CCD (EMCCD) camera conversion factor	61
5.5	Theoretical simulation of the setup capabilities	61
5.6	Experimental quantification of the setup capability	64
5.7	Particle tracking for viscosity measurement	68
5.8	Measurement of different cell structures	70
5.8.1	Nuclear lamins - surrounding the cellular nucleus	71
5.8.2	Vimentin filaments - part of the cytoskeleton	76
5.8.3	Mitochondrion organelle - power plant of the cell	79
5.8.4	Protein gp210 in the nuclear pore complex - gateway of the nucleus	81
6	Discussion and further developments	85
	List of abbreviations	92
	List of Figures	94
	List of Tables	96
	Bibliography	97

Chapter 1

Introduction

The functionality of the human body and with it many of its diseases are based on single cells or even on single cellular components. It is therefore essential to gain insight into the intra- and intercellular processes in order to understand the overall physiological functions and the mechanisms of ailments. Among the many techniques which are available for investigation, taking microscopic images of regions of interest plays a major role.

Optical fluorescence microscopy is a powerful tool since it augments the advantages of optical microscopy, which are non-invasive imaging of the inside of sufficiently transparent samples, with the high specificity of molecular fluorescence labeling. This is in contrast to, for example, electron microscopy, which is limited to measuring ultra-thin slices, or atomic force microscopy which provides only information about the sample surface.

The microscope's optical resolution determines the smallest structure size which can be distinguished in the image. In order to be able to visualize for example small cellular structures like single filaments or record molecular transport processes, a resolution in the range of typically several tens of nanometers or even better is needed. Unfortunately, light of wavelength λ , emitted by a point source and imaged by a lens, is always detected as a blurred spot. Adjacent objects which are closer than $d = \lambda/2n \sin \alpha$ cannot be separated since their images are blurred by diffraction into a single pattern. At this, n is the refractive index of the medium and α is half the opening angle of the objective lens. Accordingly, it is not possible to focus visible light to a spot size smaller than 200 nm laterally and 400 to 700 nm axially.

This diffraction barrier was postulated by Émile Verdet [1], Ernst Abbe [2] and Lord Rayleigh [3] at the end of the 19th century and limited the resolution for all far-field light microscopes until the 1990s. 4Pi microscopy [4] and I⁵M [5] improved the resolution in axial direction up to a factor of 7 by using opposing objective

lenses coherently. Still, this does not overcome the fundamental limitations due to the wave characteristics of light.

In the last decades, super resolution imaging techniques have been established which overcome this diffraction barrier. A review by Stefan W. Hell gives a comprehensive overview and is recommended for a deeper insight [6]. The key element in order to distinguish fluorescent objects less than 200 nm apart is the on and off switching of their signal such that it can be separated in space and time. This typically requires specific fluorescent molecules which can be transferred resp. switched between a fluorescent on state and a dark off state.

The available switching variants are manifold. Most basic is the switching between a bright singlet S_1 and a dark ground S_0 electronic state. Alternatively, the molecule can be transferred between an excitable on state and a non-excitable off state, for example by a long lasting electronic triplet state or a state generated by chemical bonding. The mechanism used depends on the actual microscopy concept.

In order to increase the resolution well beyond the diffraction limit there are two complementary approaches. Either the region in which fluorescent molecules are in their on state is actively controlled by targeted switching, or single molecules at random positions are stochastically switched between on and off and their location is determined subsequently.

Targeted switching is used in methods such as stimulated emission depletion (STED) [7], saturated pattern excitation microscopy (SPEM) [8], saturated structured illumination microscopy (SSIM) [9] and reversible saturable/switchable optically linear fluorescence transition (RESOLFT) [10]. For STED in particular the fluorescence excitation, induced by a diffraction-limited focused beam, is restricted in space by a second overlaid beam that features a central zero intensity area. This second beam de-excites the molecules to the electronic ground state, only at the zero intensity centre fluorescence is still allowed. The extent of that defined area scales inversely with the square root of the applied STED intensity and is not limited by the diffraction barrier anymore. Within biological samples resolutions of about 20 nm full width at half maximum (FWHM) in the focal plane can be reached [11]. Stochastic switching is used in the Single Marker Switching (SMS) schemes. Depending on the applied switching mechanism they are referred to as photo-activated localization microscopy (PALM) [12], stochastic optical reconstruction microscopy (STORM) [13], photo-activation localization microscopy with independently running acquisition (PALMIRA) [14], ground state depletion microscopy followed by individual molecule return (GSDIM) [15] and variants thereof. The probability for

two fluorophores to be emitted at the same time within a diffraction limited volume has to be negligible. Therefore, the fraction of stochastically switched molecules in the on state needs to be restricted sufficiently. The burst of N photons, before the molecule subsequently transfers to the dark state, is detected as a diffraction limited pattern, spatially separated from the spots of other molecules. The centroid can be localized with a precision much better than the diffraction limit and scales with \sqrt{N} . The hereby determined position is registered in a position histogram. The succession of switching on, emitting/detecting photons and switching off of random fluorescent molecules needs to be repeated a sufficient number of times in order to achieve a detailed image of the sample. Typical resolutions are in the range of several 10 nm FWHM in the focal plane [16, 17].

Both the targeted and stochastic approach need adaptations in the optics and/or light sources of the microscope setups. An alternative strategy to overcome the diffraction barrier is to analyse the independent stochastic intensity fluctuations of fluorescent emitters in the super-resolution optical fluctuation imaging (SOFI) concept [18]. For this, just a short video of the sample with labels switching repeatedly and independently between a fluorescent and a non-fluorescent state is required. The cumulant of the original pixel time series, related to the correlation function, gives the pixel value of the final SOFI image, calculable up to different orders. Non-correlated fluctuations cancel each other out whereby only highly correlated fluctuations remain. The resolution improvement depends on the order of cumulant reached which again requires i.a. high signal intensities. A 5-fold improvement in spatial resolution beyond the diffraction barrier can typically be achieved. Since cells in their natural environment have a distinct spatial extension, resolution increases not only in two, but in all three spatial dimensions is indispensable to super-resolve their three-dimensional (3D) structure. The SOFI concept is intrinsically three-dimensional by taking a video z -stack and the STED technique of depletion can equally be extended to the axial direction [19, 20]. In contrast the expansion of the SMS-based techniques to the third dimension is typically realized by breaking the axial symmetry of the detection point spread function (PSF) [16, 21–23]. By using two opposing objective lenses in a 4Pi like geometry the detection efficiency can be increased twofold, improving the resolution by a factor of $\sqrt{2}$. Interference between the signals detected through both lenses increases the axial resolution even further, resulting in an overall resolution of about 6 nm FWHM in the axial and 8–22 nm in the lateral direction. However, such methods are restricted to thin layers which are in the range of about 0.25 μm and 1 μm

for the interferometric PALM (iPALM) [24] and the 4Pi-SMS [17] implementation respectively. The restriction is caused by the limited focal length of the required high numerical objective lenses. Recently with the whole-cell 4Pi single-molecule switching nanoscopy (W-4PiSMSN) setup the 4Pi-SMS scheme is optimized i.a. by deformable mirrors such that whole cells along a 10 μm axial range can be imaged with isotropic resolution [25]. Since the focal depth of the high numerical aperture (NA) objective lens is still limited to about 1.2 μm the concatenation of optical slices is necessary.

A new concept for super resolution imaging is needed which provides a much greater axial range, preferably fully isotropic. In this dissertation a stereo three-dimensional Single Marker Switching (Stereo 3D-SMS) microscope is presented which is capable to image large sample volumes.

Multiple objective lenses image the same emitter from different perspectives which are not on the same optical axis. Similar to the concept of stereo view the spatial position of the emitter can be calculated from the respective two-dimensional (2D) detection patterns. In order to optimize the detection efficiency and to achieve an isotropic resolution over a great volume four objective lenses are used simultaneously, arranged in a tetrahedron like manner. This stereo SMS concept applies the basic principle of localizing the detection patterns even for the expansion to the third dimension and has no need for any PSF modifications.

The dissertation covers the whole development process from the plain idea towards the first applications with the following main points:

- Conceiving an implementation of the stereo view procedure.
- Simulation of the expected capabilities in terms of resolution and spatial volume.
- Computer aided design of the setup.
- Programming the control of the electronic devices.
- Development of the concept as well as the related algorithms to generate a 3D image from the measured raw data.

The thesis in hand starts with the theoretical background of fluorescent imaging and super resolution. Then, the implementation of the experimental setup is presented. Beside the technical components and the light paths, this also contains the electronic control and the sample as well as the buffer preparation. Afterwards, the

concept for the image analysis and the simulation of artificial data for determining the capabilities of the setup are explained in detail. Next, the theoretical and experimental results are presented. Finally, the discussion of the results and the whole setup is adjoined along with an outlook to possible advancements.

Chapter 2

Background of super resolution microscopy

2.1 Fluorescence

Several advanced microscopy techniques in the life sciences are based on fluorescence contrast, which offers inter alia high specificity and sensitivity. As biological matter is reasonably transparent for visible light and is hardly damaged by it, *in vivo* and *in vitro* measurements are possible without radical changes to the cells or their environment. This is, for example, in contrast to atomic force microscopy which is only capable to measure at the sample surface or electron microscopy which uses harmful radiation and typically requires the sample to be cut into ultra-thin slices. In addition, all methods that circumvent the diffraction limit by means of optically switchable transitions are based on fluorescence contrast. A detailed knowledge of the principles underlying fluorescence is therefore essential for the understanding of this thesis [26, Ch. 3].

2.1.1 Basic principle

The processes involved in fluorescence can be well illustrated by a Perrin-Jablonski diagram. The diagram shown in figure 2.1a depicts the ground and the first excited singlet electronic states (S_0 , S_1) and the triplet state (T_1) of a fluorescent molecule together with their vibrational levels. Following Hund's rule the triplet state has a lower energy than that of the corresponding singlet state. Higher order electronic states are not shown, as they are not needed to point out the basic principles.

At room temperature and in thermal equilibrium most of the molecules are in their lowest vibrational energy level of S_0 according to Boltzmann's law. By absorbing a photon of suitable energy, the molecule is excited into S_1 . According to

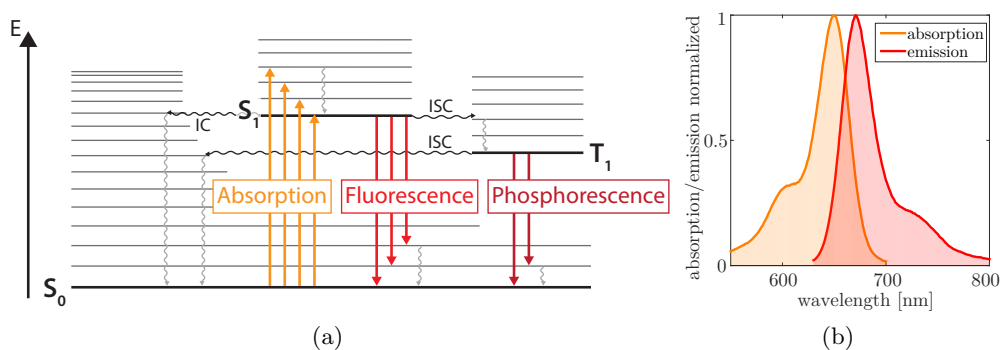


Figure 2.1: (a) The Perrin-Jablonski diagram illustrates the electronic states of a molecule and the possible transitions between them. The absorption of a photon brings the molecule to a higher singlet state S_1 . From there it can either relax to the ground state S_0 by radiative fluorescence or non-radiative internal conversation (IC). Alternatively, it can go to the triplet state by intersystem crossing (ISC) from where radiative phosphorescence is possible. The ISC is marked with black wavy arrows while the non-radiative vibrational relaxation inside the electronic states is marked by gray wavy arrows.(b) The normalized absorption (orange) and emission spectra (red) for the fluorescent dye Alexa Fluor 647 is shown. The red shift of the emission with respect to the excitation is referred to as Stokes shift and enables spectral separation.

the Franck-Condon principle, the nuclei remain stationary during this transition since it takes place on much shorter time scales (about 10^{-15} s) than molecular vibrations. Hence the molecule is initially excited into one of the higher vibronic states and then relaxes to the lowest vibrational level of S_1 . From there, three spontaneous processes are possible: fluorescence, internal conversation (IC) and intersystem crossing (ISC).

fluorescence

The transition from S_1 to S_0 by the spontaneous emission of a photon is called fluorescence. Since the transition can take place into one of the various vibrational levels of S_0 , the emission is spectrally broad, see figure 2.1a. As already mentioned, the relaxation mostly occurs from the lowest vibrational level of S_1 , which is why its characteristics are mostly independent from the excitation wavelength. Further, the fluorescence spectrum is shifted to longer wavelengths resp. lower energy as compared to the excitation spectrum, due to the energy loss by the vibrational relaxation. This effect is called Stokes shift and had been observed well before the explanation indicated by the

Perrin-Jablonski diagram was found.

internal conversion (IC)

The molecule can return to a lower state by IC without emitting a photon, for example, caused by collisions. The size of the energy gap between S_1 and S_0 depends on the specific molecule. The related probability that this process takes place may be in the same order of magnitude as fluorescence and intersystem crossing.

intersystem crossing (ISC)

The non-radiative transition between two electronic states of different spin multiplicity, e.g. from S_1 to T_1 , is called intersystem crossing (ISC). Although the transition between states of different multiplicity is in principle forbidden, it can nevertheless occur due to spin-orbit coupling. The probability for ISC can even become high enough that with time constants of up to 10^{-7} – 10^{-9} s it can compete with the other two pathways. Relaxation from T_1 to S_1 can be either radiative or non-radiative, where the radiative transition is called phosphorescence. Usually the non-radiative de-excitation predominates over phosphorescence.

The typical lifetime of S_1 is in the range of 10^{-10} – 10^{-7} s and much shorter than that of T_1 (10^{-6} – 10 s). Therefore, the occupation of the triplet state can lead to prolonged dark times without fluorescence. The transition probabilities observed for a specific molecule do not only depend on the molecule itself but also on its environment like the surrounding medium.

In addition to the transitions presented here, other processes may also occur, some of which photochemically destroy the fluorophore. This photobleaching seems to rely mainly on interactions between the excited fluorescent molecule and molecular oxygen [27, Ch. 39]. The amount of oxygen in the surrounding media and hence the photobleaching probability can be reduced by the use of specific buffers (section 3.4.3).

Typically a fluorophore emits several fluorescent photons before it transits to the long-living triplet state or photobleaches. The number of photons N , within such a burst, depends on the probability distribution of all possible transition pathway [28]. For a good fluorophore with a high quantum yield the internal conversion can be neglected. If the rate constants for the emission of a photon and the transition into one of the dark states are denoted as k_{fl} , k_{dark} respectively, the probability to

enter a dark state at each excitation/relaxation cycle then calculates to:

$$p = \frac{p_{\text{dark}}}{p_{\text{dark}} + p_{\text{fl}}} = \frac{k_{\text{dark}}}{k_{\text{dark}} + k_{\text{fl}}} \quad (2.1)$$

and the probability P for a molecule to emit N photons before getting optically dark follows a geometric distribution:

$$P(N) = p(1 - p)^N \quad (2.2)$$

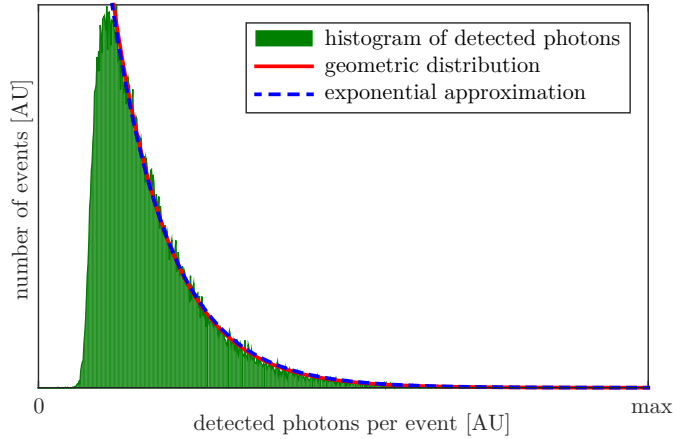


Figure 2.2: The histogram of the number of detected photon for about 10^6 events shows a geometric distribution. In a good approximation the slope can be estimated as an exponential decay. The gap at lower photon numbers arises from a detection threshold which is used to separate signal and noise.

In SMS microscopy the detected image of a burst is referred to as an event. An exemplary histogram of the number of photons in about 10^6 of these events is shown in figure 2.2. The gap at low photon numbers arises from the detection threshold which is used to distinguish between signal and noise. In the continuous approximation the geometric distribution follows an exponential decay.

2.1.2 Characteristics of switchable fluorophores

The basic physical principles presented in the previous section apply to all fluorophores. In recent decades new types of fluorophores have been reported, which can be transferred between states that differ in their fluorescence properties. By taking advantage of this state switching capability it is possible to bypass the diffrac-

tion limit in fluorescence microscopy. How this is achieved in SMS microscopy has already been mentioned briefly in the introduction and is explained in more detail in chapter 2.3.

Switching between different fluorescence properties can be realized in various ways. Therefore various classes of photoswitches exist which differ in one or more characteristics:

For example photoswitching can be triggered by the absorption of a photon or by chemical reaction. Photoswitches can also differ with respect to the underlying switching mechanism. In *cis-trans* isomerization, the spatial position of two substituents in relation to a reference plane within the molecule changes [29]. For the use as a switchable fluorophore one configuration can be optically bright, while the other is optically dark. Caged fluorophores, however, are initially in a caged dark state [30]. Illumination with light of the appropriate wavelength causes the cage to break up and the molecule is able to emit photons until it bleaches. Alternatively, the switching can also be caused by the formation of radicals, which has for example been shown for rhodamines [31].

Also, the fluorescent property which is switched can be different. Many fluorophores switch between an optical bright (on) and dark (off) state, but they can also change their emission wavelength, as for example photoshifting fluorophores [32, 33]. Moreover, the fluorescent properties can be either switched reversible or non-reversible. There are also different types of fluorophores, e.g. organic molecules or fluorescent proteins.

All these different characteristics determine to what extent the dyes can be used for sub-diffraction imaging. To decide which fluorophores are best suited for SMS microscopy, it is necessary to specify the most important parameters.

Number of photons per switching cycle

A large number of emitted photons per switching cycle improves the localization precision and thus the resolution of the image.

Duty cycle

The temporal separation of molecules within a diffraction-limited range is the basis for super-resolution in SMS microscopy. Even if a single molecule emits an extremely high number of photons the SMS scheme will not work if adjacent fluorophores cannot be distinguished. In most cases, the aim is to keep the time fraction a molecule is in its on-state, the duty cycle, as small as possible, as a duty cycle of $1/F$ allows for a maximum of F fluorophores

within a diffraction limited range. Following the Nyquist sampling criteria, the duty cycle therefore also limits the maximal achievable resolution [34].

Intensity ratio between the fluorescent signal in the on and the off states.

In addition to the photon number and the duty cycle, there are further parameters which influence the image quality. One is the intensity ratio between the fluorescent signal in the on and the off states, described by the on-off contrast. For a clear distinction between these states a high on-off ratio is required.

Number of switching cycles

Another important parameter is the number of switching cycles a molecule can undergo before it is bleached as, if desired, the signal of several switching cycles may be combined in a reasonable way in order to increase the localization precision.

Many of these parameters depend on each other. For example, a large number of photons per switching cycle requires a certain amount of on-state time which increases the duty cycle if the off-time does not increase accordingly. The most suitable combination of fluorophore parameters for SMS-Microscopy depends also on the specific application. As an example: For the examination of sparse structures, such as nuclear pores, a high on-switching rate is desirable in order to shorten the acquisition time. However, in case of a densely labeled sample or when using a low aperture objective lens, which is equivalent to a large diffraction limited area, it may be advantageous to reduce the on-switching rate.

Overall, it has been observed that switchable organic dyes are in most cases optimally suited for SMS microscopy. This applies in particular to Cy5 or the chemically almost identical Alexa Fluor 647 [35] which exhibit a great overall performance including a high number of photons per switching event and a low duty cycle. The underlying switching mechanism of these molecules is the light-induced reaction with surrounding thiols or phosphines. Illumination with red light leads to a binding of these substances whereby the fluorophore is converted into a non-fluorescent state. After some time, the adduct breaks up again and the fluorophore returns to the bright state. The on switching rate can be increased by exposure to ultraviolet (UV) light. Note that the rate constants for on k_{on} and off switching k_{off} add to the previous mentioned rate constants of the other photophysical pathways, equation 2.1.

Not only because of the required thiols or phosphines is the composition of the

imaging buffer crucial for the switching behavior of Alexa Fluor 647 and Cy5. An oxygen scavenger system is also necessary, as otherwise the fluorophores may get photobleached too early by reacting with oxygen solved in the medium.

Due to the advantages mentioned here, Alexa Fluor 647 is used for the microscopy technique presented below to obtain high-quality super-resolution images.

2.1.3 Emission anisotropy of a dipole

Most fluorophores interact with the light field primarily through their electric transition dipole moment. Therefore, the emission from a fluorophore can be usually treated as a Hertzian dipole whose orientation is associated with that of the emitting molecule. The orientation of a molecule is a parameter [36] which can provide useful information about the molecule itself and its environment, for example order parameters in a lipid bilayer [26, Ch. 7].

The dipole emission leads to an asymmetric angular intensity distribution. Similar to the classical oscillating dipole, the intensity field is proportional to $\sin^2 \beta$, where β is the angle between the dipole moment $\vec{\mu}$ and the Poynting vector \vec{s} of the emitted light (fig. 2.3). The intensity field is rotationally symmetric about the direction of the dipole moment.

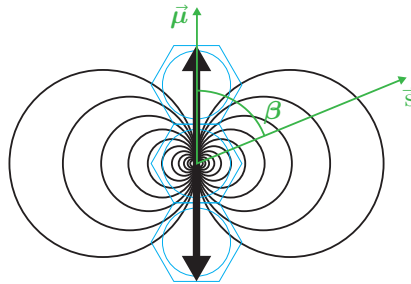


Figure 2.3: Intensity distribution of the emission from a dipole.

The molecule is sketched in blue, the black arrow indicates the dipole moment $\vec{\mu}$, the black rings correspond to lines of equal field intensity and \vec{s} corresponds to the Poynting vector exhibiting an angle β with respect to the dipole moment (based on [36]).

For detection, the fluorescence is collected by an objective lens over an extended solid angle, which depends on the aperture angle of the lens. Therefore, the objective lens integrates over the corresponding range of Poynting vectors and consequently the collected intensity depends on the angle of the dipole moment with

respect to the objective lens' optical axis. This allows to determine the underlying molecular orientation. For example, the collected fluorescence intensity reaches a minimum if the transition dipole is parallel to the direction of the objective lens' optical axis.

Typically the detected emission characteristics are blurred due to rotation of the molecule. If the molecule changes its orientation on the timescale of the measurement by torsional vibration or rotation, the recorded signal will be averaged. However, the molecular dipole orientation can also be almost constant on the time scale of the measurement, due to a stiff binding of the molecule to the environment or an embedding in a bilayer.

2.2 From signal to image - point spread function and resolution

In fluorescence microscopy, light emitted by a fluorophore is collected with an objective lens and imaged onto a detector. In this context, the individual fluorophores can be treated as point-like sources. Due to the wave nature of light the image of a point source is blurred, as sketched in figure 2.4. As fluorescence emission is an incoherent process, the electric field distribution at position $\vec{r} = (x, y, z)$ is given by [37]:

$$E(\vec{r}) = A \int_0^\alpha \sqrt{\cos(\theta)} \sin(\theta) J_0 \left(k \sqrt{x^2 + y^2} \sin(\theta) \right) e^{ikz \cos(\theta)} d\theta \quad (2.3)$$

Where A depicts a normalization constant and θ is the polar aperture angle, running from 0 to α . The wave number $k = 2\pi n/\lambda_0$ is defined by the vacuum wavelength λ_0 and the refractive index n . This formula for the amplitude point spread function (A-PSF) holds true for the near vicinity of the geometrical focus ($\vec{r} = 0$). For larger distances to the geometrical focus higher orders than the zeroth order J_0 of the Bessel function of the first kind have to be taken into account.

As the detector, such as a camera, does not directly measure the electric field but the light intensity, the electrical field distribution has to be converted into the intensity distribution PSF by calculating the absolute square of equation 2.3:

$$h(\vec{r}) = |E(\vec{r})|^2 \quad (2.4)$$

For an extended fluorescent object $O(\vec{r})$, the image $I(\vec{r})$ results from the convolution

2.2 From signal to image - point spread function and resolution

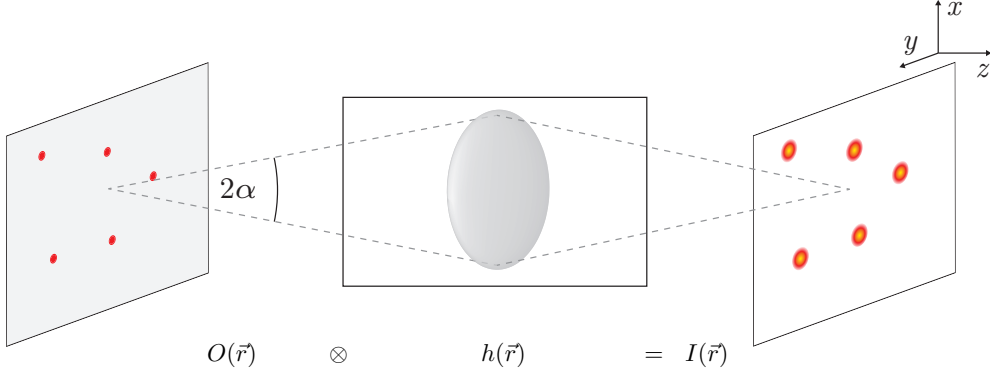


Figure 2.4: The image $I(\vec{r})$ of an object $O(\vec{r})$ is given by its convolution with the PSF $h(\vec{r})$ (eq. 2.5). The size of the PSF depends strongly on the full aperture angle 2α of the imaging lens (eq. 2.3).

of all individual points of the object with the PSF $h(\vec{r})$ [38]:

$$I(\vec{r}) = \int O(\vec{r}') h(\vec{r} - \vec{r}') d\vec{r}' = O(\vec{r}) \otimes h(\vec{r}) \quad (2.5)$$

The normalized intensity profile of the PSF (eq. 2.4) in the detection plane and along the optical axis is shown in the semi-logarithmic plot in figure 2.5. The distribution is point-symmetric around $\vec{r} = 0$. In the focal plane the profile exhibits a high central maximum and side lobes of strongly decreasing intensity. The area within the first order minimum of this pattern is referred to as the Airy disk. In the axial direction the distance to the first order minimum is larger than in lateral direction, thus the PSF is longer than wide.

The Rayleigh criterion states that two objects can just be resolved if the intensity maximum of one falls into the first order minimum of the other [39]. This corresponds with the definition of the radius of the Airy disk. In analogy to the resolution in the lateral direction $\Delta x/y$, the resolution in the axial direction Δz can be defined as the axial distance of the first order minimum to the geometrical focus:

$$\Delta x/y = 0.61 \frac{\lambda_0}{\text{NA}} \quad (2.6)$$

$$\Delta z = 2.00 \frac{n\lambda_0}{\text{NA}^2} \quad (2.7)$$

where

$$\text{NA} = n \sin \alpha \quad (2.8)$$

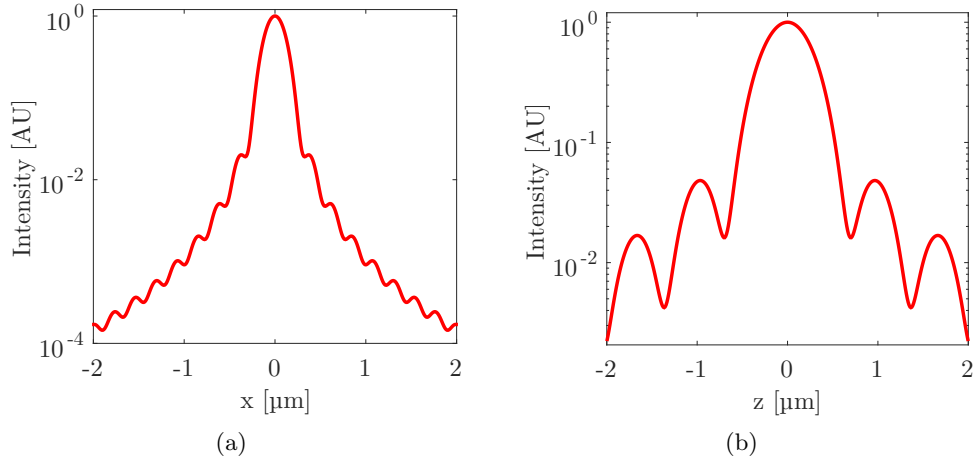


Figure 2.5: Semi-logarithmic intensity profile of the detection PSF in lateral and axial direction through $r = 0$

- a) In the lateral direction the profile has a high central maximum and weak side lobes.
- b) In the axial direction the PSF is extended with a wider distance between the first order minima.

The PSF is calculated with NA 1.4, the refractive index of oil $n = 1.51$ and wavelength $\lambda = 639$ nm.

is the numerical aperture of the objective lens.

Alternatively, the resolution can be defined by the FWHM of the PSF in the axial and lateral direction:

$$\text{FWHM}_{x/y} = 0.51 \frac{\lambda_0}{\text{NA}} \quad (2.9)$$

$$\text{FWHM}_z = 1.77 \frac{n\lambda_0}{\text{NA}^2} \quad (2.10)$$

Neglecting only the weak side lobes of the PSF, the Airy disc can be well approximated by a Gaussian, whose FWHM corresponds to that of the PSF.

2.3 Localization and separation to gain super resolution

2.3.1 Super resolution in two dimensions

The fundamental resolution limit due to diffraction is about half the wavelength of the light used (eq. 2.6). This was already postulated by Abbe in 1873 [2]. The key element for overcoming the diffraction barrier is switching the ability of

2.3 Localization and separation to gain super resolution

fluorophores to fluoresce on and off. This enables the spatiotemporal separation of fluorescent objects within an area of the size of an Airy disc. For this purpose, fluorophores are used, which can be switched between a bright fluorescent and a dark non-fluorescent state. The easiest way to realize that is by switching the fluorophore between the bright excited electronic state S_1 and the dark ground state S_0 . Alternatively, molecules can be switched between an excitable on state and a non-excitable off state, as already described in section 2.1.

There exist two major strategies for overcoming the diffraction barrier: targeted and stochastic switching, which differ in the way how switching is used to overcome the resolution limit.

STED microscopy

In targeted switching-based concepts, the area in which fluorescence is allowed is controlled deterministically. These concepts include methods such as STED [7], SPEM [8], SSIM [9] and RESOLFT [10]. In STED microscopy imaging is performed by scanning two superimposed beams over the sample. Molecules are excited from S_0 to S_1 by a gaussian shaped beam. A second beam of higher wavelength de-excites the molecules back to S_0 . As the second beam exhibits a doughnut shape with zero intensity in its center, all molecules except those at the center are de-excited. Consequently, fluorescence is only allowed at the very center. The size of that area scales inversely with the square root of the intensity of the de-excitation beam and is thus no longer limited by diffraction. A resolution of up to 20 nm FWHM in the focal plane can be reached routinely [11].

SMS microscopy

Stochastic switching is performed, in contrast to targeted switching, in a wide field imaging scheme, where an area orders of magnitude larger than a diffraction limited spot is recorded simultaneously. This, so called, Single Marker Switching (SMS) microscopy is, depending on the underlying switching procedure, known under various names such as: PALM [12], fluorescence photo-activated localization microscopy (fPALM) [40], STORM [13], PALMIRA [14], GSDIM [15], direct stochastic optical reconstruction microscopy (dSTORM) [41].

The overall concept of SMS microscopy is sketched in figure 2.6: In conventional fluorescence microscopy, all fluorescent markers emit simultaneously when the sample is excited (fig. 2.6 left). Due to the overlapping images of nearby emitters,

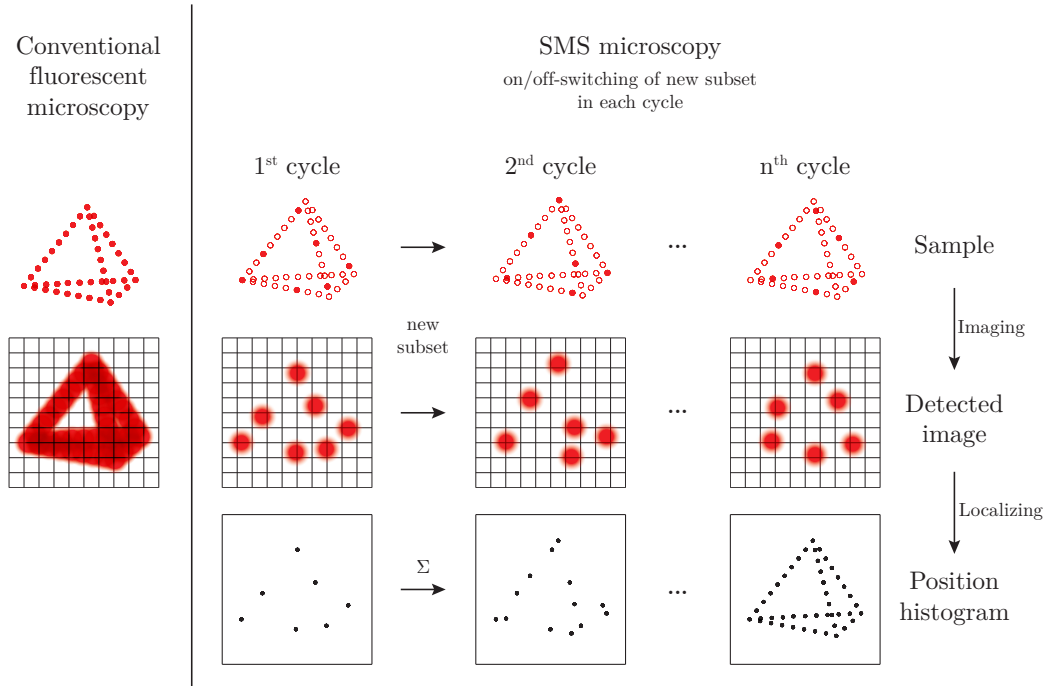


Figure 2.6: Basic concept of SMS microscopy

On the left-hand side the conventional fluorescent microscopy image is shown. On the right-hand side the image formation within the SMS concept is sketched. In each frame the signal of a different subset of switchable fluorophores in their bright state (top row) is detected by a camera (middle row) and subsequently localized (bottom row). The position histogram represents the super resolution image (based on [42]).

structures which are closer than the diffraction limit cannot be separated. In order to distinguish various emitters within a diffraction-limited area their signals need to be separated in time (fig. 2.6 right). This is usually accomplished by using fluorophores which can be switched between a bright and a dark state. If the probability to be in the bright state is sufficiently low, only one fluorophore will emit within a diffraction-limited area during the exposure time of the detector, e.g. during one camera frame. The center of the detected diffraction pattern of each individual molecule can be located very precisely. Drawing a histogram of the positions of each localized emitter generates a map of the respective fluorescent marker positions. In order to obtain sufficient information about the sample, many frames have to be recorded, as indicated in figure 2.6. For imaging cells this number may be in the order of 10^5 frames.

2.3 Localization and separation to gain super resolution

The typical achievable resolution Δr of SMS microscopy is in the range of several 10 nm FWHM in the focal plane [16, 17] and is mainly limited by the number of detected photons N , $\Delta r \propto 1/\sqrt{N}$. This dependency is a result of the localization concept and will be explained in more detail below.

As already mentioned in section 2.2 the diffraction pattern $h(\vec{r})$ (eq. 2.4) can be well approximated by a Gaussian function $h_{\text{Gauss}}(x, y, z)$

$$h_{\text{Gauss}}(x, y, z) = A \exp \left(- \left(\frac{(x - x_0)^2}{2\sigma_{Gx^2}} + \frac{(y - y_0)^2}{2\sigma_{Gy^2}} + \frac{(z - z_0)^2}{2\sigma_{Gz^2}} \right) \right) \quad (2.11)$$

where A is the amplitude and $\sigma_{Gx/y/z}$ the standard deviations of the Gaussian. The latter is directly connected to the FWHM and is usually equal in x and y direction.

$$\text{FWHM} = 2\sqrt{2 \ln 2} \sigma_G \approx 2.35 \sigma_G \quad (2.12)$$

With the definition of the FWHM and the x/y equality, equation 2.11 can be converted to

$$h_{\text{Gauss}}(x, y, z) = A \exp \left(- \frac{4 \ln 2}{\text{FWHM}_z^2} (z - z_0)^2 \right) \cdot \exp \left(- \frac{4 \ln 2}{\text{FWHM}_{x/y}^2} ((x - x_0)^2 + (y - y_0)^2) \right). \quad (2.13)$$

When setting $z - z_0$ to zero, the center of the detection pattern x_0/y_0 from a single fluorophore can be determined by a two dimensional Gaussian fit, $h_{\text{Gauss}}(x, y)$. The quality of this fit defines the localization precision Δr , with $r = \sqrt{x^2 + y^2}$.

As each detected photon can be interpreted as an independent measurement of the molecule position with an uncertainty of σ , the localization precision can be calculated according to the common statistical formula for the standard error of the mean:

$$\Delta r = \frac{\sigma_G}{\sqrt{N}} \quad (2.14)$$

Consequently, the localization precision improves when more photons are detected. On the other hand, the localization precision decreases if the distance $|z|$ of the emitting fluorophore from the detection plane increases, as the detection pattern gets blurred and thus the uncertainty of each independent measurement is increased. According to equation 2.12 the standard error has to be multiplied by a factor of

2.35 in order to express the localization precision in terms of the FWHM.

$$\Delta r_{\text{FWHM}} = 2\sqrt{2 \ln 2} \Delta r \approx 2.35 \frac{\sigma_G}{\sqrt{N}} \quad (2.15)$$

The images read out from the camera contain noise, stemming from different sources: shot noise, background noise, dark current noise, readout noise and pixelation noise [43]. The first two types of noise are due to the characteristics of the fluorescent process and the sample whereby the other noise sources stem from the detection process. The shot noise is already taken into account in equation 2.15. The background noise can be neglected as it can be reduced by an advanced sample preparation and well adapted optics. The dark current and therefore the associated noise is mostly of thermal origin and can thus be neglected if a cooled type of detector is used. The readout noise is a constant noise which adds to the signal of each pixel during the readout process of a charge-coupled device (CCD) chip. It can be neglected if the number of photo-electrons of each pixel is substantially increased prior to the readout process. This is for example the case for EMCCD cameras, but at the expense that the shot noise is increased by an excess noise factor of about $\sqrt{2}$, which is induced by the electron multiplication process [44].

$$\Delta r' = \frac{\sigma_G}{\sqrt{N/2}} \quad (2.16)$$

$$\Delta r'_{\text{FWHM}} \approx 2.35 \frac{\sigma_G}{\sqrt{N/2}} \quad (2.17)$$

The pixelation noise arises from the uncertainty of where a photon arrived in the pixel. Following Thompson et al., the optimal pixel size corresponds to σ_G [45], as a finer pixelation degrades the number of photons which are detected within each pixel and a coarser pixelation leads to the aforementioned loss of information, according to the Nyquist-Shannon sampling theorem.

2.3.2 State of the art 3D methods in SMS microscopy

The SMS concept was first developed for a resolution increase in the lateral direction, that is in two dimensions. However, to also estimate the axial (z) position of the emitter from the shape of the detected blurred signal, several methods have been developed to date. One of the main problems to be solved in this context was that the symmetry of the PSF must be broken with respect to the focal plane, in order to distinguish between molecules located above or below the focal plane.

2.3 Localization and separation to gain super resolution

This can be achieved, for example, by adding asymmetric aberrations to the PSF or by using two axially displaced detection planes (Fig. 2.7).

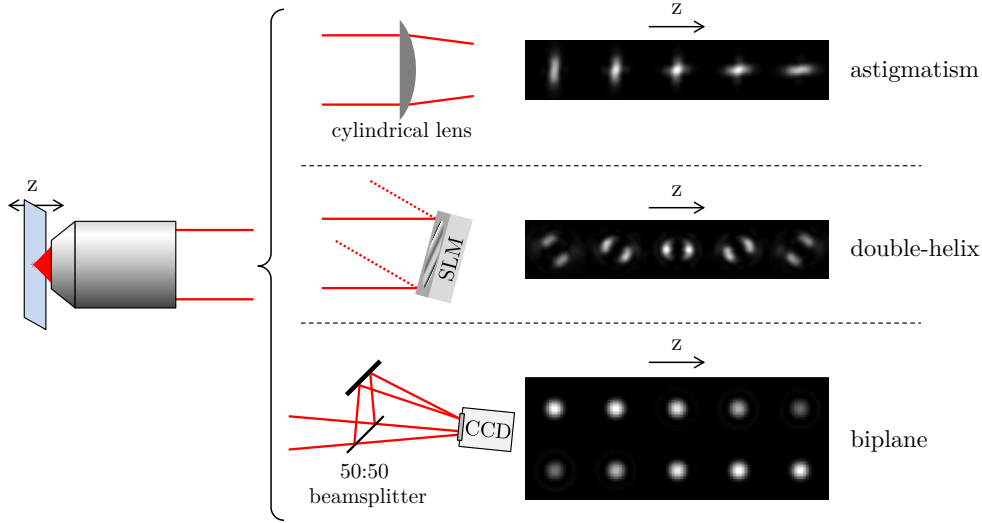


Figure 2.7: Principles of unambiguous localization in the axial direction

The axial position of an emitter can be estimated from the shape of the detected diffraction pattern. As the PSF is typically symmetric with respect to the focal plane this symmetry must be broken. This can, for example, be achieved by adding astigmatism with a cylindrical lens, by changing the shape of the PSF to a double-helix with a SLM or by using two slightly axially displaced detection (bi-)planes.

The use of a cylindrical lens in the detection beam path adds astigmatic aberration to the PSF and creates two slightly different focal planes for the x and y directions. As a result, the ellipticity and orientation of a fluorophore's image varies as its axial position changes [21]. Alternatively, the detection PSF can be engineered, e.g. by a spatial light modulator (SLM), to have two laterally displaced lobes that have a different angle of the line between them depending on the axial position of the emitting molecule. In effect, the PSF appears as a double-helix along the z axis of the microscope [22]. In a biplane setup, the detection beam path is split up and the fluorescence signal is detected in two planes which are slightly displaced in the axial direction. From the differences in the detected diffraction patterns the 3D information can be determined [23]. All these techniques feature a quite anisotropic localization precision which is about $\sigma_{x/y} = 5\text{--}15\text{ nm}$ and $\sigma_z = 15\text{--}25\text{ nm}$ for 1000 detected photons [16]. Additionally, the axial range of these methods is limited to about $1\text{ }\mu\text{m}$ due to the restricted focal depth of the high NA

objective lenses used.

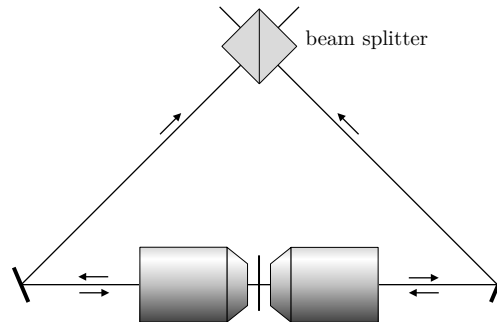


Figure 2.8: Basic principle of a 4Pi-setup

Two opposing lenses focus onto the same spot. The detection beams are interfered by the use of beam splitters (not shown in total). The axial position of the emitter can be determined from the detected interference patterns.

Other methods require signal detection by two opposed objective lenses in a 4Pi configuration (fig. 2.8). Here, the z -position of the emitter is obtained by recombining the fluorescence wavefronts that leave the objective lenses by a 3-way beam splitter to re-divide the two emission wavefronts from the objective lenses, such that three partial wavefronts with a fixed but different equidistant phase difference of $2\pi/3$ are created [24]. The relative intensities of these partial wavefronts represent an about fourfold more precise measure of the emitter's z -position as compared to single lens experiments. However, these interferometric PALM (iPALM) studies are challenged by z -dimension localization ambiguities for layers thicker than $\lambda/2$ (225 nm), limiting iPALM to ultraflat structures or to the proximity of the coverslip. In the 4Pi-SMS configuration the shape of the wavefronts is additionally taken into account, whereby the focal depth is extended to about $1\ \mu\text{m}$ [17]. These techniques feature an almost isotropic resolution, with $\sigma_{x/y} = 4\text{--}9\ \text{nm}$ and $\sigma_z = 2\text{--}3\ \text{nm}$. But the experimental implementation is very challenging with respect to alignment and control.

Recent work in the W-4PiSMSN setup corrects for aberrations and optimizes the PSF quality by the use of deformable mirrors [46]. But for measuring samples thicker than about $1.2\ \mu\text{m}$, valid for most cells, axial scanning is still necessary.

2.3.3 Relation of numerical aperture and focal depth

The focal depth is the range in which an objective lens is able to image a point source, such as a fluorescent molecule, sufficiently sharp onto a detector. The size of the diffraction pattern depends mainly on the NA of the objective lens and corresponds to the axial FWHM of the detection PSF, equation 2.10. A high-resolution oil immersion objective lens with NA 1.4 has a small FWHM in the axial direction (table 2.1). That is why the focal depth of the above mentioned 3D methods are all limited to about 1 μm .

	NA 1.4	NA 0.8
refractive index n	oil 1.51	water 1.33
solid angle Ω	$1.25\pi \text{ sr} \hat{=} 3.93 \text{ sr}$	$0.40\pi \text{ sr} \hat{=} 1.26 \text{ sr}$
FWHM $_{x/y}$	0.27 μm	0.44 μm
FWHM $_z$	0.64 μm	2.19 μm

Table 2.1: Solid angle and PSF characteristics FWHM $_{x/y/z}$ of two objective lenses with NA 1.4 and NA 0.8

Typical cell samples are thicker than these 1 μm which is why several layers need to be imaged successively in order to cover the whole depth of the sample. The use of objective lenses with for example NA 0.8 and water immersion would lead to a great extension of the axial FWHM. Thereby a much larger depth can be covered at once, briefly sketched in figure 2.9. The PSFs are calculated accordingly to the electric field distribution at equation 2.3.

As the NA depends on the refractive index n and the aperture angle α , equation 2.8, a lower NA objective lens usually exhibits a lower aperture angle and therefore the number of collected photons is typically decreased. Especially in SMS microscopy the number of detected photons is the key element for achieving the super resolution. Therefore, when using lower NA objective lenses the loss of localization precision needs to be compensated. A solution for this problem is presented in the following.

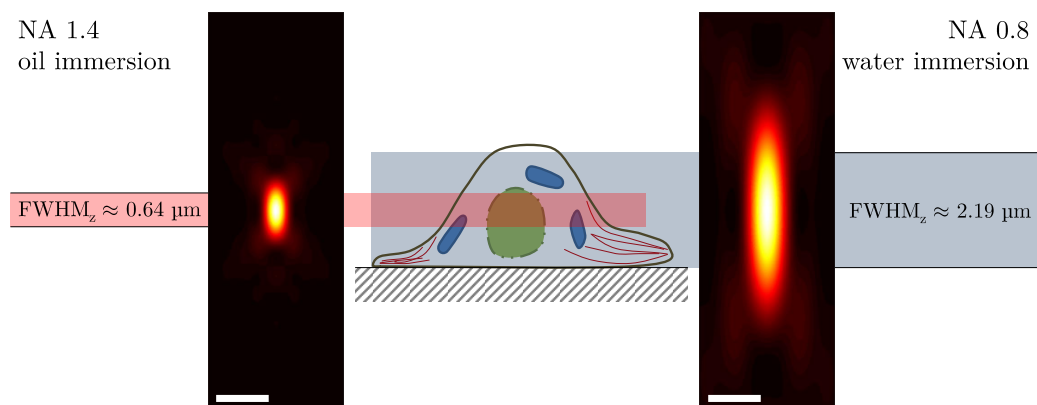


Figure 2.9: Comparison of the PSFs of two objective lenses: NA 1.4, oil immersion and NA 0.8, water immersion. The focal depth is indicated by the FWHM and sketched inside a cell. The high NA objective lens covers a much thinner region than a lower NA objective lens does. The scale bars indicate $1 \mu\text{m}$.

Chapter 3

Stereo 3D-SMS microscopy

3.1 Fundamental concept

3.1.1 From 2D plane to 3D space by spatial imaging

The most basic and probably best known concept for three-dimensional imaging is used by our eyes with their different viewing directions. When transferring this concept of spatial perception into microscopy, the problems arise that only the surface of a volume is recorded and that structures below the diffraction limit cannot be resolved. In addition, typical microscopes with a single objective lens or with two objective lenses in the 4Pi arrangement [17] do not provide any of the necessary spatial information due to the lack of data along the optical axis.

By combining spatial depth perception with the SMS microscopy, high-resolution images with information throughout the whole measured volume are possible. In this process, the entire object is decomposed into the individual fluorophores, with mutually overlapping signals being separated in time by switching them on/off according to the SMS concept. The simultaneous recording of these individual events from different, spatially independent viewing directions makes it possible to determine their position in space. For this, only the transformation parameters from the image spaces (2D) to the object space (3D) must be known.

The basic concept of this spatial imaging is also sketched in the figure 3.1. For the sake of simplicity, this is done two-dimensionally, but the extension to 3D is easily possible by adjusting the dimensions. The principle of reconstruction is explained afterwards.

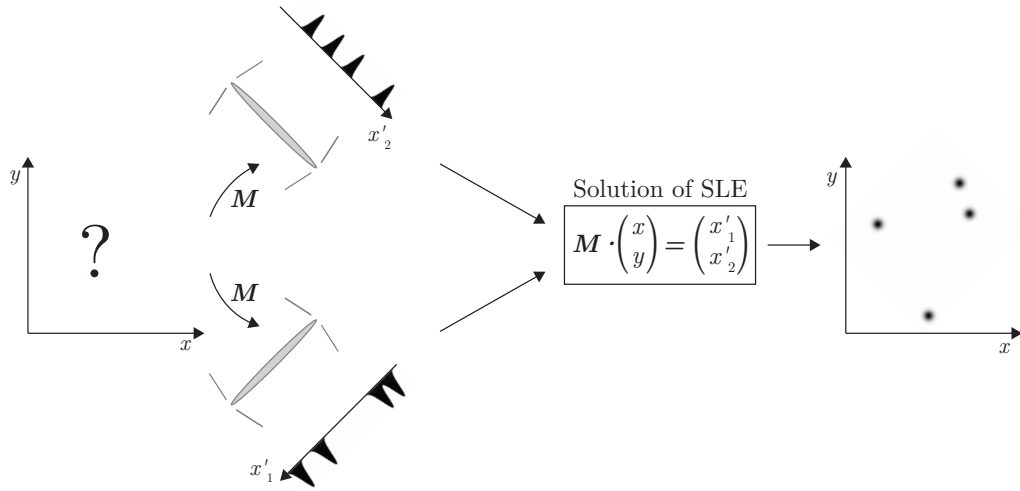


Figure 3.1: Basic concept of stereo view, exemplary in 2D

An unknown 2D object, consisting of isotropic emitting point sources, is imaged from two different directions, with both optic axis lying in plane x/y . The resulting one-dimensional images extend along the new coordinate axes x'_1 and x'_2 , respectively. If the transformation matrix M is known, a system of linear equations can be set up. With this it is possible to calculate the initial 2D coordinates of the emitters (x, y) . The extension to 3D objects follows the same principle.

Essentially, spatial imaging is an inverse problem where the position

$$\vec{r} = \begin{pmatrix} x \\ y \\ z \end{pmatrix} \quad (3.1)$$

of the object in the base coordinate system is unknown. A common way to address such an inverse problem is to set up a system of linear equations (SLE).

$$M \cdot \vec{r} = \vec{R}' \quad (3.2)$$

This main equation needs to be solved in order to calculate the spatial position of the object.

Vector \vec{R}' holds the correlated coordinates $\vec{r}'_i = \begin{pmatrix} x'_i \\ y'_i \end{pmatrix}$, which are the positions of the object image in the respective detection plane. Its length depends on the number

K of images, taken under different orientations.

$$\vec{R}' = \begin{pmatrix} x'_1 \\ y'_1 \\ \vdots \\ x'_K \\ y'_K \end{pmatrix} \quad (3.3)$$

Here, \vec{r}'_i corresponds to the localized centers of the diffraction-limited detection patterns, originating from individual fluorophores. These center positions, which belong to the same emitter, form the above system of linear equations.

In order to understand how matrix \mathbf{M} is built, let us first consider that a Cartesian coordinate system can be arbitrarily positioned in 3D space by a series of rotations. One possible combination is the rotation first along the initial z -axis by angle δ , (rotation matrix $\mathbf{D}_z(\delta)$), followed by a rotation along the new y -axis by angle β , (rotation matrix $\mathbf{D}_y(\beta)$) and finally along the now arising z -axis by angle γ , (rotation matrix $\mathbf{D}_z(\gamma)$). The final transformation matrix \mathbf{D} is given by the multiplication of the three corresponding rotation matrices.

$$\mathbf{D} = \mathbf{D}_z(\gamma) \cdot \mathbf{D}_y(\beta) \cdot \mathbf{D}_z(\delta) \quad (3.4)$$

$$= \begin{pmatrix} \cos(\gamma) & \sin(\gamma) & 0 \\ -\sin(\gamma) & \cos(\gamma) & 0 \\ 0 & 0 & 1 \end{pmatrix} \cdot \begin{pmatrix} \cos(\beta) & 0 & -\sin(\beta) \\ 0 & 1 & 0 \\ \sin(\beta) & 0 & \cos(\beta) \end{pmatrix} \cdot \begin{pmatrix} \cos(\delta) & \sin(\delta) & 0 \\ -\sin(\delta) & \cos(\delta) & 0 \\ 0 & 0 & 1 \end{pmatrix} \quad (3.5)$$

The matrix multiplication results in:

$$\mathbf{D} = \begin{pmatrix} \cos(\beta) \cos(\delta) \cos(\gamma) - \sin(\delta) \sin(\gamma) & & & & \\ -\cos(\delta) \cos(\beta) \sin(\gamma) - \sin(\delta) \cos(\gamma) & & & & \\ \sin(\beta) \cos(\delta) & & & & \\ & \cos(\beta) \sin(\delta) \cos(\gamma) + \cos(\delta) \sin(\gamma) & -\sin(\beta) \cos(\gamma) & & \\ & -\cos(\beta) \sin(\delta) \sin(\gamma) + \cos(\delta) \cos(\gamma) & \sin(\beta) \sin(\gamma) & & \\ & \sin(\beta) \sin(\delta) & & \cos(\beta) & \end{pmatrix} \quad (3.6)$$

Since R' holds only the 2D coordinates of $\begin{pmatrix} x_i \\ y_i \\ z_i \end{pmatrix} = \mathbf{D}_i \cdot \vec{r}$, just the first two rows of

D_i with $i = 1 \dots K$ are needed for the combined matrix M .

$$M = \begin{pmatrix} \cos(\beta_1) \cos(\delta_1) \cos(\gamma_1) - \sin(\delta_1) \sin(\gamma_1) \\ -\cos(\delta_1) \cos(\beta_1) \sin(\gamma_1) - \sin(\delta_1) \cos(\gamma_1) \\ \vdots \\ \cos(\beta_K) \cos(\delta_K) \cos(\gamma_K) - \sin(\delta_K) \sin(\gamma_K) \\ -\cos(\delta_K) \cos(\beta_K) \sin(\gamma_K) - \sin(\delta_K) \cos(\gamma_K) \\ \cos(\beta_1) \sin(\delta_1) \cos(\gamma_1) + \cos(\delta_1) \sin(\gamma_1) & -\sin(\beta_1) \cos(\gamma_1) \\ -\cos(\beta_1) \sin(\delta_1) \sin(\gamma_1) + \cos(\delta_1) \cos(\gamma_1) & \sin(\beta_1) \sin(\gamma_1) \\ \vdots & \vdots \\ \cos(\beta_K) \sin(\delta_K) \cos(\gamma_K) + \cos(\delta_K) \sin(\gamma_K) & -\sin(\beta_K) \cos(\gamma_K) \\ -\cos(\beta_K) \sin(\delta_K) \sin(\gamma_K) + \cos(\delta_K) \cos(\gamma_K) & \sin(\beta_K) \sin(\gamma_K) \end{pmatrix} \quad (3.7)$$

All in all, the dimensions of the components in equation 3.2 are

$$M_{(2K,3)} \cdot \vec{r}_{(3,1)} = \vec{R}'_{(2K,1)} \quad (3.8)$$

Since the precision of the localization of the detection patterns is always limited due to the finite number of detected photons, a unique solution of the system of linear equations is very unlikely. Therefore, the most probable position of the emitter is calculated using the method of least squares [47].

$$\min_{\vec{r}} \|\mathbf{M}\vec{r} - \vec{R}'\|^2 = \min_{\vec{r}} \sum_{i=1}^{2K} \left((\mathbf{M}\vec{r})_i - \vec{R}'_i \right)^2 \quad (3.9)$$

Depending on the distance of the emitter to the respective focal plane the detection pattern will be differently blurred. Also the number of the collected photons can vary, for example due to some emission anisotropy as shown in chapter 2.1.3. Following equation 2.15, a wider detection pattern (corresponds to a larger standard deviation σ_G) and/or less detected photons (N) decrease the localization precision. Most often the precision will be different for each detection plane which is why a specific weighting should be added to the calculation. This can be done, for example, by dividing each element of the sum by the corresponding standard error.

$$\min_{\vec{r}} \sum_{i=1}^{2K} \left(\frac{(\mathbf{M}\vec{r})_i - \vec{R}_i}{\Delta r_i} \right)^2 = \min_{\vec{r}} \sum_{i=1}^{2K} \frac{\left((\mathbf{M}\vec{r})_i - \vec{R}_i \right)^2 N_i}{(\sigma_{Gi})^2} \quad (3.10)$$

Solving the system of linear equations is not the only way to determine the position of the emitter. An alternative is to calculate the expected detection patterns for a specific position using the PSF (eq. 2.4) and the transformation matrix (eq. 3.6). The aim is to iteratively find the spatial emitter position whose calculated detection patterns matches the actual images in the different detection planes best. Also, a combination of the latter and the SLE is possible, where the method of least square provides an estimate of the 3D emitter position and the PSF calculation makes some fine adjustments. For the proof of concept, however, only the solution strategy with the SLE is used in this thesis.

3.1.2 Achieving high isotropic resolution with spatial imaging

In order to realize the presented 3D image concept and to design it practically, the structure should achieve a high and isotropic resolution in all spatial directions.

The standard error and therefore the localization precision typically improves with a higher number of detected photons and a larger numerical aperture of the objectives. To optimize localization precision, the 4Pi-setup with two opposed high-NA objectives is the optimum. However, this implementation does not provide axial position information in the sense of spatial imaging. In contrast, two orthogonal objectives gain a lot of 3D information, but in the directions where no objective is placed, many photons will be lost.

When using multiple objective lenses, the total solid angle of a sphere $4\pi \approx 12.57$ sr must be divided between the respective aperture angles. By using four objective lenses in a tetrahedron arrangement, featuring a common focal spot, a large part of the isotropically emitted photons can be collected, since a majority of the spatial angle can be covered. At the same time, the calculation of the emitter position results in an almost isotropically resolved image of the sample, since no spatial direction is preferred. The use of even more similar objectives automatically lowers the maximum possible NA of each individual objective due to the shared maximum solid angle and with it the signal to noise ratio.

In the tetrahedron arrangement of four similar objectives the maximal possible NA for each of it is smaller than for a 4Pi setup. In consequence the precision of the localizations decreases due to the lower number of collected photons and the larger standard deviation σ_G . But this can be counteracted by the great over-determination of the SLE for the emitters position when detecting simultaneously from four different directions. Each direction contributes the two coordinates x'_i and y'_i . With four detection planes the SLE (eq. 3.2) contains eight equations to

recalculate the three Cartesian coordinates $x/y/z$ of the emitter.

Each objective has a specific focal depth that is much smaller than the lateral dimension of the field of view. The standard error of the calculated emitter position is best when the emitter is in the common focal point. This is because its detection patterns are sharply focused on all detection planes. With increasing distance, the detection patterns become blurred in at least some of the detection planes. The blurring increases the standard deviation σ_G , which reduces the localization precision. Consequently, in a tetrahedron arrangement with four symmetrically overlapping focal planes, the isosurfaces with equal precision form an octahedron shape.

3.2 Further characteristics

3.2.1 Focal shift

Passing an optical boundary between a lens and its focus position causes aberrations and apodizations which leads to a focal shift. Depending on where the boundary is located between the two, the focal shift is differently pronounced.

The focussing through an optical boundary can be illustrated by geometrical optics, figure 3.2.

The aperture angle θ_1 of the objective lens is given by the NA and the refractive index n_1 . The refraction at the surface to the media with refractive index n_2 is in accordance to Snell's law.

$$n_1 \sin \theta_1 = n_2 \sin \theta_2 \quad (3.11)$$

In the sketched case the focussing goes to a medium with higher refractive index, $n_1 < n_2$, and the ray is refracted towards the normal, $\theta_1 > \theta_2$. Thereby the focus position is shifted away from the lens, with respect to the case without the second media. If the distance A of the objective lens towards the boundary decreases, $A_1 > A_2$, the distance D of the objective lens towards the focus position increases, $D_1 < D_2$. This focus shift does not depend on a possible third medium in between the two media with n_1 and n_2 , which is why the influence of a cover glass or the like can be neglected.

The basic behavior can be illustrated by rays, but due to the wave characteristics of light the details and the quantitative numbers do not follow the geometrical optics anymore. The results of the theoretical discussion [48] are sketched in figure 3.3 with the focal shift as a function of the focussing depth d ($d = 0$ is located directly on top

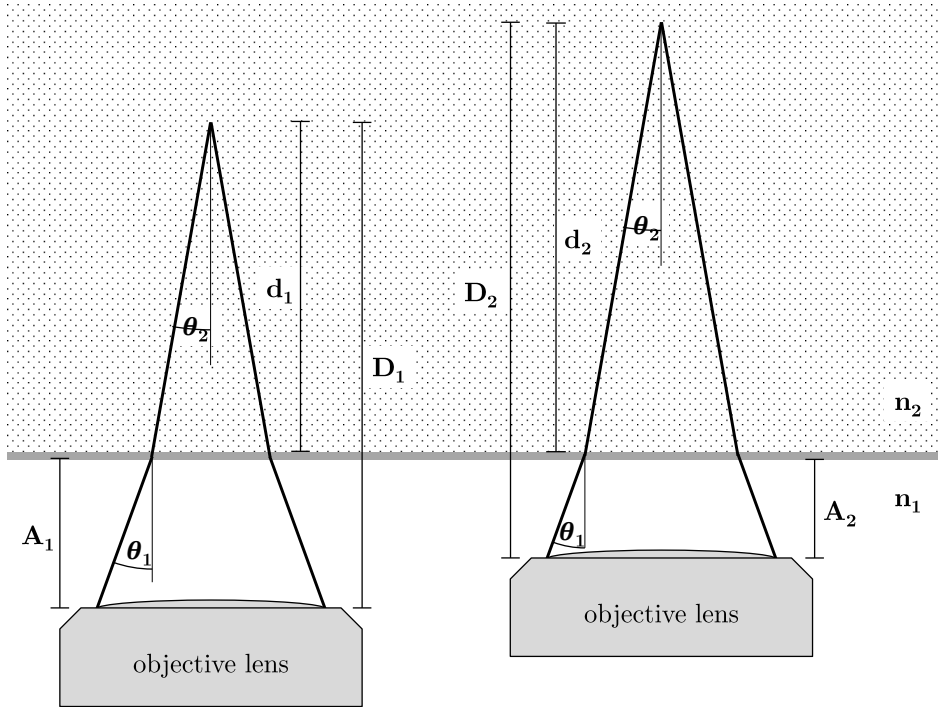


Figure 3.2: Shifting of the focus position when moving the objective

of the cover glass). The behavior of this transition from oil ($n_1 = 1.518$) to water ($n_2 = 1.33$) is the opposite than illustrated in figure 3.2: The shift counteracts the focussing depth. Unlike for the discussion with geometrical optics, the rise of the absolute value of the focal shift is not linear but instead decreases with increasing focussing depth for this case of $n_1 > n_2$.

When focussing multiple objectives onto each other and moving the common focus point inside the sample the focal shift gets relevant. If a possible optical boundary is shifted along the axis of one of the objectives, the position of its focus point is shifted. This shifting needs to be compensated to keep all focus points together and to ensure a correct movement within the coordinate system.

3.2.2 Diffusion of particles

Next to the Single Marker Switching microscopy the setup can also be used to track particles, moving around within the detected volume. There are various applications, for example the functioning of walking motors within cells, operation strategies of bacteria and cilia whose mechanical interaction is dominated by friction, or the rates of enzyme-mediated chemical reaction [49].

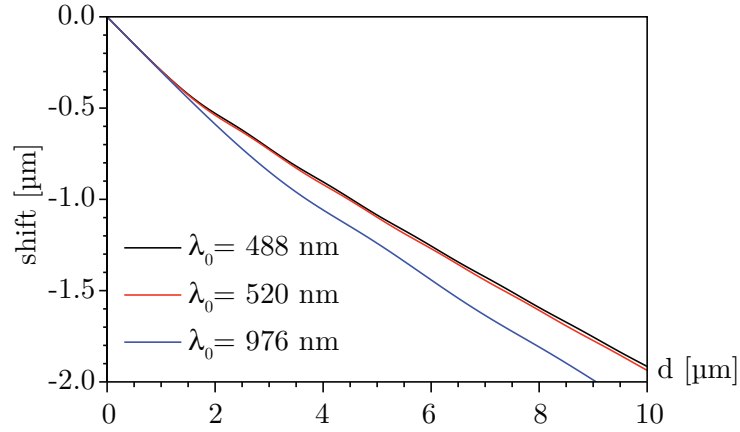


Figure 3.3: Theoretical focus shift, calculated for an optical transition from oil ($n_1 = 1.518$) to water ($n_1 = 1.33$) [48]

A simplified model is the diffusion of fluorescent particles inside a liquid of a specific viscosity. The mean square displacement (MSD), $\langle (r_N)^2 \rangle$ given in $[\text{m}^2]$, within a specific time τ [s] depends on the size of the particles and the properties of the embedding medium. Hereby N is the number of steps and the MSD can be calculated by internal averaging with all pairs [50].

Assuming a non-moving homogeneous liquid with the diffusion constant D [m^2/s] and a uniform fluorescent bead with radius R [m], an undirected normal diffusion is expected. Depending on the spatial dimension of the system n , the diffusion constant corresponds to the MSD by the following [49]:

$$\langle (r_N)^2 \rangle = 2 \cdot n \cdot D \cdot \tau \quad (3.12)$$

Furthermore, the dynamic viscosity η [$\text{Pa} \cdot \text{s}$] of the embedding medium and the diffusion constant are correlated by the Stokes-Einstein relation.

$$D = k_B \cdot T / (6 \cdot \pi \cdot \eta \cdot R) \quad (3.13)$$

This holds for a macroscopic sphere of many nanometers which is moving slowly within a fluid [49], with the Boltzmann constant k_B [J/K] and the temperature T [K].

When determining the viscosity differently, for example by a viscometer, in some cases the kinematic viscosity ν [m^2/s] is measured. This can be converted to the

dynamic viscosity η by multiplying with the density of the fluid ρ [kg/m³].

$$\eta = \nu \cdot \rho \quad (3.14)$$

3.3 Practical realization

In order to achieve the goal of this thesis the practical realization of a setup using spatial imaging in combination with the localization scheme, according to section 3.1, is essential. The fundamentally new approach requires the development of a novel microscope layout together with the electronic control and the subsequent analysis of the measured data.

3.3.1 Combination of objectives

As a result of the theoretical considerations, the microscope should be based on the use of four objectives in a tetrahedron arrangement, section 3.1.2. All of them should focus on the same spot and the respective numerical aperture should be as high as possible. Due to the severely restricted space a slim design and a long focal length is required for the objectives. In addition, the sample needs to be embedded in buffer and placed in the center whereby the non-perpendicular crossing of an optical surface is to be avoided in order to prevent optical aberrations.

These requirements can be fulfilled by the use of one air immersion objective facing straight upwards and three water dipping objectives facing tilted downwards in the tetrahedron arrangement:

1x Zeiss Objective LD Plan-Neofluar 63x/0.75 Corr

- 63x magnification
- 0.75 NA
- 2.2–1.2 mm working distance, depending on cover glass thickness
- 0–1.5 mm cover glass thickness, adjusted to by a correction ring
- air immersion
- $\alpha = 48.59^\circ$ semi-aperture angle
- $\Omega = 2.13$ sr solid angle
- label: objective 1

3x Nikon CFI Apo 40XW NIR

- 40x magnification
- 0.8 NA
- 3.5 mm working distance
- without cover glass
- water dipping
- $\alpha = 36.98^\circ$ semi-aperture angle
- $\Omega = 1.26$ sr solid angle
- label: objectives 2–4

The solid angle Ω is calculated by

$$\Omega = 2\pi(1 - \cos \alpha) \quad (3.15)$$

whereby α is the semi-aperture angle (eq. 2.8). The overall covered solid angle adds up to 7.6 sr resp. 2.4π sr.

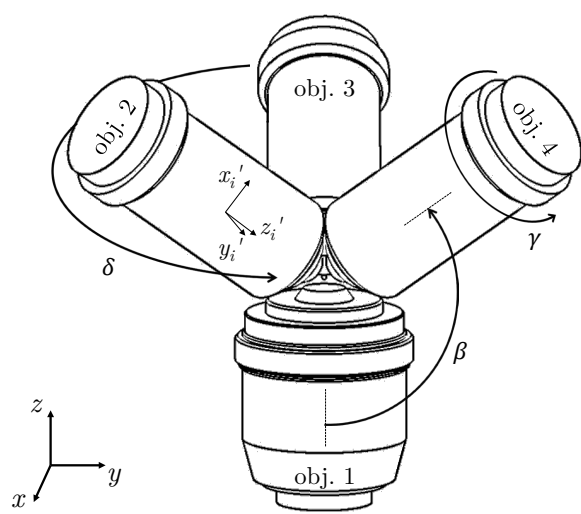


Figure 3.4: Orientation of the objectives in a tetrahedron like shape.

One air immersion objective (obj. 1) is facing upwards and three water dipping objectives (obj. 2-4) are facing tilted downwards. The relation of the respective coordinate systems \vec{r}_i' to the basic coordinate system \vec{r} can be described by the rotation angles β , δ and γ .

The tetrahedron like arrangement of the specified objectives is sketched in figure 3.4, with the x/y -plane of the basic coordinate system in the horizontal and the z -axis pointing upwards. The relationships of the detection planes to the basic coordinate system can be described by the angles δ for the rotation about the ordinary z -axis, β for the uplifting and γ for the rotated imaging onto the detector. Due to the physical dimensions of the objective housings the tetrahedron angle of 109.5° cannot be used. Instead, the available range for beta is very narrow, namely the lower limit is $\beta = 125.5^\circ$ and the upper limit is only slightly higher due to the small free space ($<300\ \mu\text{m}$) between the objective lenses. Therefore, in the aim of spatial imaging, less information about the z -direction is acquired than with a perfect tetrahedron shape. The rotation of the objectives 2–4 along the z -axis is $\delta = 0^\circ/120^\circ/240^\circ$. The rotation γ of the images with respect to the detector depends on the particular detection beam paths.

A specifically designed aluminium frame arranges the upper objective lenses 2–4 in the intended tetrahedron like shape, figure 3.5. The adapted mounting of the objective lenses onto that frame enables five degrees of freedom for fine adjustment: two rotational and three translational.

Due to the severely limited space between the upper objective lenses, their orientation needs to be precisely set in order to avoid contact with each other. Therefore, two rotational adjusters with mechanical fine thread screws are incorporated which finetune angle β and δ .

In order to overlay all focal points the respective cartesian positions of the objective lenses can be translated in all three directions. This is done by electronically controlled linear positioners with nanometer accuracy and millimeter travel range (SLC-17 and SLC-24, SmarAct). Matched constant force springs take the load off the positioners to ensure a great stability of the set positions.

The objective lens 1, facing the overall focus position from below (figure 3.6), has just one degree of freedom. A linear positioner of the same kind as before enables a translation up and down along the respective z' axis. Also here, constant force springs balance the weight of the objective lens.

3.3.2 Mounting of the sample

The presented arrangement of the four objective lenses gives space in the enclosed area for a cover glass with $\varnothing = 5\ \text{mm}$ diameter and a sample holder.

A cross section view of the rotationally symmetric sample holder in combination with objective lenses 1 and 2 is sketched in figure 3.7a. The extraordinary shape

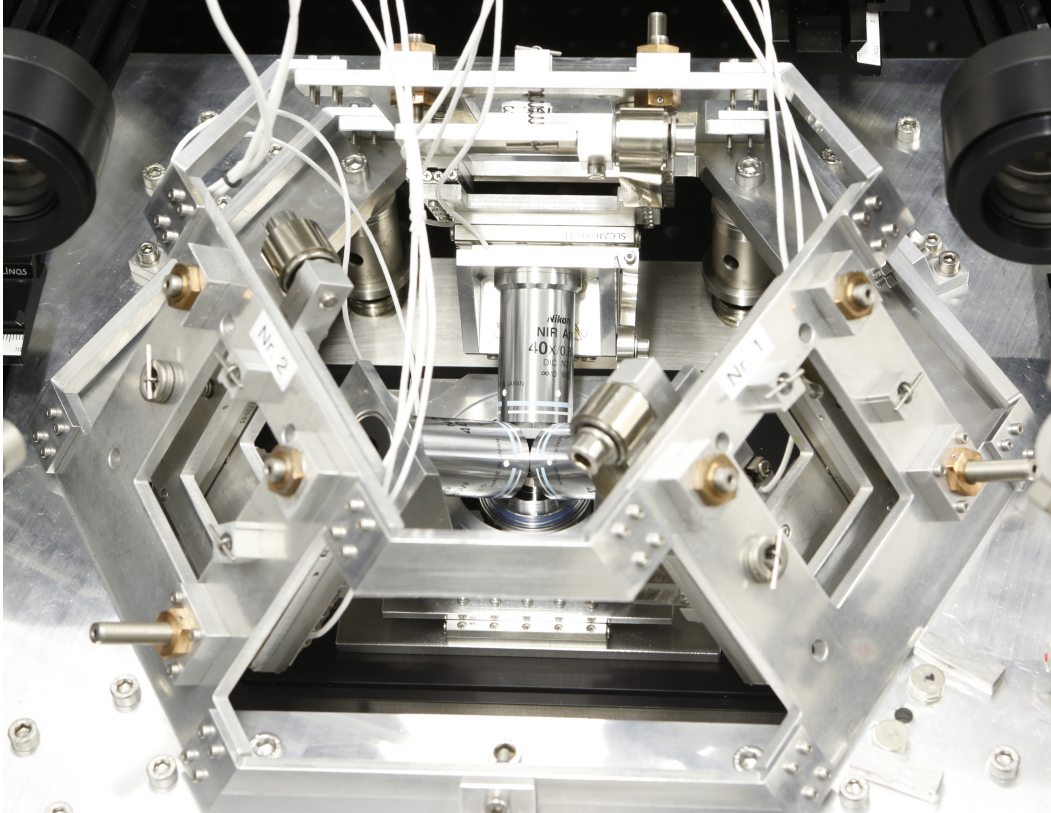


Figure 3.5: Mounting of the objectives, top view

Each of the upper objective lenses is held individually, mounted to an aluminium frame with 5 degrees of freedom: 2 for rotation, 3 for translation. The rotation angles can be adjusted mechanically by fine thread screws. The translation is done by electronically controlled linear positioners, one for each direction.

in the center of the holder follows the given dimensions of the objective lenses and brings the cover glass, and with it the sample, into the focal spot. There is space for movements of a few millimeter laterally and up to half a millimeter vertically for the sample holder. The bottom objective lens is air immersed while the front lenses of the upper objective lenses together with the sample are embedded in aqueous medium.

An illustration of the steel sample holder (grey) together with a plastic inset (blue) can be seen in figure 3.7b. The inset reduces the required volume of embedding medium from about 26 ml to 7.5 ml.

The cover glass itself is made of fused quartz which induces less background signal than standard borosilicate cover glasses. The correction ring of objective lens 1

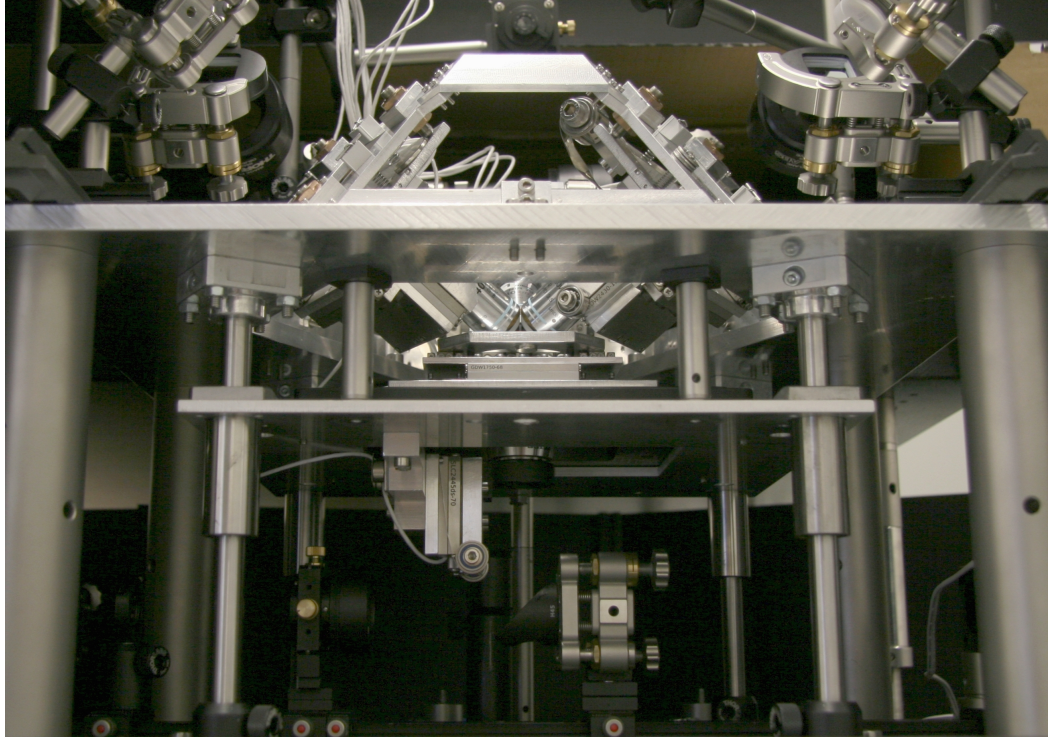


Figure 3.6: Mounting of the objective lenses, side view

At the bottom the whole combination of objective lens 1 and sample stage, mounted to a metal board, can be moved up and down along four guide shafts in order to enable the exchange of the sample. The objective lens itself has one degree of freedom for vertical translation, electronically controlled by a linear positioner.

needs to be adjusted to the $300\ \mu\text{m}$ thickness of the quartz cover glass used.

The sample holder is placed on a $x/y/z$ -translation stage. The horizontal positions x and y can be controlled with nanometer resolution and $>20\ \text{mm}$ travel range by two crosswise oriented linear positioners (SLC-17, SmarAct). Both are placed on a z -stage with also nanometer resolution and $300\ \mu\text{m}$ travel range (Nano-Z, Mad City Labs).

In order to exchange the sample the whole assembly of sample holder, translation stage and objective lens 1, all mounted to a metal board, can be moved downwards along four guide shafts. The attachment to the shafts is done by ball bushing bearings which can be seen in figure 3.6. This precise guidance enables an almost reproducible alignment of the bottom entity with respect to the upper objective lenses.

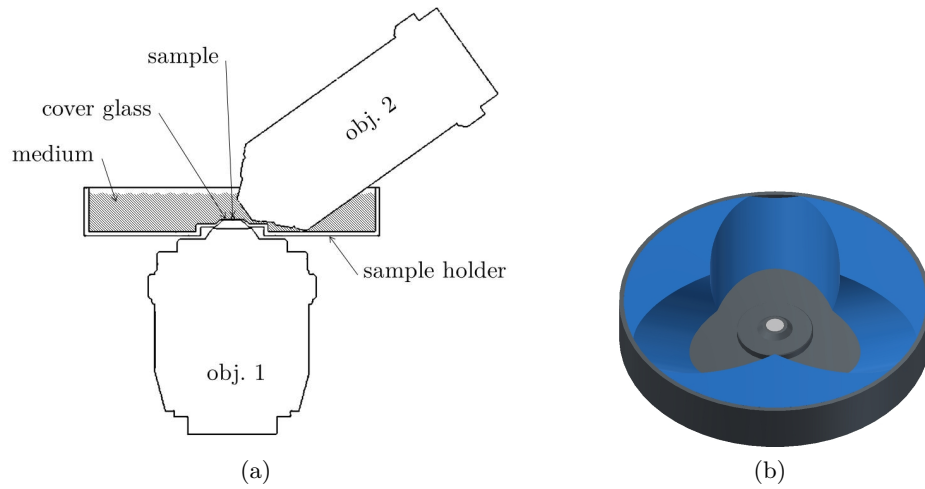


Figure 3.7: Cross section view and illustration of the sample holder

- a) The sample is located upon a cover glass which is mounted to a sample holder and embedded in aqueous medium. Due to the specific shape of the central part of the holder, the sample can be placed in the common focal spot of the objective lenses. The level of the medium must be high enough to cover the whole front lenses of the upper objective lenses.
- b) Into the circular sample holder an inset is implemented which fills the unused space. Hereby, the amount of medium can be reduced to about one third.

3.3.3 Index matching cover glass

The lowest edge of the front lenses of the dipping objective lenses is positioned next to and below the upper surface of the cover glass. To prevent artifacts in the detected PSF a matching of the refractive indices of the cover glass and the medium would be best. The dipping objective lenses are designed for the refractive index of water $n = 1.33$. One possibility to reduce the refractive index of the cover glass is to manufacture them by the fluoropolymer CYTOP™, AGC Chemicals.

The hardened CYTOP™ has a refractive index of $n_{\text{CYTOP}} = 1.34$ and a transmittance of $> 95\%$ in the visible region. The solvent of about 91% in the stock solution can be removed by following a baking protocol of several days. The aim is to create $\varnothing = 5$ mm cover glasses with about 0.5 mm thickness made of CYTOP™. This can be done by pouring the required amount of the stock solution in a glass petri dish, removing the solvent and cutting the residual disk to the desired shape by a laser cutter.

3.3.4 Illumination and detection

The emission spectrum of a fluorophore is red shifted towards the excitation spectrum by the Stokes shift, following section 2.1. The emitted light can be separated from the typically much more intense excitation light by using dichroic mirrors, which are designed such that they reflect a certain wavelengths band while transmitting another, compare to figure 3.8. In epifluorescence microscopy, such a mirror enables the use of the same beam path through a single objective lens for excitation and detection.

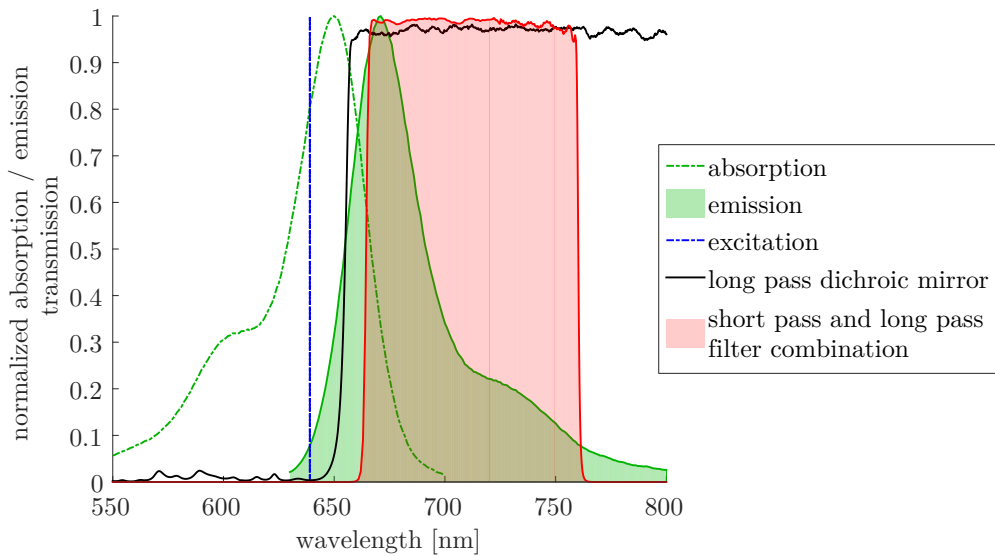


Figure 3.8: Filter combination together with the normalized absorption and emission of the dye.

The absorption spectrum of the dye Alexa Fluor 647 is indicated by a green dashed line, the emission spectrum by a green area. The excitation by a 639 nm laser is marked by a dashed blue line. The separation of excitation and emission is done by a dichroic mirror (F38-635, AHF), black line. In order to reduce noise effects the camera is covered by a short and a long pass filter (F37-774, F47-665, AHF), red area. Most of the emitted light from the dye can pass this filter combination.

The afore presented setup is designed such that excitation and detection is possible using all four objective lenses. So in the pathway from each objective lens a dichroic mirror (DC, F38-635, AHF) is implemented for separating the two beam paths.

For the imaging the fluorescence from all four channels is directed onto one quarter

of a single EMCCD-chip, which eliminates the need for synchronization. The camera (iXon-3 897, Andor Technology) is placed in a common image plane. The field of view of each detection path is cropped by rectangular irises (RI) in an intermediate image plane to avoid overlaps. Perpendicular oriented mirrors (PM) are used to position the images close to each other on the camera chip.

In order to reduce the influence of scattered light the camera chip is covered by different filters (F). The combination of a short pass (F37-774, AHF) and a long pass filter (F47-665, AHF) acts like a band pass whose transmission band almost covers the full emission spectrum, red area in figure 3.8. An additional notch filter (F40-635, AHF) eliminates remaining light of the high power excitation laser.

The excitation (orange) and detection (red) beam paths are sketched in figure 3.9, along with the implemented optical elements. Each objective lens has its corresponding tube lens (TL) followed by various achromatic lenses (L) of different focal length in order to adjust the final magnification. Following section 2.3 one pixel of the camera should cover an area of $\sigma_G \times \sigma_G$ with

$$\sigma_G \approx \frac{1}{2.35} \cdot \text{FWHM} = \frac{0.51 \cdot \lambda}{2.35 \cdot \text{NA}},$$

when projected into the sample plane. The fluorescent dye Alexa Fluor 647 has an emission peak at $\lambda = 665 \text{ nm}$. With this and the given numerical apertures of the objective lenses the effective pixel side length calculates to 192 nm for objective lens 1 (NA 0.75) and 180 nm for objective lenses 2–4 (NA 0.8). A single pixel on the CCD-chip has a physical dimension of $16 \mu\text{m} \times 16 \mu\text{m}$. Thereby, a total magnification of 83.1x respectively 88.7x is intended.

The excitation is done by two identical continuous wave high-power laser with $\lambda = 639 \text{ nm}$ wavelength (Coherent OPSP 639nm 1.5W, suppliers: HB-Lasers and tarm). One is used for the illumination from below and one for the illumination from above, whereby the beam of the latter is divided by beam splitters (BS) almost equally into three, one part for each objective lens 2–4. In order to achieve a wide-field illumination the lenses in the excitation beam paths are arranged such that the beam is almost focused in the back focal plane of the objective lens.

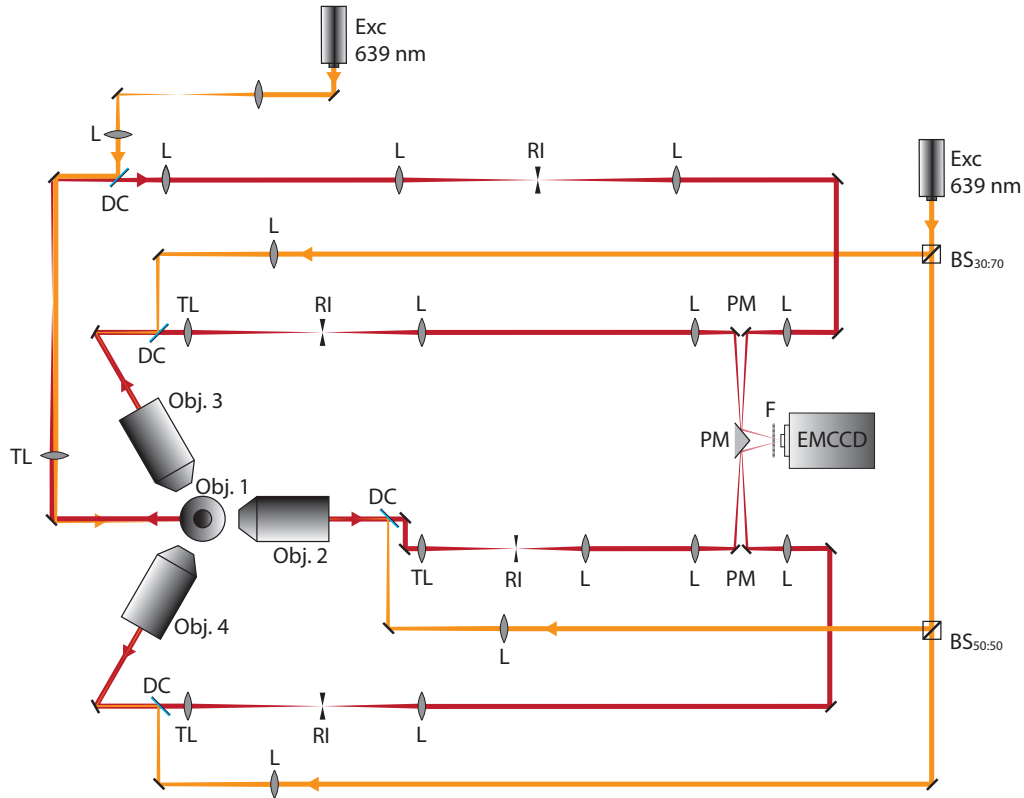


Figure 3.9: Excitation and detection beam paths

The excitation (orange) by all objective lenses is separated from the detection (red) by dichroic mirrors (DC). One of the two equivalent laser devices illuminates from below through objective lens 1. The intensity of the other laser is split almost equally into three by beam splitters (BS), one line for each upper objective lens. The size of the excitation beams and the magnification of the detection is adjusted by various lenses (L). Each objective lens has its corresponding tube lens (TL). The detection beam paths are individually cropped by rectangular irises. They are brought close by perpendicular oriented mirrors (PM) so each fills 1/4 of the EMCCD chip. The camera chip is covered by various filters (F) in order to minimize noise effects.

3.3.5 Conversion factor between photons and camera counts

The output of the EMCCD camera is an electron multiplied and noise influenced number of counts N_C , which is proportional to the detected number of photons N_P . The conversion factor between photons and counts varies for the selected EM gain. It can be calculated from a correction factor C and a multiplication noise factor F [43, 44, 51].

$$N_P = \frac{F^2}{C} N_C \quad (3.16)$$

The correction factor C is the slope of the linear relationship between the mean pixel value \bar{N}_C and its variance σ_C^2 .

$$\frac{\sigma_C^2}{\bar{N}_C} = C \quad (3.17)$$

For a sufficiently high EM gain the multiplication noise factor, also referred to as excess noise, converges to $F = \sqrt{2}$ [44].

3.3.6 Electronic control of the setup

The setup has several electronic devices which need to be controlled. Next to the camera and the z -stage there are all together twelve linear positioners (objective lenses 2–4 with three positioners each, objective lens 1 with one and the sample stage with two). All of them can be digitally controlled by commands instead of an analog voltage input. The travel control as well as the camera read out is done by LabVIEW (National Instruments).

The linear stages (positioners and z -stage) are divided in two groups: One for the control of the upper objective lenses and a second for the sample stage and the bottom objective lens. Once the sample is mounted and the upper objective lenses are adjusted to the same spot, the fine tuning is just done by the second group. The corresponding user interface is shown at figure 3.10.

In the routine for controlling the camera various parameters can be set: exposure time, temperature, fan mode, EMCCD gain, preamplifier gain, vertical shift speed and a baseline clamp. Next to a live view which shows the latest picture also a measurement with a given number of frames can be run, shown at figure 3.11. The images are saved clustered in binary files at a chosen location, in parallel to the 30 ms image sequence.

The integration of all devices into the same program allows combined control of them. With one of the subroutines, the sample stage and the camera can be

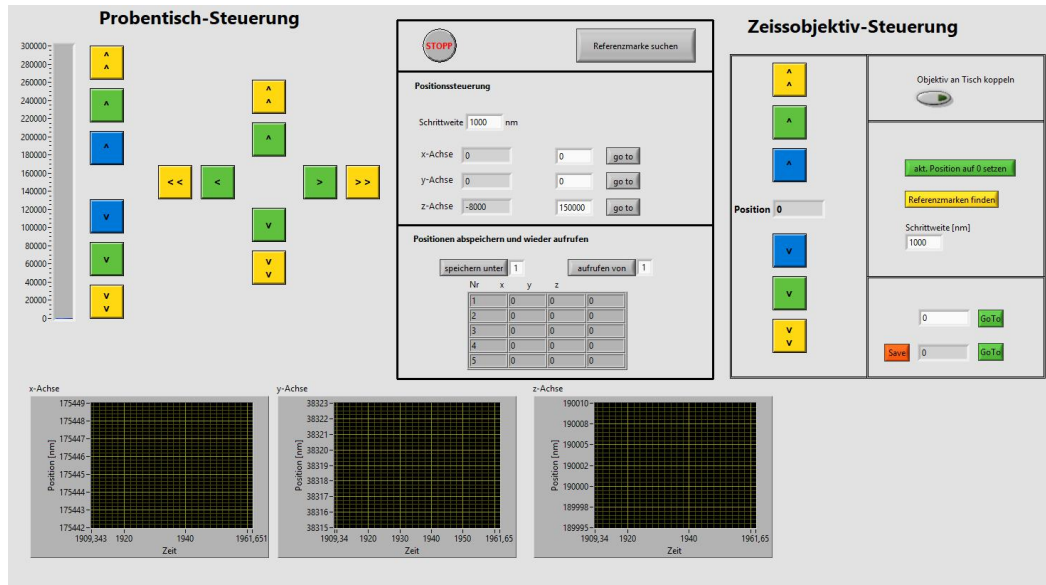


Figure 3.10: User interface for control of sample and bottom objective lens

controlled simultaneously, figure 3.12. A position list can be loaded and at each of these given positions an image is taken.

The subsequent evaluation of the data is explained in chapter 4.

Chapter 3 Stereo 3D-SMS microscopy

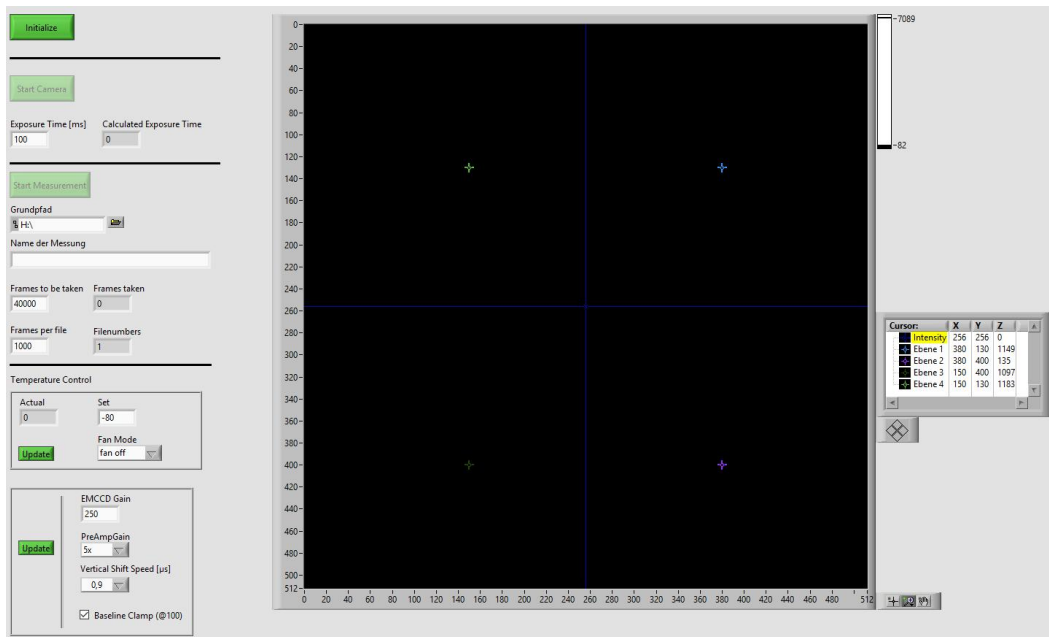


Figure 3.11: User interface for continuous measurements

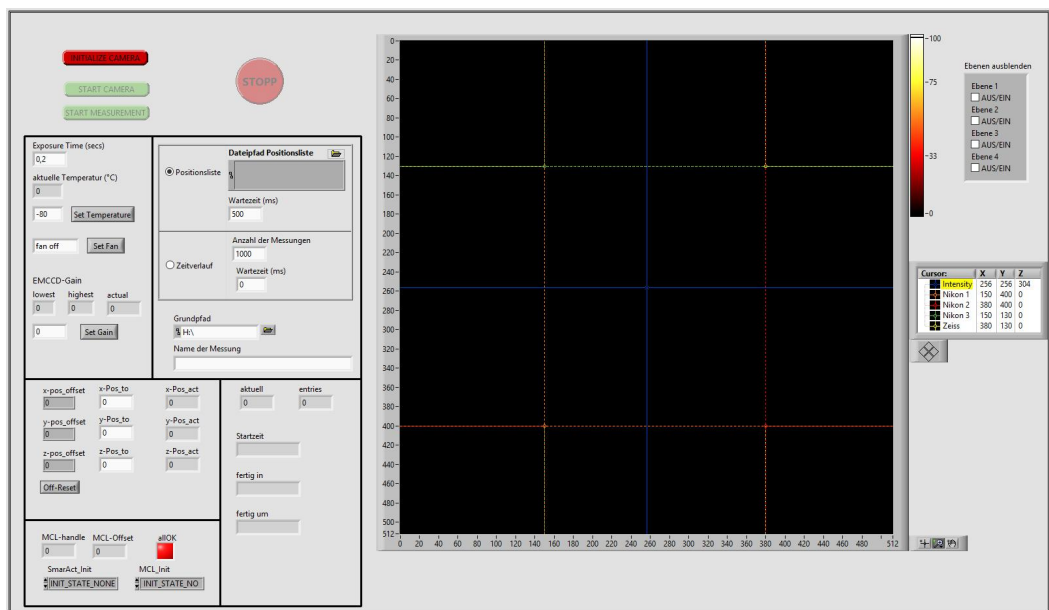


Figure 3.12: User interface for control of sample and bottom objective lens

3.4 Samples and buffer

The presented concept of stereo view is based upon the detection of point source like emitters. This could either be single fluorophores, fluorescent beads or other small round shape particles.

3.4.1 Fluorescent beads

For the given combination of excitation laser, dichroic mirror and filters the microspheres Dark Red (FluoSpheres, Carboxylate-Modified, Life Technologies) are suitable. These beads have the excitation peak at $\lambda = 660$ nm, the emission peak at $\lambda = 680$ nm and a nominal diameter of $\varnothing = 200$ nm (F8807) or 40 nm (F8789). They can be attached to glass by covering the surface with a layer of poly-L-lysine (P8920, Sigma-Aldrich) in beforehand. The particle density can be adjusted by incubation time, volume and dilution of the solution.

3.4.2 Cells and their preparation

For the SMS concept of switching and localizing single fluorophores, the dye Alexa Fluor 647 (Invitrogen) is well suited, detailed in section 2.1.2. For staining specific parts within a cell the concept of immunostaining with primary and secondary antibody is used according to standard protocols. After fixing the cell and permeabilizing the membrane, the primary antibody which couples to the chosen target is added for about an hour. After repeated washing the secondary antibody, coupled with the dye, is added for another hour, which connects to specific open linkers of the primary antibody.

3.4.3 Buffer solution for SMS imaging

The switching behavior and the photostability of the dye crucially depends on the surrounding buffer medium. Therefore, a combination of an oxygen scavenging system (glucose oxidase and catalase (GLOX)) in order to achieve a low oxygen environment and primary thiol (mercaptoethylamine (MEA)) is used [35].

For stabilizing the pH-value a combination of protocatechuic acid (PCA) and protocatechuic dioxygenase (PCD) is added [52]. The also suggested cyclooctatetraene (COT) was not used because of its high volatility and health hazard.

The final imaging buffer contains the following stock solutions:

TN-buffer

- 50 mM Tris (252859, Sigma Aldrich)
- 10 mM NaCl (71380, Sigma Aldrich)
- H₂O
- adjusted to pH 7.5 by 1 M HCl
- stored at room temperature

base imaging buffer

- 10% (w/v) glucose (D9434, Sigma Aldrich)
- TN-buffer
- stored at room temperature

oxygen scavenging system (GLOX)

- 4 mg/ml catalase (C100, Sigma Aldrich)
- 50 mg/ml glucose oxidase (G2133, Sigma Aldrich)
- TN-buffer
- stored at +4 °C

mercaptoethylamine (MEA)

- 1 M cysteamine (30070, Sigma Aldrich)
- HCl 37% 1:12
- adjusted to pH 7.5 by 1 M HCl
- stored at +4 °C

protocatechuic acid (PCA) solution

- 100 mM protocatechuic acid (37580, Sigma Aldrich)
- H₂O
- adjusted to pH 9 by 1 M NaOH
- stored at +4 °C

protocatechuic dioxygenase (PCD) solution

- 50% H₂O
- 50 mM Tris (252859, Sigma Aldrich)

- adjusted to pH 8 by 1 M HCl
- 2 mM EDTA (E6758, Sigma-Aldrich)
- 100 mM KCl (60128, Sigma-Aldrich)
- 50% glycerol (104095, Merck Millipore)
- 5 μ M protocatechuic dioxygenase (P8279, Sigma Aldrich)
- stored at -20 °C

The final imaging buffer consists of the base imaging buffer mixed with GLOX (40 μ g/ml catalase, 0.5 mg/ml glucose oxidase), MEA (10 mM cysteamine), PCD-solution (50 nM PCD) and PCA-solution (2.5 mM PCA).

The refractive index of the buffer solution is $n_{\text{buffer}} = 1.348$, measured by an Abbe refractometer (AR4, A.Krüss Optronic GmbH). This is in good accordance to the given value $n_{\text{lit}} = 1.3477$ for an aqueous solution with 10 mass percent glucose [53]. The measured refractive index is $\Delta n = 0.016$ higher than the one of pure water $n_{\text{water}} = 1.3325$.

Chapter 4

Data analysis framework

The output, when measuring with the microscope setup, is a set of 2D images or frames from the camera. Each quarter of a single frame contains the image of one of the objective lenses. The central regions of the quarters are assigned to a fourfold 2D data set for each frame. These are the raw data for calculating the three-dimensional representation of the sample.

The simulation of artificial raw data allows to evaluate the potentials of the setup in terms of resolution and imaging volume. The subsequent analysis is mainly the same as for the real data.

The analysis splits into different steps like localizing, determining the transformation parameter, correlating the detection patterns and finally estimating the most likely emitter position. This procedure can be used for data from cell measurement as well as for particle tracking.

4.1 Simulation of artificial data

For the simulation of artificial raw data first the position \vec{r} of an emitter in the basic coordinate system is randomly or specifically chosen. The emission of the specified total number of photons is assumed as isotropic.

For a known orientation of the objective lenses, position \vec{r} can be transformed to \vec{r}' in the respective detection coordinate systems. The detection pattern, which can be calculated following section 2.2, is located at position x'/y' and its shape depends on the distance of the emitter with respect to the focal plane. The number of detected photons enclosed in each pattern is calculated from the total number of emitted photons and the aperture angle of each objective lens.

Since the camera is pixelated, the theoretically calculated detection pattern is binned accordingly and the pixel counts are rounded to integer values. In order to include shot noise these noiseless image values are replaced by values drawn from

a Poisson distribution with the mean equal to the pixel count. In order to simulate the electronic readout noise also a white gaussian noise is added to each pixel. Its mean parameter and standard deviation is estimated from typical EMCCD measurements. The resulting image is comparable to the real raw data obtained from the setup and can be handled equally.

A repeated image calculation for the same emitter position is differently affected by the noise. Doing the calculation several times gives the opportunity to estimate the standard deviation or FWHM for determining the spatial position of the emitter.

4.2 Image analysis - from raw data to a 3D-image

There are different possible procedures to compute the 3D emitter position \vec{r} from the detection patterns, carried out in section 3.1.1. The one used is to first localize the center \vec{R}' of the detection patterns in each detection plane. With this the emitter position is calculated from a system of linear equations (equation 3.2)

$$\mathbf{M} \cdot \vec{r} = \vec{R}',$$

solved by weighted least square fitting (equation 3.10)

$$\min_{\vec{r}} \sum_{i=1}^{2K} \frac{\left((\mathbf{M}\vec{r})_i - \vec{R}_i \right)^2 N_i}{(\sigma_{G_i})^2}.$$

The minimization of the equation is done by the use of the 'fminsearch' function in numerical computing environment Matlab (MathWorks). This function is based upon the Nelder-Mead simplex algorithm [54]. For solving the SLE without weighting the much faster 'mldivide' resp. '\' can be used which takes advantage of symmetries in the problem and dispatches these to an appropriate solver.

All following subsections are about getting the needed values for solving these equations the best, i.e. with the minimal remaining square sum.

4.2.1 2D localization of the emitter position

In order to estimate the center position of the detection pattern several steps are necessary. First, the background of the image gets subtracted. Next, a segmentation to areas of high values determines the individual events. Finally a 2D gaussian is fitted to these subROIs, following Thompson et al. [45]. In case the localization

converges, the estimated center position of a successful approximation is saved in the unit of pixel in a list of events. With it, the number of the actual frame and the weighted and unweighted sum of counts inside the detection pattern is saved. The counts are converted to the number of photons by the gain related conversion factor of the EMCCD camera.

A possible drift during the measurement caused either by the objective lens or by the sample can be corrected. For each detection plane a fully data-driven method for the drift detection and correction will be used [55].

4.2.2 Determining the transformation parameters

The correlation of the detection coordinate systems in respect to the basis coordinate system, and with it to each other, is described by several parameters:

rotation angles β_i , γ_i and δ_i (3 parameters per detection path)

The rotation angles of the transformation matrix M and their expected values are explained in detail in section 3.3.1 and will be determined for all four objective lenses.

effective pixel side lengths (2 parameter per detection path)

In classical microscopes, with the detection plane parallel to the cover glass, the pixel side lengths can be measured using a calibration grid. In this setup such a calibration would be much more complicated due to the tilted perspectives. Hence, the unit conversion from pixel to nanometer respectively the pixel side lengths are fitted as transformation parameters.

position of the coordinate system origin (2 parameters per detection path)

The origin of the basic coordinate system defines the center of the particular detection coordinate systems. When cropping the four images from the camera readout, the centers of these fields of view coincident approximately with the origin. For the fine tuning of the offsets, these values are also handled as transformation parameters.

All together results to a total number of $4 \cdot (3 + 2 + 2) = 28$ unknowns for the transformation. Because of the high number of degrees of freedom, which are needed to find the optimum arrangement of the objective lenses in this proof of concept setup, the setup lacks high reproducibility. Therefore, these values vary slightly from one measurement to the next and need do be fitted again for each of

it. But with several hundreds or up to thousands of emitters, spread over the whole focal volume, they can be calculated directly from the measurement data, even if both the transformation parameters and the emitter's positions \vec{r} are unknown. For this, the transformation parameters are optimized in such a way, that the mean minimal value of the least square fittings for all detected emitters gets as small as possible.

With multiple events per frame and unadjusted parameters it is difficult to decide which localized 2D positions belong to each other, which is carried out in detail in the following section. For a first-order approximation bright solitary events close to the center are chosen because they have a high probability to be correlated. With this, more or less accurate parameters for the correlation of multiple emitter can be determined, followed by a fine tuning of the transformation parameters.

In order to get a rough pre-estimation of the parameters, for example for serving as a starting point for the fitting, it would be best to know both \vec{r} and \vec{R}' . This can be achieved by measuring a fluorescent bead at various known positions throughout the detection volume. By localizing the centers of the detection patterns just the transformation parameters remain unknown and can easily be approximated.

4.2.3 Correlation in case of multiple emitter

If there are multiple emitters measured in the same frame, it needs to be specified, which of the detection patterns from the different detection planes are correlated. With n emitters per frame there are supposed to be equivalent detection patterns in each of the four images. If it is not known which of these patterns belong to each other, there are n^4 possible combinations.

Since just the x/y -position in the detection coordinate system is known, the emitter can be located on a normal through this point. A line can be set up for all n x/y -positions in each detection coordinate system and transformed to the basis coordinate system. These lines are shown in figure 5.11, just with the differences that they have been transformed into the other detection planes. However, a small distance between two lines in the basic coordinate system is a good indication that the corresponding localized positions belong to the same emitter. Therefore, first, pairs of lines are identified which are close, i.e. which have a distance below a certain threshold. Then, these pairs are compared to each other to find sets of four, which have the smallest distance and are most likely correlated. These sets are used for solving the SLE by least squares fitting, which then gives the 3D emitter position. One event is just allowed to take part in one correlation.

Due to the presorting by the line distance calculation, the number of possible combination n^4 can be reduced significantly. Therefore, the maximum number of emitters per frame is not limited by the correlation analysis. Instead, it is limited because detection patterns in all imaging directions (i.e. from all perspectives) need to be sufficiently separated.

4.2.4 Final calculation of the most likely emitter position

Once the correlation of the localized positions is defined and the transformation parameters are optimized the most likely emitter position can be calculated. For this, equation 3.10 is used which includes the weighting of the localized positions. The number of photons N for the weighting step is calculated when doing the localization. In order to get an estimation for the standard deviation σ_G the emitter position will be predetermined by an unweighted least square fitting. By transforming this position back to the detection coordinate system the distance from the detection plane is known. Hereby it is possible to get the shape of the expected PSF and the corresponding standard deviation σ_G .

Detection patterns which are not used for combinations of all four detecting objective lenses can be used in the same way for combinations of three detecting objective lenses. This can be the case when the emitter is too far apart from one of the detection planes but still in focus of the other objective lenses.

The mean or total photon number of the correlated detection patterns as well as the goodness of the weighted least square fitting can serve as quality criterion.

4.2.5 Following a track

When tracking moving particles the procedure is the same as before. To follow the track of a single particle the distance of the positions from one frame to the next needs to be below a given threshold. No larger discontinuities, meaning missing frames, are allowed. Consequently, following several particles simultaneously is easily possible.

Typically, various emitters are located throughout the detection volume. So also in the case of tracking, it is possible to calculate the transformation parameters from the measured data.

Chapter 5

Stereo 3D-SMS: Characterization and first imaging examples

Subsequent to a detailed planning phase and the construction of the setup, practical measurements are performed and the recorded data is analyzed.

One is the evaluation of the setup properties. This includes the measurement of the actual point spread function, the stability of the setup, the focal shift for the bottom objective lens and the camera conversion factor.

Another is the quantification of the setup performance in terms of possible resolution. This can be done on a theoretical basis as well as on an experimental one.

Finally, two different areas of application are presented. First thing is the simultaneous tracking of multiple moving fluorescent emitters. The second is the measurement of different cellular structures which are fluorescent labeled: nuclear lamins, vimentin filaments, mitochondria organelles and gp210 in the nuclear pore complex.

5.1 Comparison of the theoretically calculated and the actually measured PSF

One characteristic of the setup is the comparatively low NA of the objective lenses which results in a great focal depth, section 2.3.3. The theoretical detection PSF can be calculated from the 3D field distribution, equations 2.3 and 2.4.

The theoretical and actual PSFs by the water dipping objective lenses are illustrated in figure 5.1. The color maps of the images are logarithmically scaled and the scale bars indicate $2\ \mu\text{m}$. The illustrations cover $z = 9\ \mu\text{m}$ in depth and the PSFs are in both cases rotationally symmetric along the central z -axis.

The theoretical detection PSF in figure 5.1a is calculated for an objective lens with NA 0.8 in a $n_{\text{water}} = 1.33$ medium. At distances of $z \approx \pm 2.5\ \mu\text{m}$ from the center the

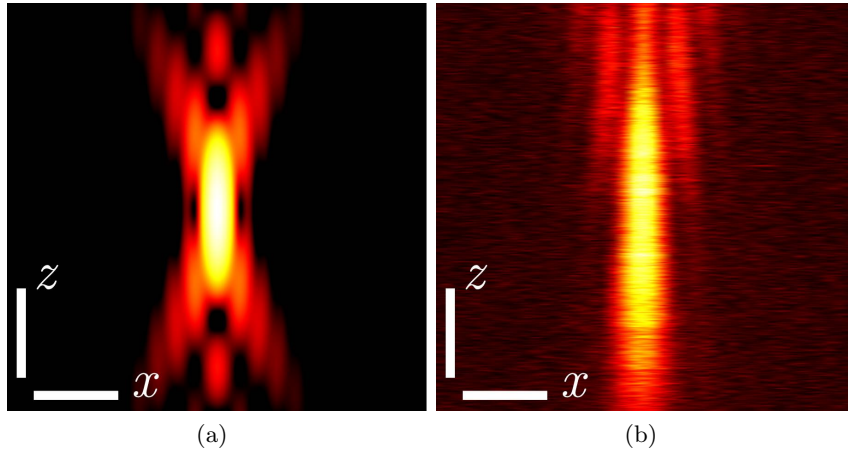


Figure 5.1: Comparison of the theoretical and experimental PSF
 a) Theoretically calculated PSF, detected by an objective lens with NA 0.8 in a $n_{\text{water}} = 1.33$ medium is axial symmetric along the z -axis.
 b) Experimentally measured PSF by scanning a NA 0.8 water objective lens over a $\varnothing = 45$ nm fluorescent bead. The refractive index of the medium is $n_{\text{buffer}} = 1.348$. Due to spherical aberrations the axial intensity distribution changes significantly, however the axial symmetry remains.
 all scale bars indicate $2\ \mu\text{m}$

axial first order minima are located. The corresponding x/y intensity distribution approximates a ring-shape with a distinct central intensity minimum.

This theoretical detection PSF holds for an aberration-free imaging system. However, the non-perfect index matching of the buffer, consisting of 10% glucose which increases the refractive index to $n_{\text{buffer}} = 1.348$, section 3.4.3, introduces spherical aberrations. This affects the actual PSF in the setup, which is measured by scanning the objective lens with $\Delta z = 20$ nm step size while imaging a $\varnothing = 45$ nm fluorescent bead, shown at figure 5.1b. The PSF is much more elongated in the axial direction than predicted and the side lobes are much weaker. Due to this, the intensity maximum is located at the center position throughout the full axial range shown. Therefore, each detected intensity pattern can be fitted by a Gaussian. This clearly extends the axial depth in which localization is feasible.

When measuring the PSF with pure water instead of the standard buffer, its shape changes significantly, figure 5.2. The extension in axial direction is as expected from the theoretical calculations. However, in the x/y -plane the detection pattern is not point-symmetric anymore but seems to be cut on one side. This

5.1 Comparison of the theoretically calculated and the actually measured PSF

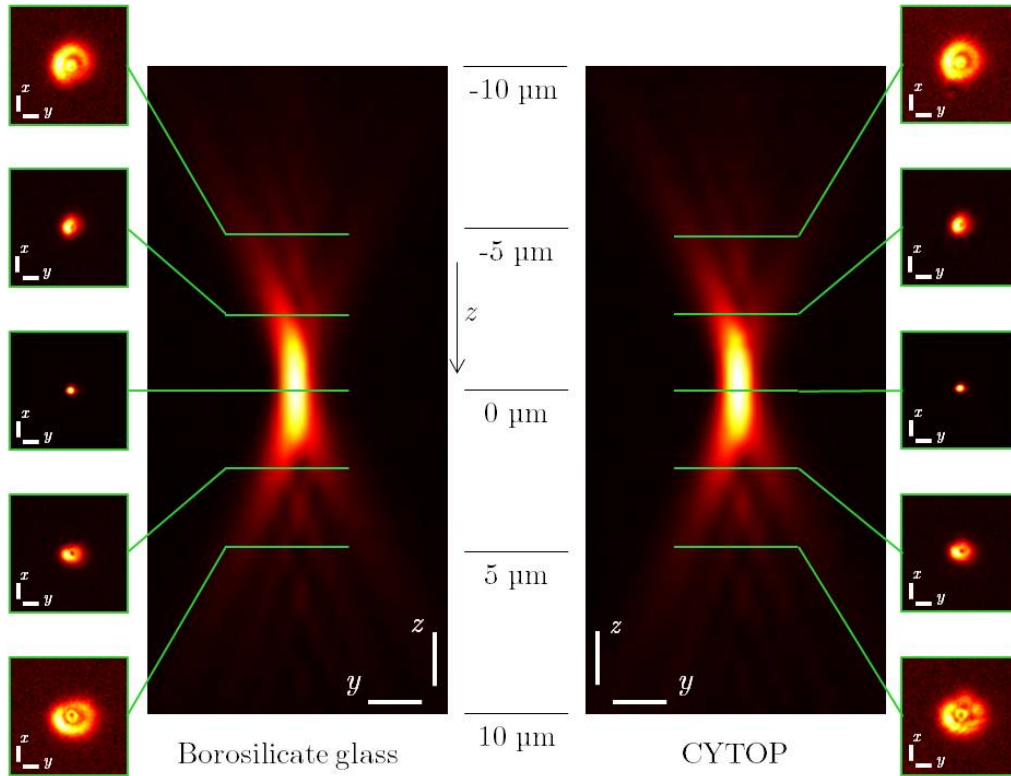


Figure 5.2: Comparison of cover glasses made of borosilicate glass or CYTOP™. left part: Detected PSF when measuring a fluorescent bead in a $n_{\text{water}} = 1.33$ medium on a borosilicate cover glass by one of the dipping objective lenses. The x/y detection patterns seem to be cut on one side. right part: Use of a $n_{\text{CYTOP}} = 1.34$ cover glass to eliminated any possible reflections or cut-offs towards the dipping objective lenses. However, the asymmetry of the detected PSF does not change significantly.

characteristic is almost unaffected by the type of cover glass used: borosilicate glass with $n_{\text{glass}} = 1.473$ or CYTOP™ with $n_{\text{CYTOP}} = 1.34$ (sec. 3.3.3). In the latter and almost refractive index matched case any reflections or cut-offs by the cover glass were supposed to be eliminated. The asymmetry of the detection pattern leads to a localization error. This is why all measurements are done with at least 10% glucose in the aqueous buffer solution, leading to a symmetric detection PSF (figure 5.1b). In order reduce autofluorescence the cover glass in the following is made of quartz instead of borosilicate, but this does not change the shape of the actual PSF.

5.2 Stability of the setup

When characterizing the stability of the setup, two timescales are relevant. On the short time scale from one frame to the next (tens of milliseconds), vibrations in the setup especially between objective lens and sample may lead to blurring of the emitter images, which directly affect the localization precision reachable for each objective lens. On the long time scale of the whole measurement, up to tens of minutes, drift of the sample or the individual objective lenses becomes most important. This can be caused, for example, by temperature fluctuations of the surrounding or the unwanted heating of the objective lenses by the laser light.

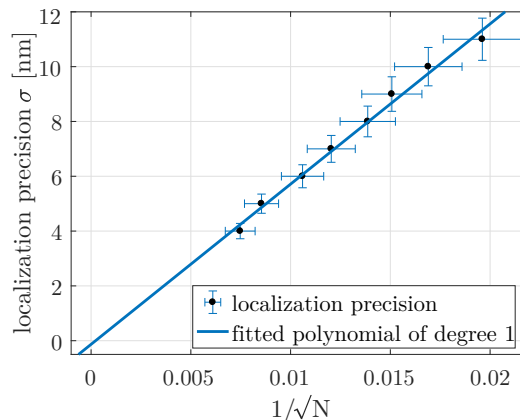


Figure 5.3: To illustrate the system stability on the short time scale a fluorescent bead is measured with different detected photon numbers N 100 times in a row. The standard deviation of these sequences is plotted with respect to $1/\sqrt{N}$ (black marks). The blue line shows the linear regression.

The possible precision of the localization scales with the square root of the number of detected photons, section 2.3. By measuring a fixed bead with different numbers of detected photons 100 times in a row, the standard deviation for each photon number can be calculated. This corresponds to the localization precision. Vibrations in the system would add an offset and a deviation to the slope of the standard deviation. The achieved localization precisions are plotted in figure 5.3 with respect to the square root of the photon number exemplary for one objective lens and axis. The linear regression does not show any impact of vibrations for the evaluated range of photon numbers which covers the expected photon numbers of the setup.

The long time stability of the setup is sketch in figure 5.4. After a short time of relaxation, a fluorescent bead $\varnothing = 200$ nm is imaged 1000 times over a time period

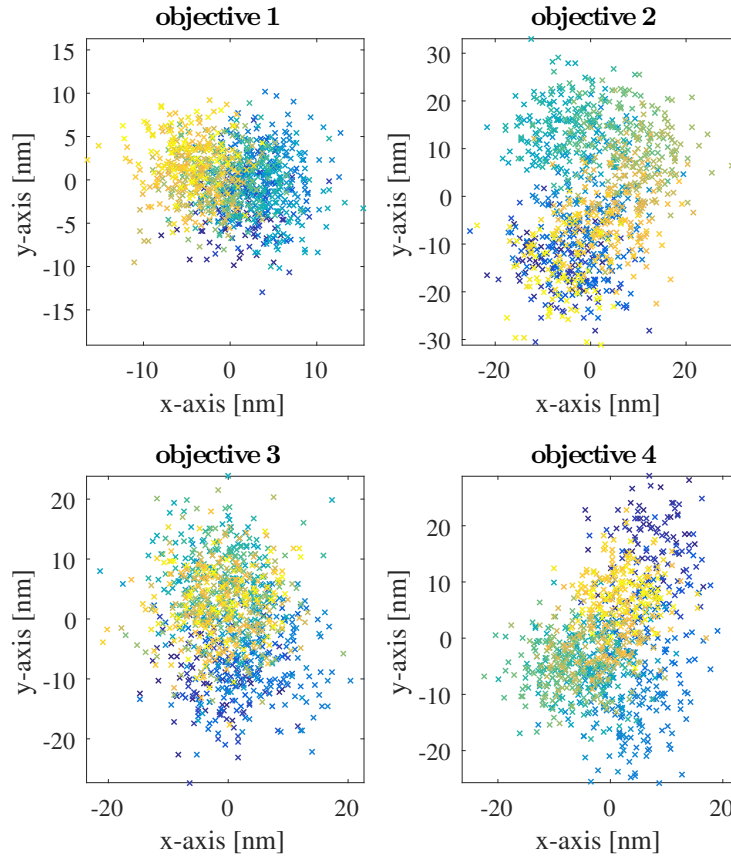


Figure 5.4: The system stability on a long time scale is measured by imaging a $\varnothing = 200$ nm bead 1000 times within 20 minutes. The localized bead positions are plotted for each objective lens with a time dependent color code (blue to yellow).

of 20 minutes. The localized positions of the bead for each objective lens are plotted with a time dependent color code (blue to yellow). It can be seen that localized positions from consecutive frames scatter on the scale of 10 nm. Additionally, a small drift of 10–40 nm over the measurement time is visible. The scattering is in the range of the expected localization precision (about 5 nm) and is therefore inherent to the method. the drift can be corrected for, section 4.2.

5.3 Focal shift of the bottom objective lens

Depending on the actual application it might be necessary to place the common focus point at different depths inside the sample, eg. for imaging thick objects. When

focussing through an optical boundary, a vertical movement of this boundary leads to a shifting of the focal distance, section 3.2.1.

For the case of the bottom objective lens the fluorescent light passes two optical boundaries: medium/glass and glass/air. This is just the reverse view to the light path than in figure 3.2. Since the intermediate glass layer can be neglected, the beam path goes from the optically thicker sample buffer to the optically thinner air. This is the opposite case than plotted in figure 3.3 (water/oil boundary) which is why the inverted slope of the focal shift is expected.

Beside calculating, the actual focal position can also be measured. For this, two cover glasses with fluorescent beads attached to the surfaces are placed in several known distances facing each other with buffer medium in between. From the necessary travel of the objective lens to focus the different layers, the focal shift can be calculated. The results are plotted in figure 5.5.

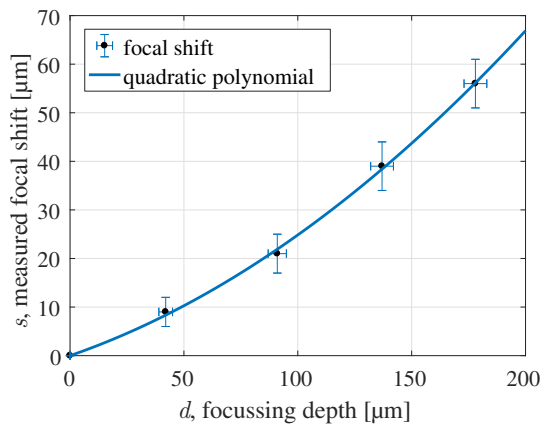


Figure 5.5: Measured focal shift of the bottom objective lens

The data points s of the focal shift with respect to the focussing depth d can be fitted by the following quadratic polynomial:

$$s = 8.60 \cdot 10^{-4} \cdot d^2 + 0.16 \cdot d + 2.01 \cdot 10^{-6} \quad (5.1)$$

This formula can be used to automatically correct for an occurring focal shift when moving the coverslip in the axial direction of the bottom air immersion objective lens.

5.4 Calculating the EMCCD camera conversion factor

The conversion factor between detected photons and camera pixel counts is proportional to the slope of the variance of a pixel count with respect to the mean pixel value, section 3.3.5. These values are calculated by measuring a time invariant fluorescent light source over several numbers of frames. The linear slope between the variance and the mean value for each pixel gives the correction factor C .

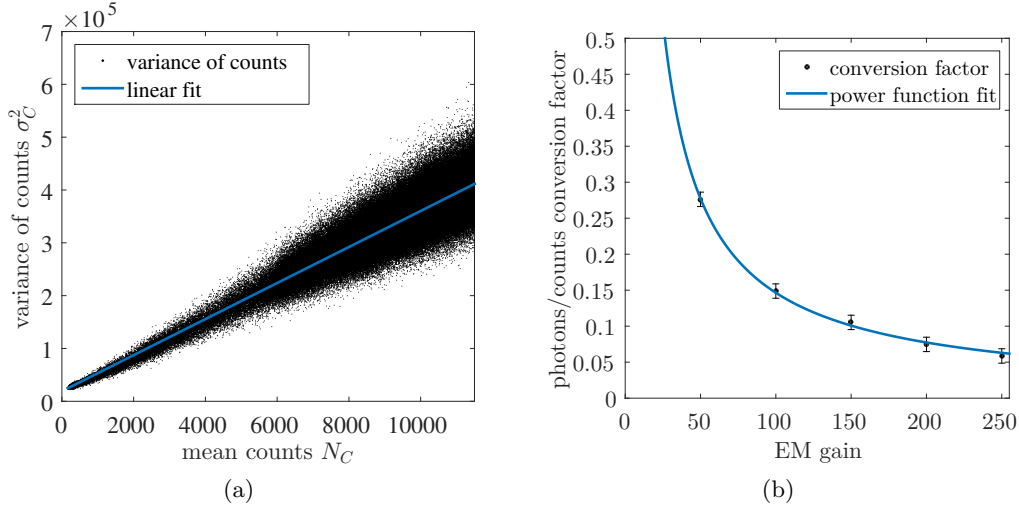


Figure 5.6: EMCCD camera conversion factor

- The slope of the count variance per pixel σ_C^2 in respect to the mean count number \bar{N}_C gives the correction factor C . This value corresponds to the conversion factor of counts to photons by $\frac{F^2}{C}$, equation 3.16
- The conversion factor at different EM Gains can be fitted by a power function, the gain dependent conversion formula.

The slope at figure 5.6a of $C = 34.1 \pm 0.5$, exemplary for EM gain 250, corresponds to a conversion factor from counts to photons of 0.058, equation 3.16. The progression of the conversion factors for several EM gains can be expressed by a power function, figure 5.6b. This gives the following gain dependent conversion formula.

$$\text{conversion factor} = 10.19 \cdot \text{EM Gain}^{-0.921}$$

5.5 Theoretical simulation of the setup capabilities

The setup capabilities namely the possible precision within a specific detection volume can either be theoretically calculated or practically measured. For the the-

oretical calculation of these values the simulation of the raw data is done following section 4.1. The number of detected photons for the specific objective lenses are derived from the number of photons typically detected in SMS microscopy from an Alexa Fluor 647 molecule by a NA 1.4, oil immersion objective lens, $N \approx 5200$ photons [35]. This is about 2900 photons for the bottom objective lens and about 1700 photons for each of the upper objective lenses. The transformation parameters are set to the values given in section 3.3.1 with an uplifting angle of $\beta = 125.5^\circ$.

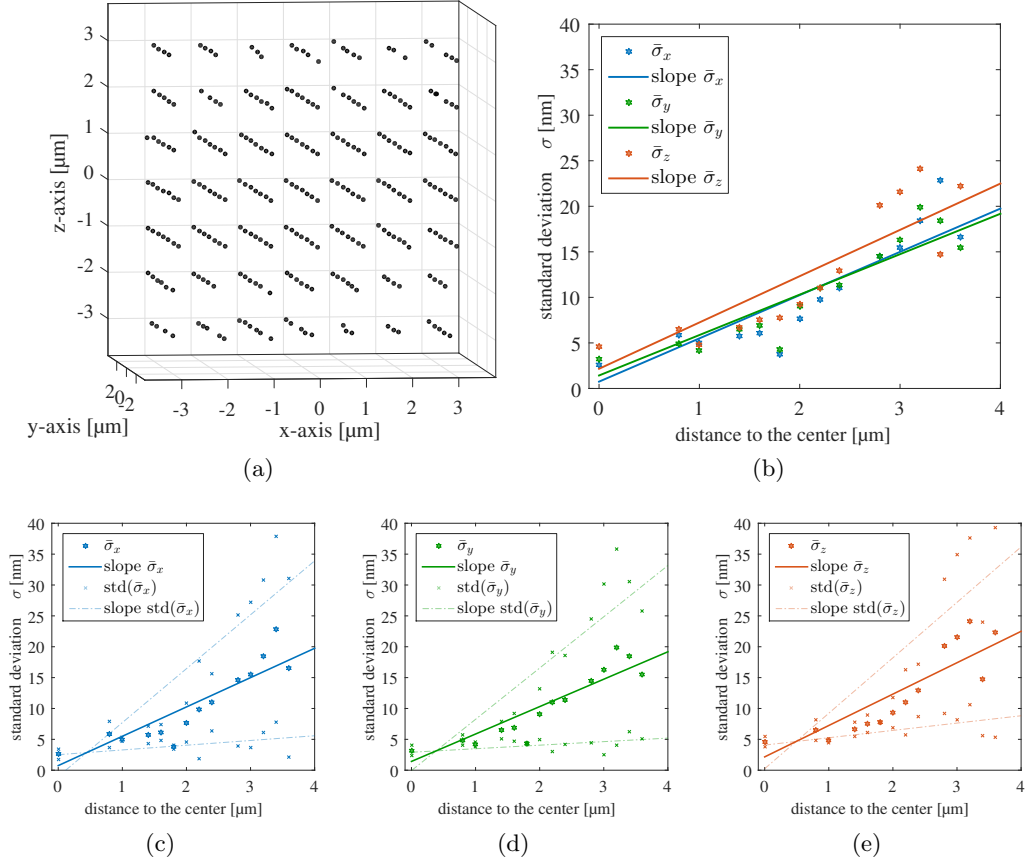


Figure 5.7: Simulation of the setup capabilities

- a) Mean values of the determined emitter positions at each grid point of a $6 \times 6 \times 6 \mu\text{m}^3$ cube ($\Delta_{x,y,z} = 1 \mu\text{m}$, black marks).
- b) Standard deviation of the mean values averaged over 200 nm with respect to the distance from the center, separated for each spatial direction. The slopes are illustrated by lines.
- c-e) Mean values of subfigure b) together with their respective standard deviations, separated plot for each coordinate.

For the same emitter position, 10 recalculations are made, randomly influenced

5.5 Theoretical simulation of the setup capabilities

by noise which is a combination of Poisson noise of the signal and white gaussian noise for all detector pixel. After localizing and solving the system of linear equations for all repetitions, the standard deviation of all calculated emitter positions gives the localization precision. It should be noted, that the known emitter position \vec{r} is only used for calculating the raw data, and not for the subsequent position estimation.

The procedure for calculating the localization precision is done for various points on a cubic grid within the detection volume. Hereby, the dependency of the localization precision on the distance from the common focal spot can be examined.

In figure 5.7a the determined emitter positions on a $6 \times 6 \times 6 \mu\text{m}^3$ cubic grid with $\Delta_{x,y,z} = 1 \mu\text{m}$ step size are illustrated. The mean value of the positions in each grid point is marked black. While in the center all emitters are located, on the edges several positions are missing. This is caused by the strong decrease of intensity and the ring like PSF for blurred signals as shown on the left in figure 5.1.

The standard deviation for each grid point is calculated for all three cartesian directions. This is a good tool for measuring and illustrating the performance of the setup over an extended volume. The progression of the standard deviation with respect to the distance from the center is plotted in figure 5.7b. For the sake of clarity, the standard deviations are averaged ($\bar{\sigma}_{x/y/z}$) over distance intervals of 200 nm. The standard deviations of these mean values ($\text{std}(\bar{\sigma}_{x/y/z})$) are shown in figures 5.7c/d/e, separated for each coordinate.

In the center region of about $|\vec{r}| \leq 2 \mu\text{m}$ distance the calculated performance of the setup is best with standard deviations of 5–10 nm. This is independent of the cartesian direction. Even though the objective lens arrangement does not exactly correspond to the tetrahedron shape, the simulated localization precision is isotropic.

For an emitter in the center position, its image in all four detection planes is in focus, which represents ideal conditions for the determination of its true position. With further distance, the detection pattern by one or more objective lenses gets blurred and is not gaussian anymore, caused by the particular distance of its focal plane to the emitter position. This degrades the localization precision and significantly reduces the overall performance. For that reason, the mean standard deviation increases to about 25 nm and also the standard deviation of this distance-dependent average increases. Positions further apart than the specified volume are not correctly detected anymore in the simulated case.

For later comparison, the mean numbers of detected photons, estimated by the anal-

ysis routine, are $N_1 = 3300$ photons for the bottom objective lens and $N_{2,3,4} = 2700$ photons for each of the upper objective lenses.

5.6 Experimental quantification of the setup capability

The quantification of the setup capabilities can also be done experimentally with the same procedure as in the previous theoretical case but using the detected signal of fluorescent beads. The illumination intensity and the exposure time of the camera are adjusted in a way that the number of detected photons is comparable to the signal of the Alexa Fluor 647 dye. A single bead of $\varnothing = 45$ nm, attached to a cover glass and mounted in a 10% glucose solution, is moved on a cubic grid and each position is measured 10 times in a row. After calculating the emitter position from the detected images for each grid point, their standard deviation can be determined, which is a measure for the microscope's localization precision.

The measured $8 \times 8 \times 8 \mu\text{m}^3$ grid with a spacing of $\Delta_{x,y,z} = 1 \mu\text{m}$ is shown in figure 5.8a. The mean value at each grid point determined from the single measurements is marked black. All positions are determined and the scanned cube can be nicely reproduced without any distortions.

When measuring with 10% glucose in water same as with the standard buffer, section 3.4.3, the PSF is significantly elongated, figure 5.1b, and the first order minimum in the axial direction is much weaker than in the case of pure water. Due to that, the detection patterns of fluorescent beads, which are further apart from the particular focal planes, still have a gaussian rather than a ring like shape. This significantly increases the distance to the focal planes, in which localization can be performed reliably. Therefore, the usable volume is larger compared to the simulation.

In figure 5.8b the standard deviations of the grid points are plotted with respect to the distance to the center resp. the common focal spot. Similar to the simulated data the standard deviations are averaged for clarity over bins of 300 nm, $\bar{\sigma}_{x/y/z}$. For the sake of completeness, the standard deviations $\text{std}(\bar{\sigma}_{x/y/z})$ of these mean values are shown separated for x , y and z in figures 5.8c/d/e.

The precision of $\sigma_{x,y,z} = 5 - 15$ nm is almost isotropic over the whole volume and linearly increases with larger distance. Therefore, the setup is able to measure emitter positions at least $|\vec{r}| = 7 \mu\text{m}$ away from the center, so a spherical volume with $14 \mu\text{m}$ diameter. The mean number of detected photons are $N_1 = 3500$ photons for the bottom objective lens and $N_{2,3,4} = 2900$ photons for each of the upper objective

5.6 Experimental quantification of the setup capability

lenses.

Current research is done to improve the photon number emitted by switchable fluorophores. In addition, in tracking experiments a higher number of photons is possible. In order to demonstrate the potential of the setup, the characterization was repeated with brighter emitters, namely $\varnothing = 200$ nm fluorescent beads. As shown by the $16 \times 16 \times 16 \mu\text{m}^3$ cubic grid in figure 5.9 with $\Delta_{x,y,z} = 2 \mu\text{m}$, the possible distances for successful emitter localization is distinctly extended, compared to figure 5.8. The standard deviation decreases isotropically to $\sigma_{x,y,z} = 3 - 15$ nm in a distance from the center of up to $|\vec{r}| = 14 \mu\text{m}$. The mean number of detected photons is $N_1 = 10000$ photons and $N_{2,3,4} = 10700$ photons. By the use of sufficiently bright emitters, the setup is capable to measure a spherical volume of $> 26 \mu\text{m}$ diameter with high precision and without any need for scanning.

When measuring a fluorescent bead at specified positions like the presented cubic grids, both \vec{r} and \vec{R}' in equation 3.2 are known. With a sufficiently high number of different positions in space the transformation parameters contained in \mathbf{M} can get calculated, even if they are just estimated very imprecisely in advance. These values can be taken as starting points for the fine tuning in the particular measurements, like cells or tracking, with the use of random unknown emitter positions.

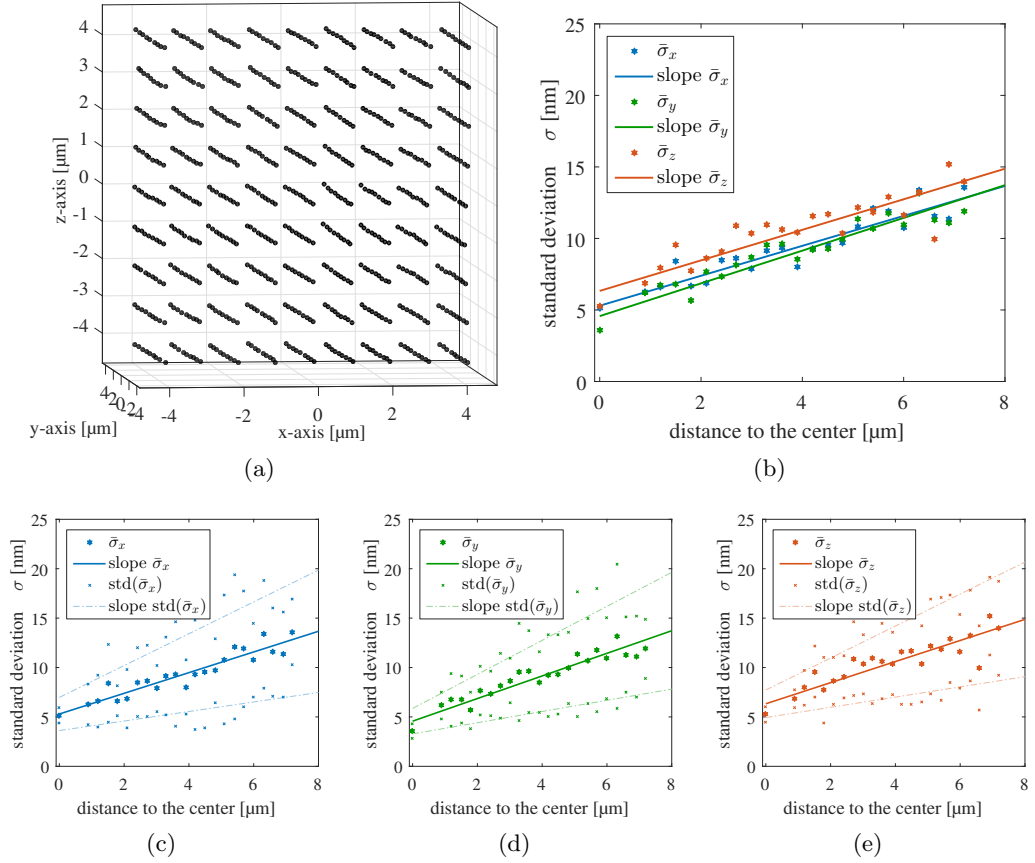


Figure 5.8: Experimental characterization of the Stereo 3D-SMS setup in the case of actual fluorescent dyes with a restricted photon number.

a) Mean values of the determined $\varnothing = 45$ nm bead positions at each grid point of a $8 \times 8 \times 8 \mu\text{m}^3$ cube ($\Delta_{x,y,z} = 1 \mu\text{m}$, black marks)

b) Standard deviation of the mean values averaged over 300 nm with respect to the distance from the center, separated for each spatial direction. The slopes are illustrated by lines.

c-e) Mean values of subfigure b) together with their respective standard deviations, separated plot for each coordinate.

5.6 Experimental quantification of the setup capability

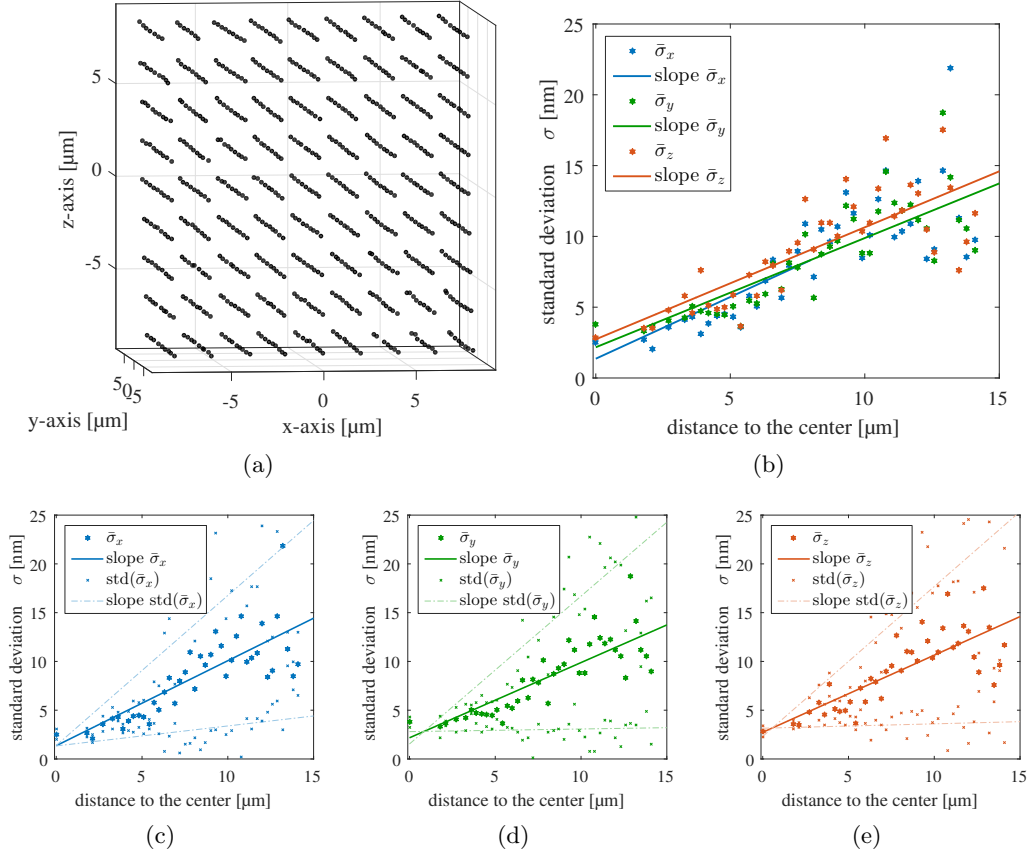


Figure 5.9: Capability of the setup in the case of bright emitter.

- a) Mean values of the determined $\varnothing = 200$ nm bead positions at each grid point of a $16 \times 16 \times 16 \mu\text{m}^3$ cube ($\Delta_{x,y,z} = 2 \mu\text{m}$, black marks)
- b) Standard deviation of the mean values averaged over 300 nm with respect to the distance from the center, separated for each spatial direction. The slopes are illustrated by lines.
- c-e) Mean values of subfigure b) together with their respective standard deviations, separated plot for each coordinate.

5.7 Particle tracking for viscosity measurement

The setup can be used to track moving particles within the focal volume. For the proof of concept fluorescent beads of 200 nm diameter are used, diffusing normally in the surrounding medium. Additional measurements are done with $\varnothing = 45$ nm beads. Following section 3.2.2 it is possible to determine the dynamic viscosity η by calculating the mean square displacement and with it the diffusion constant D of the particles.

Two different buffers are used: the normal base imaging buffer with mainly 10% (w/v) glucose dissolved in H_2O , described in section 3.4.3, and alternatively 30% (w/v) glucose dissolved in H_2O . For comparison of the results the viscosities of these solutions are also measured by a capillary viscometer (Lauda, Ubbelohde capillary). The thereby determined kinematic viscosity ν can be converted to the dynamic one by multiplication with the density ρ of the solution.

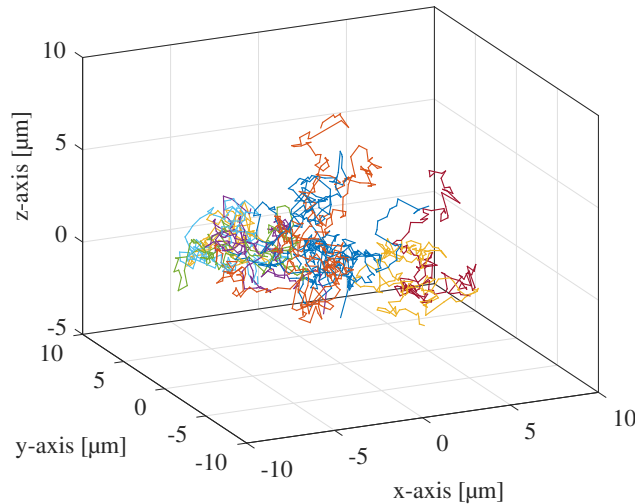


Figure 5.10: Exemplary tracks of five diffusing $\varnothing = 200$ nm beads in a 10% glucose solution.

Exemplary bead tracks are illustrated in figure 5.10. These five beads of 200 nm diameter are diffusing in 10% glucose solution, measured with a time constant of $\tau = 30$ ms. The detected photon numbers are in the range as in the case of the calibration measurements for the $\varnothing = 200$ nm beads.

The determined values MSD, D and η for the diffusion in the two different solutions are written in table 5.1, together with the results by the viscometer.

The viscosities measured by tracking η_{tracking} are within the given errors in ac-

5.7 Particle tracking for viscosity measurement

	10% glucose	30% glucose	
MSD	$(2.7 \pm 0.1) \cdot 10^{-13}$	$(1.8 \pm 0.5) \cdot 10^{-13}$	[m ²]
D	$(1.5 \pm 0.6) \cdot 10^{-12}$	$(1.0 \pm 0.3) \cdot 10^{-12}$	[m ² /s]
η_{tracking}	1.4 ± 0.6	2.2 ± 0.6	[mPa s]
$\nu_{\text{viscometer}}$	1.275 ± 0.002	1.959 ± 0.001	[mm ² /s]
ρ	1.05 ± 0.01	1.10 ± 0.01	[g/cm ³]
$\eta_{\text{viscometer}}$	1.34 ± 0.01	2.16 ± 0.02	[mPa s]

Table 5.1: Results for tracking $\varnothing = 200$ nm beads.

For both glucose solutions of different percentages, the dynamic viscosities η_{tracking} and $\eta_{\text{viscometer}}$ agree well within the fault tolerances. This keeps for both glucose solutions of different percentages.

cordance with the viscosities measured by the viscometer $\eta_{\text{viscometer}}$. The solution with 30% glucose is more viscous than the one with 10% glucose, as expected. The more viscous the solution is, the more restricted are the movements of embedded particles. This goes along with a dropping mean square displacement and a dropping diffusion constant.

These measurements verify the capability of the setup for tracking. This is not restricted to diffusing fluorescent beads but can in principle also be any other optically detectable particle within the detection volume.

The tracking was tested as well with smaller fluorescent beads of 45 nm diameter. They are much dimmer than the previous ones with mean photon numbers in the range of 3000 to 4500 photons per objective lens.

Specially in the case of the small beads with a dim fluorescent signal and with it the lower focal volume, the signal of beads attached to the cover glass disturb the data acquisition. To avoid this problem, the common focus point should be moved away from the surface of the cover glass. But in this experimental setup the four objective lenses can only be adjusted onto the common focus point by a test sample on the cover glass. Unfortunately, this needs to be done after each replacement of the sample holder. When moving up the common focus point into the medium this would introduce a focal shift for the bottom objective lens, corresponding to sections 3.2.1 and 5.3. In the case of the brighter signal, a major focal shift can be tolerated due to the extended focal length of the relatively low NA objective lens. Nevertheless, also for the 45 nm beads signal trajectories could be identified and the determined values for the diffusion are written in table 5.2.

The determined viscosity by the tracking is increased by a factor of 1.9 (10%

	10% glucose	30% glucose	
MSD	$(6.8 \pm 1.3) \cdot 10^{-13}$	$(4.9 \pm 2.2) \cdot 10^{-13}$	[m ²]
D	$(3.8 \pm 0.7) \cdot 10^{-12}$	$(2.7 \pm 1.2) \cdot 10^{-12}$	[m ² /s]
η_{tracking}	2.5 ± 0.5	3.5 ± 1.5	[mPa s]
$\eta_{\text{viscometer}}$	1.34 ± 0.01	2.16 ± 0.02	[mPa s]

Table 5.2: Results for tracking $\varnothing = 45$ nm beads.

The determined dynamic viscosities η_{tracking} and $\eta_{\text{viscometer}}$ match except of a factor of 1.9 (10% glucose solution) respectively 1.6 (30% glucose solution)

glucose solution) or 1.6 (30% glucose solution). Beside the diameter of the beads, all conditions in the different tracking experiments are the same.

However, the track of a single bead is mostly much shorter. That is because the fluorescent signal and with it the volume in which they can be reliably localized is lower. Additionally, the small beads diffuse faster due to the reduced Reynolds number. All this leads to a greater error of the mean square displacement, the diffusion coefficient and finally the viscosity η_{tracking} . Still, the error is not sufficient to satisfactorily explain the difference of the measured viscosities by the tracking and their reference values.

5.8 Measurement of different cell structures

The imaging of cellular structures with subdiffraction resolution is the main application for the SMS microscopy. In order to show the various capabilities of the presented setup, different cell components are measured exemplarily. These first results of samples based on switching fluorescent markers show the applicability of the stereo view concept for the SMS scheme.

The main demands for the sample are a great mean photon number and the optical separability of close by emitters. For all the cell experiments the dye Alexa Fluor 647 is used which fulfills the requirements to the marker to a high degree, as was pointed out in section 2.1.2. In order to improve the duty cycle even more, an embedding medium containing GLOX, MEA, PCA and PCD is taken, following section 3.4.3. The immunostaining of the investigated fixed HeLa or A6 cells is done with different primary and secondary antibodies.

The excitation and switching by the $\lambda = 639$ nm laser source can either be done from the bottom objective lens, from the top objective lenses or from all directions

at once. The power densities are $\sim 17 \text{ kW/cm}^2$ for the bottom objective lens and $\sim 4 \text{ kW/cm}^2$ for each of the top objective lenses.

For the illustration discrete emitter positions are deleted. The overview images show each detected position as a small sphere of a constant size with a color corresponding to its depth. For the intensity color-coded zoom in images a 3D gaussian with a FWHM of 20 nm is drawn into a grid followed by a smoothing.

5.8.1 Nuclear lamins - surrounding the cellular nucleus

The lamin protein is located at the inner membrane of the nucleus and can be used as a nuclear envelope marker. The immunostaining of the HeLa cells is done with the primary antibody rabbit anti-lamin B1 (ab16048, abcam plc). The secondary antibody is Alexa Fluor 647 goat anti-rabbit (A21245, Thermo Fisher). The applied paraformaldehyd (PFA) fixation keeps the 3D structure of the cell sample. Usually, the nucleus is the thickest part of an adherent cell. This sample is well suited to show the great extent of the detection volume.

A typical frame of the camera, cropped to the detection areas of the four objective lenses, is shown in figure 5.11. The emitter positions in the respective detection planes are localized by gaussian fits. A drift correction for each of the perspectives is applied and these final positions are marked in the image with blue asterisks. Ideally the same emitter can be found in all four detection planes. Due to the tilted orientations of the planes in 3D space with respect to each other, the 2D detection position in one plane corresponds to a line in each of the other planes. These lines are also illustrated in the exemplary detection frame for a single picked emitter. Each of the line colors correspond to one of the perspectives. The smallest distances of all lines of one frame are calculated in accordance to section 4.2.3 which reduces the possible related detection patterns. The fine tuning of the transformation parameters was done by 500 bright emitters. The details for the calculation of the 3D emitter positions with twofold iteration using the adjusted transformation parameters can be found at section 4.2.

The result of the lamin measurement is presented in figure 5.12. The image shows the depth color-coded overview of the determined marker positions. The three-dimensional structure of the nucleus is clearly visible. The expansion in the z -direction is about $6 \mu\text{m}$, indicated by the range of the color bar. The x/y expansion is more than $14 \mu\text{m}$. In the surrounding cytoplasm and inside the nucleus almost no markers are localized. The latter is illustrated by the open cut at the front side.

Cross-sections with different orientations show the subdiffraction resolution in figure 5.13. At various positions perpendicular to the nuclear envelope show a feature size of about 50 nm (FWHM). Also, these cross-sections emphasizes the hollow structure and the absence of imaging artefact such as ghost images.

The depth of the cross-sections is 40 nm and the width of the applied line profiles is 100 nm. The mean numbers of detected photons are $N_1 \approx 4560$ for the bottom objective lens and $N_{2/3/4} \approx 4380$ for each of the upper objective lenses. The excitation and off-switching is done through the bottom objective lens. The possible on-switching induced by UV-light was not necessary due to the sufficient high spontaneous on-switching. This holds true also for the following cell samples. The measurement is made with 40,000 frames of 30 ms exposure time.

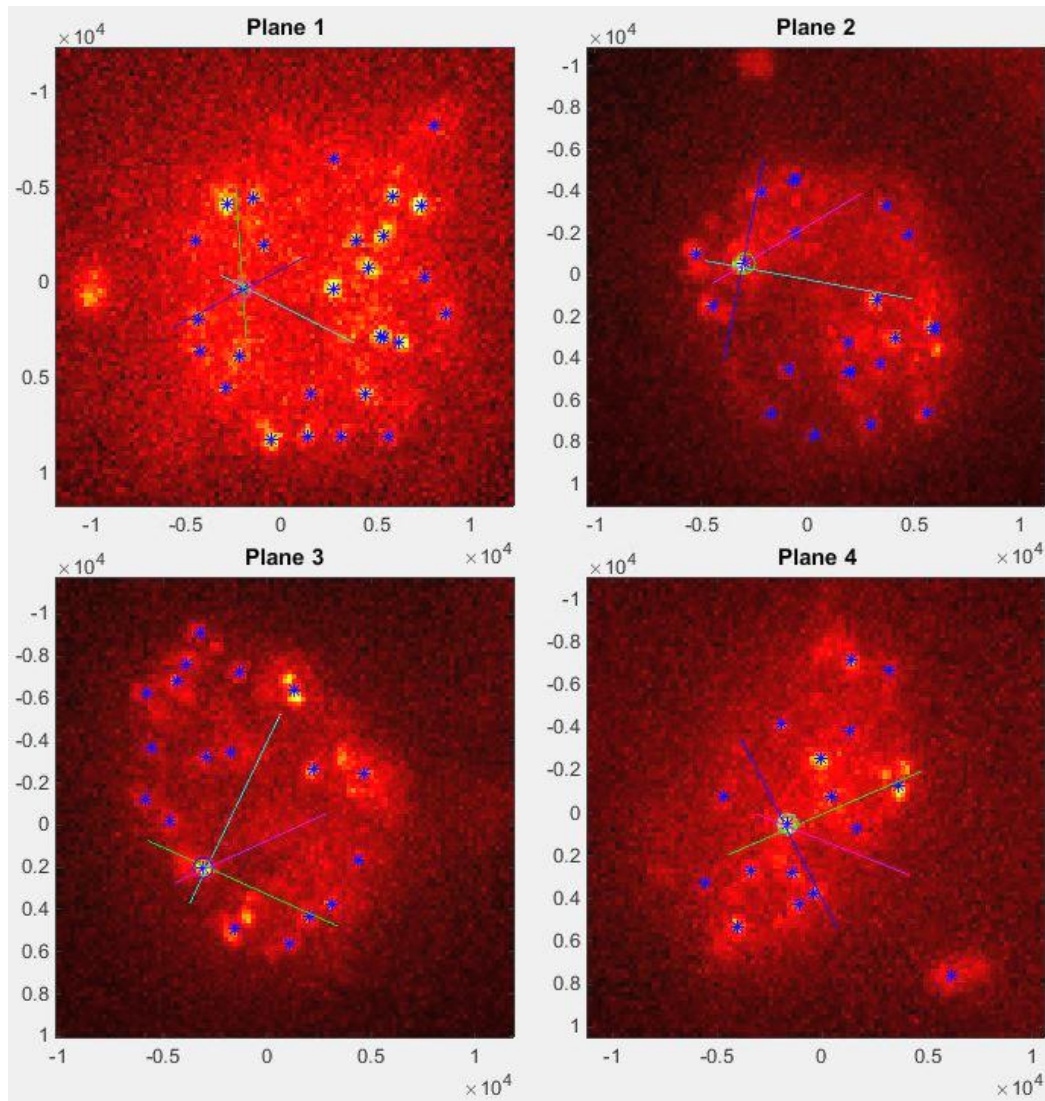


Figure 5.11: Exemplary detection frame of the ellipsoid-like nuclear envelope.

It is one of 40,000 frames and shows the fluorescence of several on-switched fluorophores from the four different objective lens perspectives. The centroid of the detection pattern i.e. the emitters position is determined by a gaussian fit and highlighted with blue asterisks. The exemplary lines of different colors, one for each orientation, are used to fine-tune the transformation parameters.

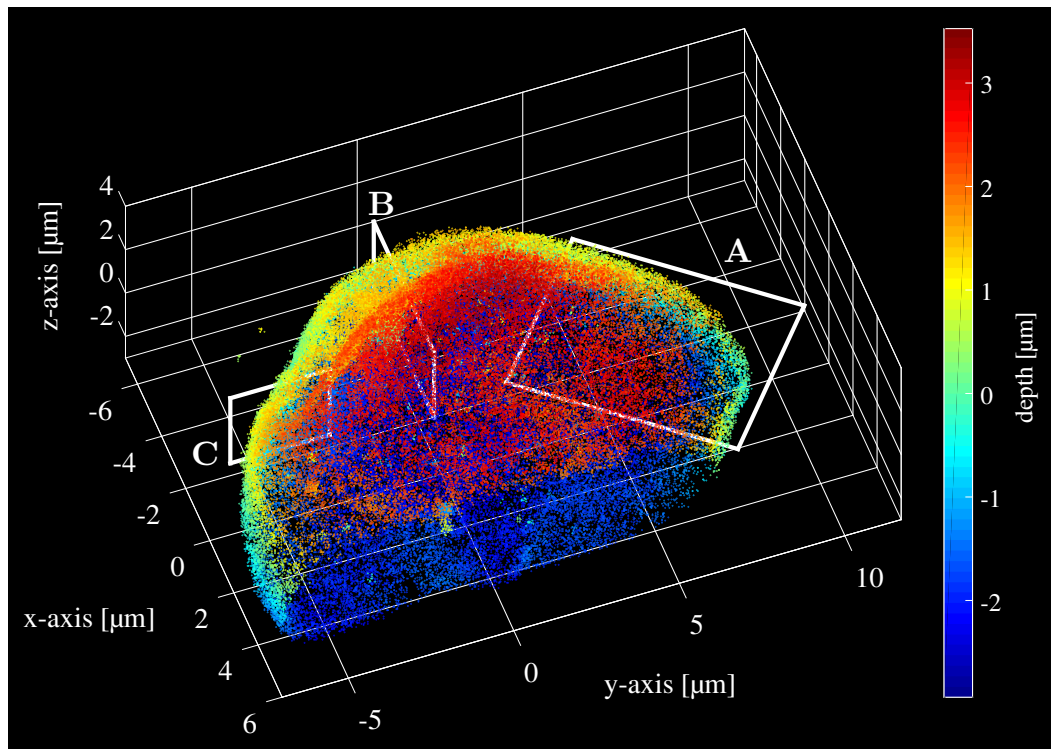


Figure 5.12: Nuclear membrane, fluorescent labeled by anti-Lamin B1 in a HeLa cell.

The depth color coded positions of the fluorescent markers gives a good impression of the extension of the nuclear envelope. The open cut at the front side of the membrane illustrates the hollow structure. The anti-Lamin attaches very specifically to the surrounding membrane. The cross-sections A (x/y), B (x/z) and C (y/z) are shown in detail in figure 5.13.

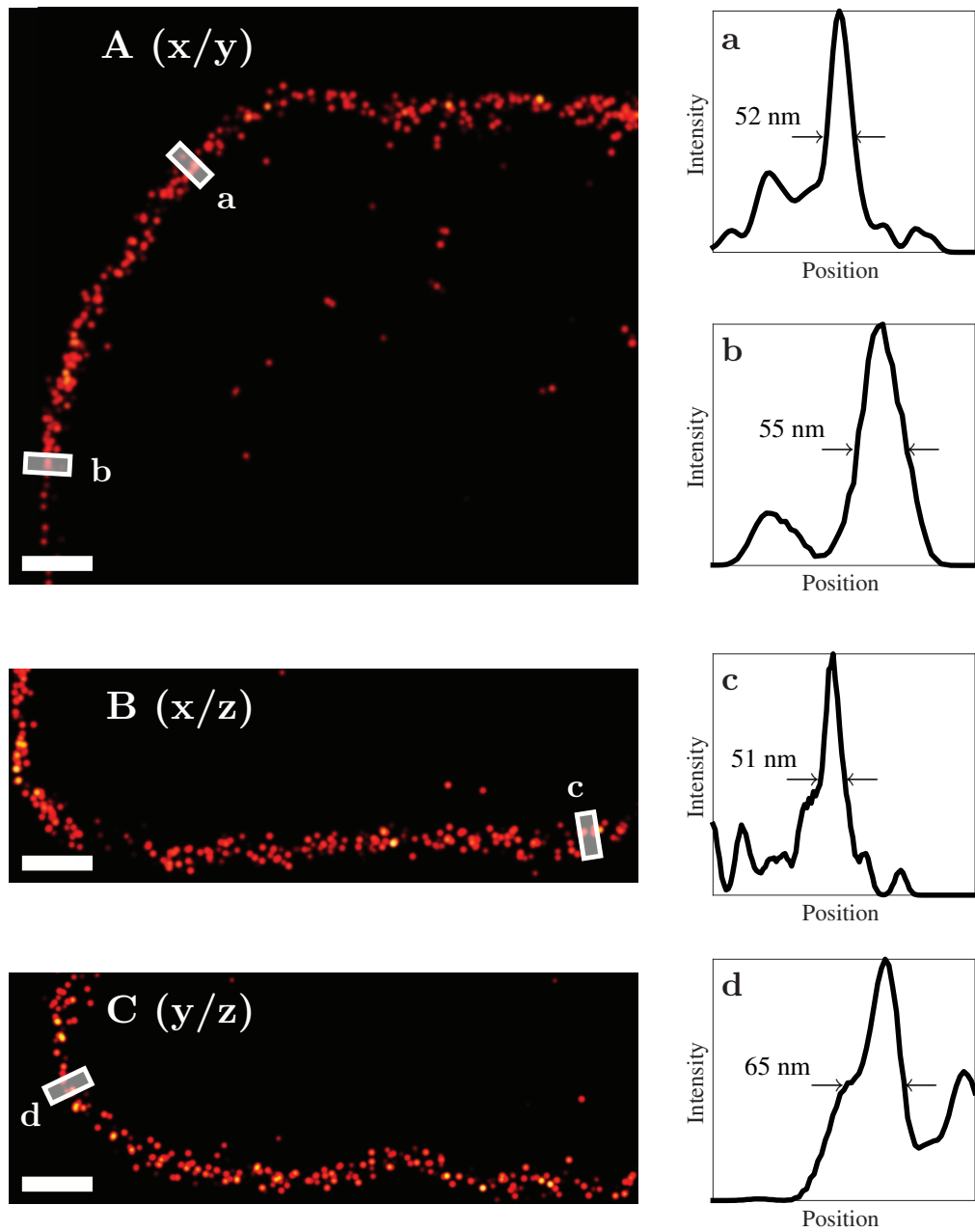


Figure 5.13: Cross-sections in different cartesian planes of the nuclear laminin at figure 5.12 and profiles over the white boxes.

Regardless of the orientation of the cross-sections, feature sizes of 50–60 nm can be shown. Moreover they emphasize the hollow structure of the fluorescent marked nuclear envelope. The scale bars indicate 1 μm .

5.8.2 Vimentin filaments - part of the cytoskeleton

The second example of cellular structures are vimentin filaments. These type III intermediate filament proteins are part of the cytoskeleton, along with the actin filaments and the microtubules [56]. Vimentin has mainly a structural role by giving mechanical strength to the cell and the surrounding tissue. The staining of the PFA fixed HeLa cells is done with the primary antibody mouse anti-vimentin (V6389, Sigma-Aldrich) and the secondary antibody Alexa Fluor 647 goat anti-mouse (A21236, Thermo Fisher). The measurement is made with 40,000 frames of 30 ms exposure time.

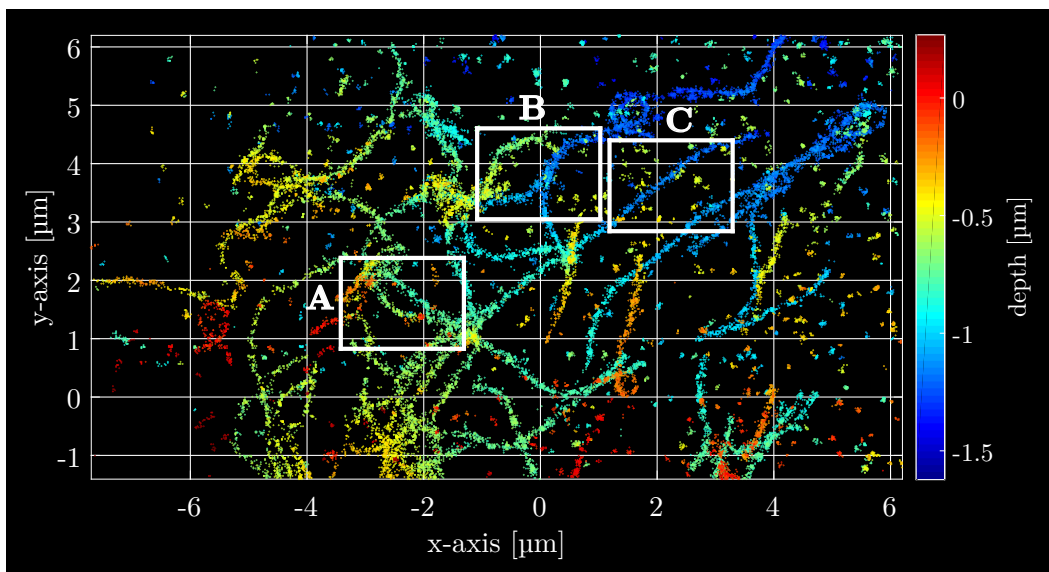


Figure 5.14: Vimentin filaments of a HeLa cell

Despite the reduced thickness of about $1.5\ \mu\text{m}$ crossing filaments at different levels can be separated. This is visualized by the depth color code. Detailed areas are indicated by A/B/C and shown in figure 5.15.

The calculated three-dimensional emitter positions of the vimentin measurement are presented in figure 5.14. The lateral x/y expansion is in the range of $\pm 6\ \mu\text{m}$ while the depth is about $1.5\ \mu\text{m}$. This low thickness is expected since the imaging area is located in the flat peripheral, sketched in figure 2.9. The depth color-code shows vimentin filaments crossing each other in different layers.

The subareas A/B/C are illustrated in figure 5.15. Profiles over single filaments show a feature size of $45\text{--}50\ \text{nm}$ (FWHM). The separation of structures closer than the diffraction limit of $\lambda/2$ is shown in subarea B. Two filaments about $60\ \text{nm}$ apart

5.8 Measurement of different cell structures

can clearly be separated shown by the line profile.

At the subareas the whole depth is accumulated and the width of the applied line profiles is 100 nm. The mean numbers of detected photons are $N_1 \approx 6980$ for the bottom objective lens and $N_{2/3/4} \approx 5640$ for each of the upper objective lenses. The excitation and off-switching is done through the bottom objective lens.

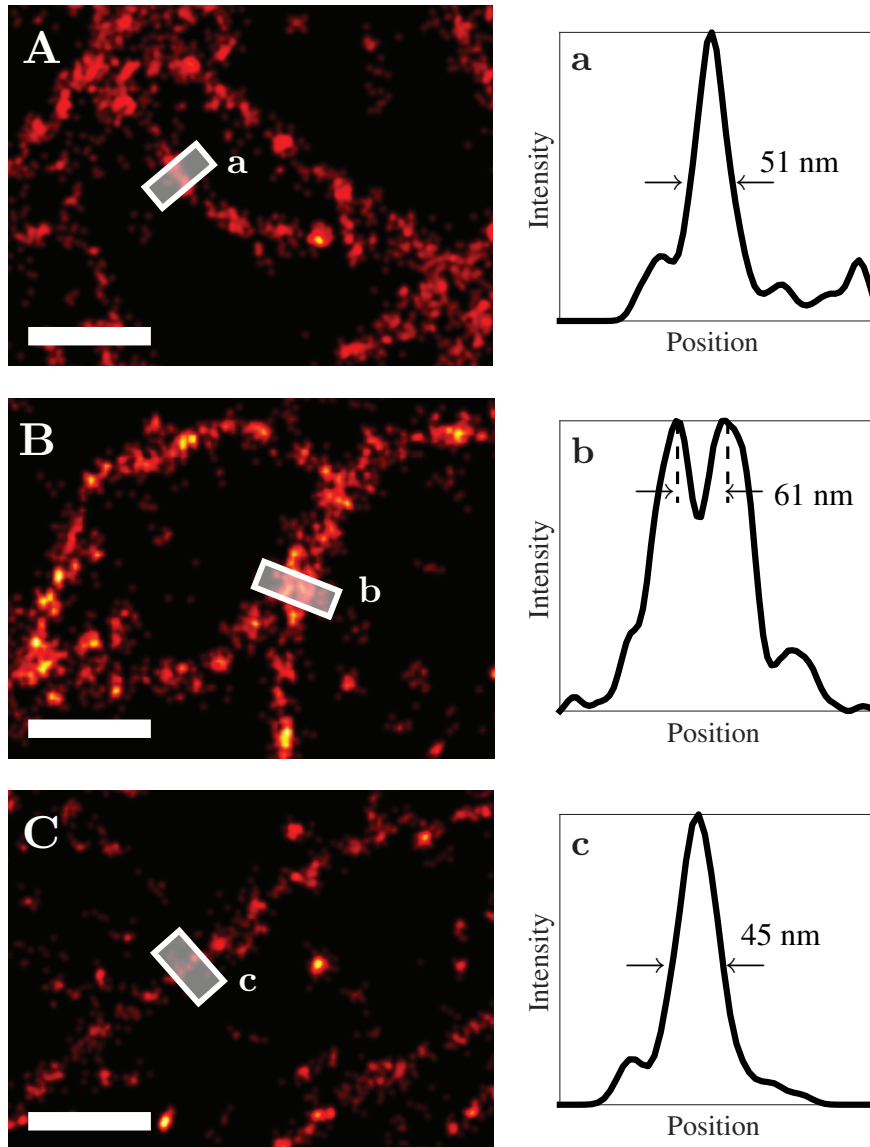


Figure 5.15: Detailed subareas of the vimentin filament measurement and profiles over the white boxes.

The filaments at the subareas A and C can be localized down to a precision of at least 45 nm. To convincingly show resolution enhancement close by structures need to be separable. This can be done at subarea B. Filaments with distance of about 60 nm can clearly be resolved. The scale bars indicate 500 nm.

5.8.3 Mitochondrion organelle - power plant of the cell

Mitochondria are organelles inside the cell and among others responsible for supplying cellular energy. They have their own independent genome and feature a double membrane. In order to exchange molecules with the surrounding, transmembrane transport proteins are needed. The subunit of this translocase protein complex, which is located in the outer membrane, is called outer membrane translocase (Tom) import receptor. One of these chaperone proteins is the Tom20. For imaging in the 3D-SMS setup PFA fixed HeLa cells are immunostained with the primary antibody mouse anti-Tom20 (sc-17764, Santa Cruz Biotechnology) and the secondary antibody Alexa Fluor 647 goat anti-mouse (A21236, Thermo Fisher). The measurements are done with 40,000 frames of 30 ms exposure time.

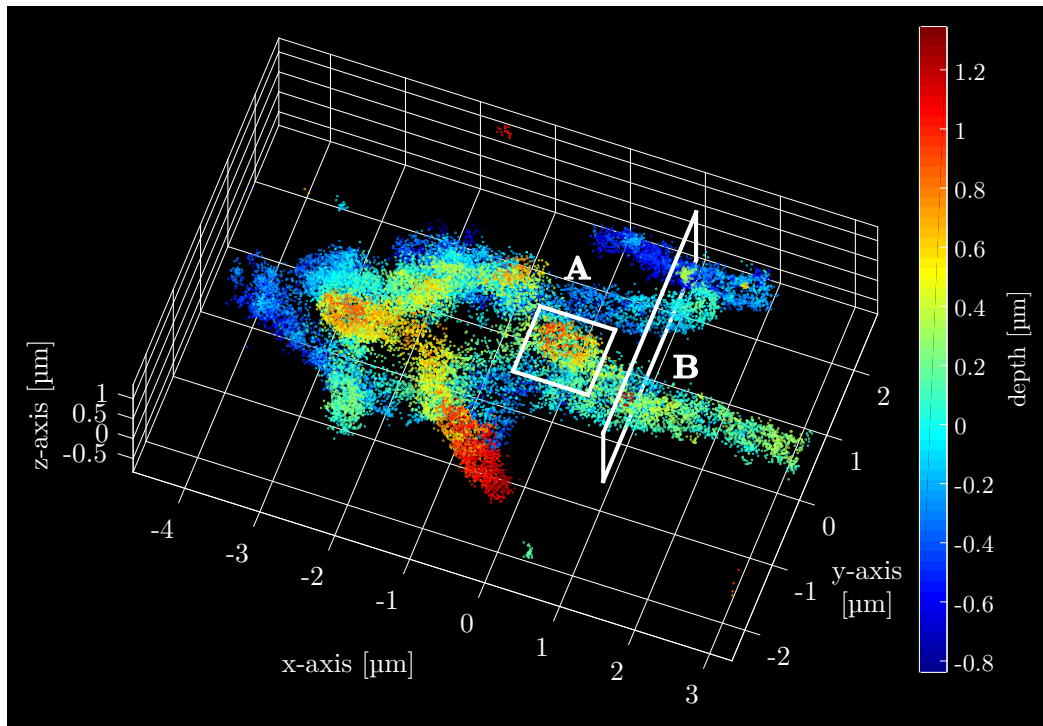


Figure 5.16: Network of mitochondrion organelles in HeLa cells.

The measurement of fluorescently labeled Tom20 in the outer membrane of mitochondria shows their tube-like structure. They have varying radii and are oriented in different directions. In order to visualize the hollow structure, cross-sections in the x/y (A) and y/z (B) planes are shown in figure 5.17.

The determined 3D emitter positions are illustrated in figure 5.16. The network

structure of the mitochondria is clearly visible. Most of the ball and tube like formed organelles are oriented horizontally whereby some are also oriented almost perpendicular to the cover glass. This can be seen by the depth color-code.

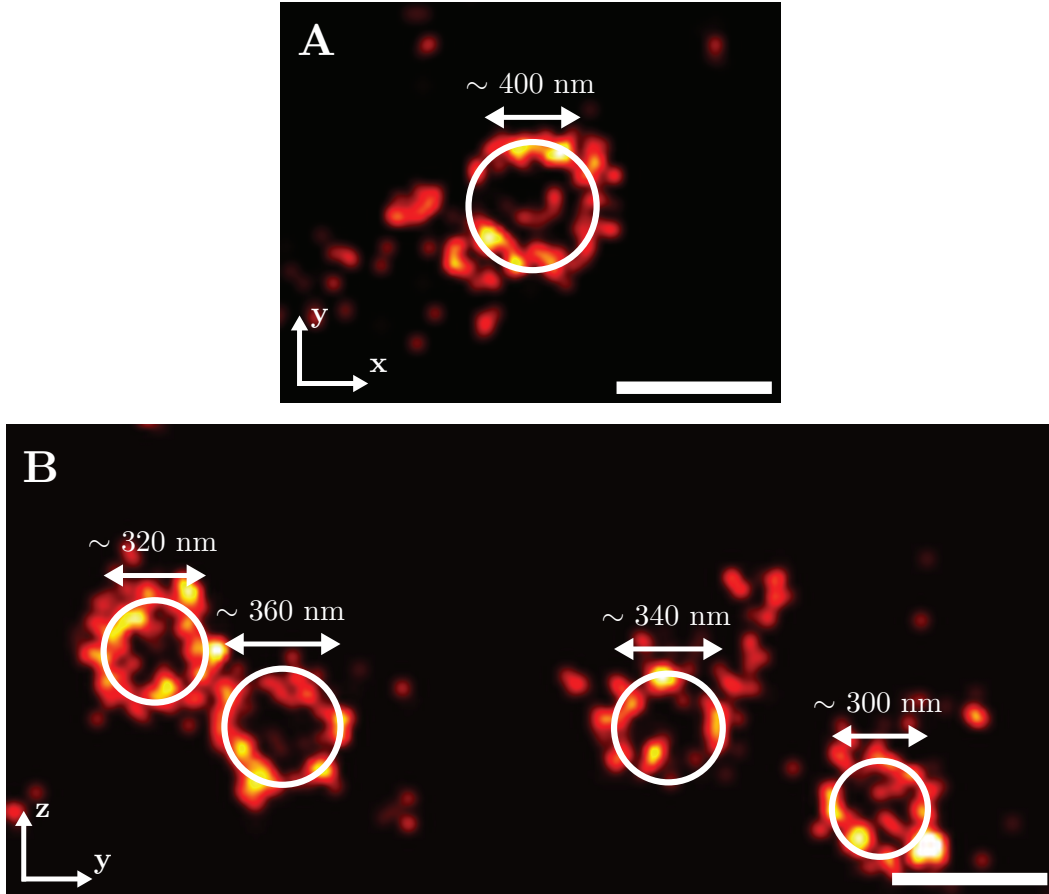


Figure 5.17: Cross-sections of hollow mitochondria organelles.
Their diameter is in the range of 300 to 400 nm.

Cross sections in the y/z as well as in the x/y plane show the hollow structure of the organelles in figure 5.17. This suggests that the fluorescent marker specifically coupled to the outer membrane of the mitochondria as intended. The measured diameter of these depicted mitochondria are 300 to 400 nm, both in the horizontal and the vertical. This is in good accordance to previous publications [57]. The scale bars indicate 500 nm.

The cross-sections are accumulated over a depth of 200 nm. The mean numbers of detected photons are $N_1 \approx 4560$ for the bottom objective lens and $N_{2/3/4} \approx 3900$ for each of the upper objective lenses. The excitation and switching is done by all

of the top objective lenses.

5.8.4 Protein gp210 in the nuclear pore complex - gateway of the nucleus

For the last example the gp210 proteins in the nuclear pore complex of A6 cells (*Xenopus laevis*, South African clawed toad kidney) are fluorescently marked. These proteins are known to form a 164 ± 7 nm diameter ring in the circular nuclear pore complex [58].

The preparation of this PFA fixed cell sample is done by immunostaining with a primary antibody against *Xenopus* gp210 [59, 60]. The secondary anti-mouse antibody again attaches Alexa Fluor 647 to the target. The calculated emitter positions are shown in the following figure 5.18. The measurement is done with 40,000 frames of 30 ms exposure time.

The nucleus of the adherent and PFA fixed A6 cells is rather flat in comparison to the one of HeLa cells, figure 5.12. Nevertheless, the expansion in the z direction of $>2.5 \mu\text{m}$ is greater than a high NA objective lens can measure without scanning.

The ring-like arrangement of the gp210 proteins can be seen at various locations around the nucleus. The sub-images in figure 5.19 show the ring structure at different orientations, both in the vertical and in the horizontal directions. The regions of interest (ROIs) A/B/C/D are located at the upper side and E/F/G/H are located at the bottom side. Both are visualized in the horizontal x/y direction. The ROIs I/J/K/L/M are located at the side with one axis to the z -direction. The dimensions of the ring structures, indicated by the 100 nm scale bar, are in accordance with previous results [58, 59] of about 160 nm. Incomplete ring-like structures may be due to incomplete labelling. Additionally, some fluorophores may have failed to contribute to the final image, e.g. because they bleached early or because of unsuccessful localization. Smaller diameters or elliptical shapes appear if the nuclear pore complex is tilted out of the respective plane.

The marker detection positions in the subareas are accumulated over the depth of the membrane. In this measurement the mean numbers of detected photons are $N_1 \approx 5080$ for the bottom objective lens and $N_{2/3/4} \approx 3640$ for each of the upper objective lenses. The excitation and off-switching is done through the bottom objective lens.

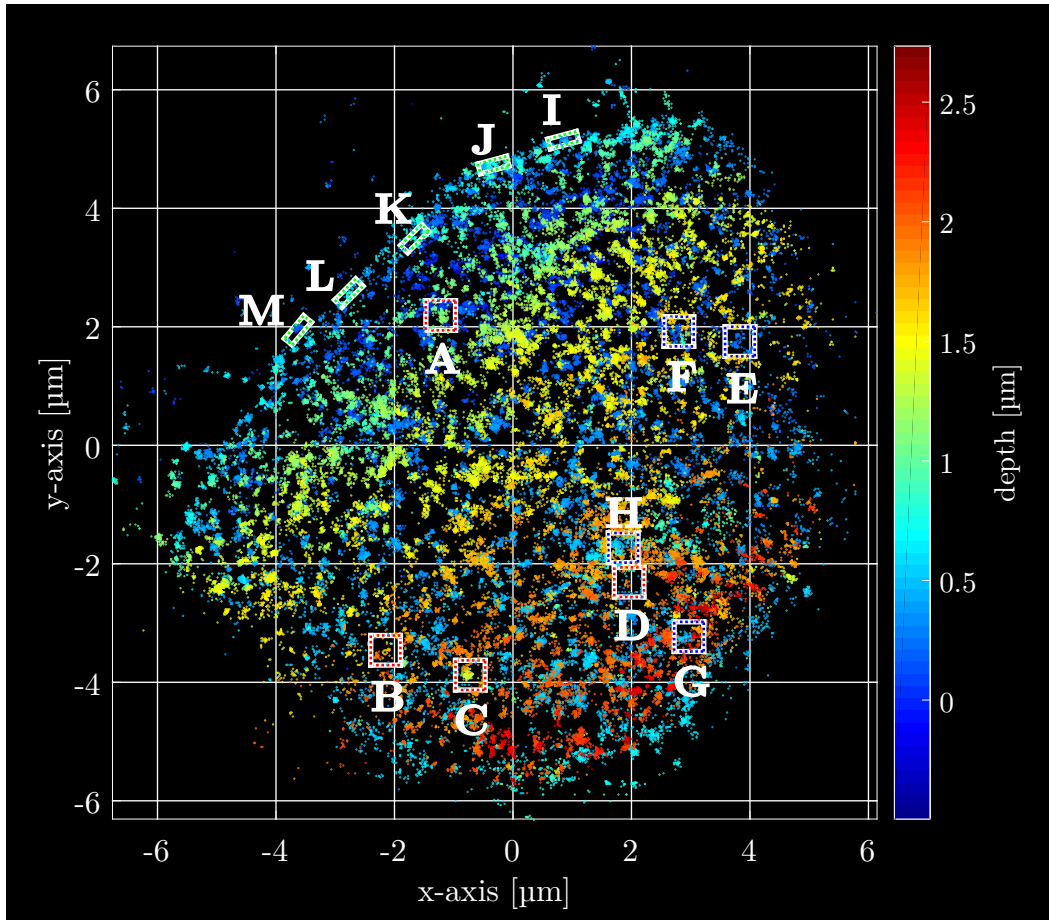


Figure 5.18: Nuclear pore complexes spread over the entire nuclear envelope of an A6 cell.

The protein gp210 is marked by a specific antibody [59]. The depth of the emitter positions is color coded. The nuclei of A6 cells are typically much less vertically extended than the one of HeLa cells, for example in figure 5.12. Several zooms into single nuclear pore complexes are indicated by rectangles and illustrated in figure 5.19.

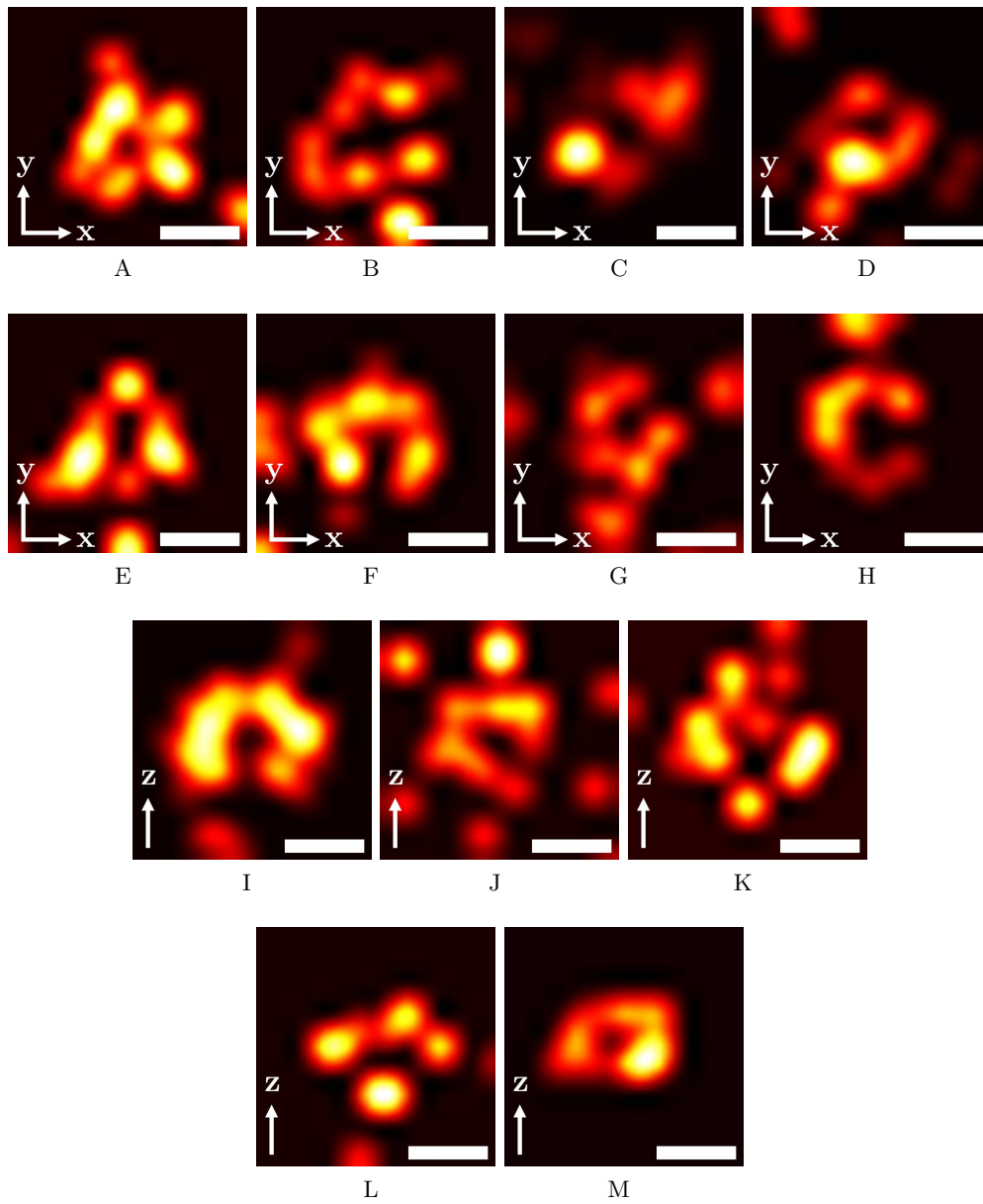


Figure 5.19: Annular structure of the gp210 protein within the nuclear pore complex.

The nuclear pores can be visualized in the x/y plane (A-D top side and E-H bottom side of the nucleus) as well as in the vertical direction (I-M). The scale bars indicate 100 nm.

Chapter 6

Discussion and further developments

In this work, the Stereo 3D-SMS microscope is presented which, by using several objective lenses, transfers the intrinsically two-dimensional SMS concept of super-resolution microscopy into the third dimension. For this purpose, the corresponding mathematical description is derived and the theoretical capabilities of the concept are calculated. Furthermore, a technical setup is designed and built that fulfills all requirements regarding optics, mechanics, stability, usability and so on. This fully customized setup requires its own computer routines for control and automated data acquisition. In addition, special algorithms for the calculation of the 3D emitter positions from the 2D detection patterns are required. The latter even with the restriction that the exact correlation parameters of the objective lenses and the sample within this development setup change from one measurement to the other. Following the solution of all these prerequisites, the setup is experimentally evaluated and first measurements are performed.

The evaluation of the quantification measurements reveals an almost isotropic precision of $\sigma_{x/y/z} = 5 - 15 \text{ nm}$ in a spherical volume of $\varnothing = 14 \mu\text{m}$. The sample brightness used is comparable to the photon numbers detected by the fluorophores in cell measurements. Therefore, the results obtained are certainly transferable to the imaging of biological samples. Due to the deliberately implemented spherical aberration to the detection PSF, the intensity maximum remains in the center of the detection pattern over a large axial range. Thus, even at larger distances from the focal plane, the center of gravity can be determined by applying a Gaussian fit. As a result, the volume in which a high localization precision is achieved is significantly larger in the practical implementation than theoretically expected. This quantification was performed for detected photon numbers, which can currently be obtained under optimized imaging conditions for biological samples. In order to estimate the performance limits of the microscope, an approximately three times

brighter sample was used. As expected, the localization precision improved by a factor of about 2 ($\sqrt{3} = 1.7$), leading to an increase in the diameter of the detection volume from 14 μm to 26 μm . Thus, no inherent limitations were found (for this range) and it is expected that the system will also be able to provide these results for biological samples, provided that brighter fluorophores will be available in the future.

The high resolution as well as the large detection volume can also be confirmed for biological application by imaging four different structures within cells. In the case of nuclear lamin, the total thickness of the nucleus of about 6 μm is measured at once without the need for axial scanning. In addition, the lamin and vimentin measurements reveal the nearly isotropic resolution of 50 – 60 nm in all spatial directions. For comparison: The published maximum focal depth in SMS microscopy using high NA objective lenses is $\sim 1.2 \mu\text{m}$ [25]. Therefore, at least five scan layers would have been required in this case to completely image the whole volume of the nucleus.

In a further biological sample, the annular structures of the nuclear pore complexes with radii below the diffraction limit were resolved, independent of their orientation in space. Due to the limited availability of the gp210 antibody, the measurements of the nuclear pores could unfortunately not be further optimized. Beyond that, also the interior of completely closed structures such as tube-like mitochondria could be imaged. A cross-section of the fluorescence-labelled folded double membrane shows the labeled ring structure.

In addition to pure imaging, the tracking of normally diffusing microspheres demonstrates another possible field of application for the Stereo 3D-SMS concept. By estimating the mean square displacement (correlated with the diffusion) of $\varnothing = 200 \text{ nm}$ microspheres, the kinetic viscosity of glucose solutions of different concentrations can be fully verified. For $\varnothing = 45 \text{ nm}$ microspheres, the determined kinematic viscosities deviate by a factor of 1.6 to 1.9 from viscometer measurements. This underestimation is probably due to the comparatively small size of the microspheres. For instance, the Stokes-Einstein relation (eq. 3.13) used to calculate the viscosity from the diffusion is an approximation for high Reynolds numbers. Because of the small size of the $\varnothing = 45 \text{ nm}$ microspheres, this approximation is apparently no longer valid. In addition, interactions between the microspheres and the glucose strands as well as the surface of the cover glass may occur.

All in all, both the cell measurements and the tracking experiments confirm the expected properties of the setup. Since the proof of concept for Stereo 3D-SMS mi-

crosscopy has been provided, the technique can now be developed further in various ways.

The existing setup is designed for maximum flexibility. However, in order to increase its stiffness and thus its reproducibility, after the final selection of the objective lenses and their relative angles with respect to each other, a design with fewer degrees of freedom should be considered. A possible variant is outlined in the following:

A commercially available inverted microscope body serves as the stable base and provides the lower, upright objective lens and the corresponding imaging optics. The three other objective lenses are mounted into an attachable top unit. The exact positioning of this unit is preferably motorized in conjunction with a pre-defined end position. This would allow to remove and replace the sample in a reproducible manner. The currently available five degrees of freedom for each of the upper lenses (two rotations, three shifts) can be reduced to one (shift of the focus along the respective optical axis). Furthermore, the beam paths can be significantly shortened by direct focusing with the tube lenses onto the camera. The fields of view of the upper lenses can either be imaged onto the same detector or individually on a separate chip each. With this mechanically significantly more stable design, it would be possible to concentrate much more on other experimental aspects such as sample preparation and evaluation.

Currently, the design is limited to the red spectral range and therefore the choice of dyes is limited. However, by adapting the laser sources and the filters used, it is also possible to operate in other spectral ranges or with multiple colors. For multicolor imaging, for instance, specific notch filters would be required instead of a single dichroic long- or short-pass mirror.

One problem in standard applications was the occurrence of focal shifts when focusing deeper into refraction mismatched samples. In order to compensate for this effect, a routine is required that could calculate a corrected z -position for the lower lens as a function of the desired common focus position, the cover glass position and the expected focus offset (measured as in section 5.3).

In addition, the configuration of the detection volume can also be modified. In the current setup, the centers of the fields of view of all objective lenses are aligned to one common point. By shifting the focal planes of all objective lenses away from this point, the localization precision in the center decreases because the focus planes no longer intersect there. In return, however, the precision in the outer regions as well as the overall size of the detection volume are increased.

So far the orientation of the fluorophores has not been considered in the data evaluation. In case a fluorophore does not emit isotropically over the time scale of a single image, these intensity fluctuations might be detected by the different objective lenses. This would allow to draw conclusions on the orientation of fluorophore's dipole moment and hence on order parameters within the structure under investigation. However, this would require precise knowledge of the relative detection efficiencies of all four channels. Like the previous points, this would also demand a long-term stable setup without variations in the detection, the relative detection angles, or the like.

The basic considerations for the setup were based on a perfect tetrahedron and a corresponding maximum aperture angle of 109.5° for all four objective lenses. Thus, the ideal design would have a completely isotropic resolution and due to the larger aperture angle of the objective lenses compared to the one presented here, even more photons could be detected, which in turn would improve the localization precision. Due to mechanical constraints such as the size of the lens housing, however, limitations had to be accepted. In order to get as close as possible to the optimum resolution, the aim must therefore be to relay the fluorescence away from the crowded central area. This would be conceivable by using 1 : 1 lenses in a tetrahedron arrangement in whose center the sample is located, see figure 6.1. It is mandatory to use the magnification of 1 in order to fulfill both the Herschel and the sine conditions [39]. Otherwise, strong aberrations would be induced. The fluorescent light of the emitter in the center would be transferred to the outside via these lenses, where the focal positions of the objective lenses can be positioned without mechanical restrictions. A compromise that would have to be made is the reduction of the depth of field when using higher NA lenses. However, this would also increase the solid angle to $\Omega = 2.66$ sr as compared to 1.26 sr (NA 0.8, water) respectively 2.13 sr (NA 0.75, air), which in turn increases the resolution of the overall system.

In addition to the aforementioned technical possibilities, optimizations of the sample and associated components as well as the calculation process are also possible.

The classical SMS sample consists of an object placed on a cover glass and covered with a few microliters of buffer solution. To shield it from the environmental air, the cover glass is sealed airtight on a microscope slide. The composition of the buffer, as listed in section 3.4.3, is optimized for these controlled conditions and often crucial for the switching behavior of the fluorophores. In the case of the cur-

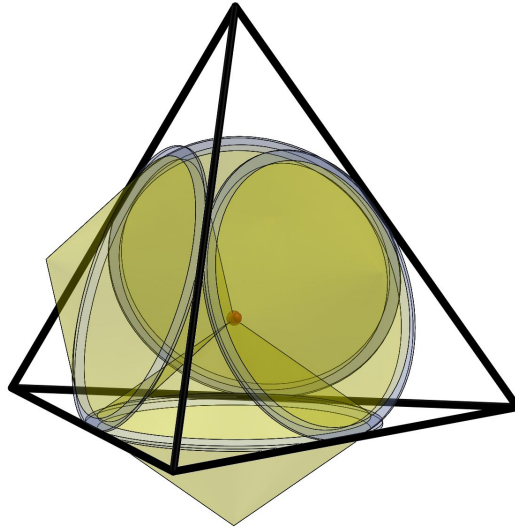


Figure 6.1: Transfer of the common focus point out of the sample by intermediate optical lenses. Their image can further be detected by high NA objective lenses. The housing of the objective lenses would be too large to get them close enough to the original center. Essential is to fulfill the Herschel and the sine conditions in order to avoid aberrations.

rent design of the Stereo 3D-SMS setup, however, the volume of the buffer medium is significantly larger and it is not isolated from the environment. As a result, in particular the buffer and the sample are no longer isolated from the surrounding oxygen and the switching behavior degrades. For instance, pH value stabilizers could be used to adjust the buffer. However, they usually contain highly toxic components which cannot be used due to the needed quantities and the lack of isolation from the environment. Therefore, other adaptations of the buffer must be found in future research, which work under the existing open conditions. In addition, there are also technical possibilities such as the suppression of the ambient oxygen with nitrogen or the design of a shielding cover. For both, however, changes to the setup design are necessary.

As a further component, the dye Alexa Fluor 647 used for the proof of concept has very good properties with regard to duty cycle and brightness. Therefore it is widely used in SMS microscopy. However, when used in the Stereo 3D-SMS setup, various problems occur. One is the described strong dependence on the buffer properties and the isolation from the ambient oxygen. Another is the adjustment of the signal density. Due to the lower NA and the higher focal depth of the objective lenses used, the size of the diffraction-limited volume is much larger than

with high NA objective lenses. In addition, there are four instead of one optical axis on which the signals of different fluorophores should not overlap (figure 2.6). In order to achieve a sufficiently low signal density, the sample must be bleached at the moment in the case of narrow structures before starting the measurement. Instead of using a dye that is initially in the bright state and must be switched off, a solution could be to use a dye that is initially in the dark state and can then be switched on precisely. Currently, these dyes such as the caged ones are too dark for the Stereo 3D-SMS method and thus deliver a very low signal-to-noise ratio. But future initial dark fluorophores may be much brighter and more independent of the exact environmental properties.

For the sample itself, the equivalence of all spatial directions allows a completely different preparation. Instead of the mostly preferred flat samples in the x/y plane, cell cultivation could also be performed in a 3D matrix. In this way, the natural environment as in the original tissue could possibly be better simulated. However, care must be taken not to implement strong refractive index differences.

Another main aspect of this setup is, in addition to the sample properties, the calculation of the 3D emitter position. So far the localization is performed as an intermediate step in the two-dimensional data analysis, like the classical SMS variant. The transition to the third dimension is done by setting up and solving a system of linear equations. Ideally, the 2D step should be made obsolete. One possibility is to generate a three-dimensional cloud for the probability of presence, supported by the detection arrays. This would make it possible to locate the emitter position directly in 3D space. Another reciprocal option would be the stepwise approximation to the spatial emitter position, whose calculated transformation into the image planes fits best to the detected patterns.

In the current Stereo 3D-SMS system, it is always necessary to calculate the correlation parameters of the objective lenses by automatically scanning the data for bright and single emitters near the central region. These emitters correlate to a high probability over all detection planes. In addition, if several emitters are detected simultaneously, they must be assigned across the detection planes. By the combination with the stochastic SOFI correlation concept, however, associated recognition patterns could be much better selected. This would allow both the determination of the desired correlation parameters and the assignment of multiple emitters.

Summarizing, the presented Stereo 3D-SMS microscope transfers the basic principle of switching fluorophores and localizing their centroid in order to gain super resolution from intrinsically 2D to the third dimension. Now that the success-

ful proof of concept has been completed, there are many possibilities for further development and creative use of this method for all possible areas of application.

List of abbreviations

2D	two-dimensional
3D	three-dimensional
CCD	charge-coupled device
COT	cyclooctatetraene
dSTORM	direct stochastic optical reconstruction microscopy
EMCCD	Electron Multiplying CCD
fPALM	fluorescence photo-activated localization microscopy
GLOX	glucose oxidase and catalase
FWHM	full width at half maximum
GSDIM	ground state depletion microscopy followed by individual molecule return
IC	internal conversation
iPALM	interferometric PALM
ISC	intersystem crossing
MEA	mercaptoethylamine
MSD	mean square displacement
NA	numerical aperture
PALM	photo-activated localization microscopy
PALMIRA	photo-activation localization microscopy with independently running acquisition

PCA	protocatechuic acid
PCD	protocatechuic dioxygenase
PFA	paraformaldehyd
PSF	point spread function
RESOLFT	reversible saturable/switchable optically linear fluorescence transition
ROIs	regions of interest
SLE	system of linear equations
SLM	spatial light modulator
SMS	Single Marker Switching
SOFI	super-resolution optical fluctuation imaging
SPEM	saturated pattern excitation microscopy
SSIM	saturated structured illumination microscopy
STED	stimulated emission depletion
STORM	stochastic optical reconstruction microscopy
UV	ultraviolet
W-4PiSMSN	whole-cell 4Pi single-molecule switching nanoscopy

List of Figures

2.1	Perrin-Jablonski diagram and spectra of Alexa Fluor 647	8
2.2	Histogram of the photon distribution	10
2.3	Intensity distribution of the emission from a dipole	13
2.4	Blurred imaging of a point source	15
2.5	Intensity profile of the PSF	16
2.6	Basic concept of SMS microscopy	18
2.7	Principles of unambiguous localization in the axial direction	21
2.8	Basic principle of a 4Pi-setup	22
2.9	PSF comparison for two objective lenses: NA 1.4 and NA 0.8	24
3.1	Basic concept of stereo view	26
3.2	Shifting of the focus position when moving the objective	31
3.3	Theoretical focus shift for oil/water optical transition	32
3.4	Orientation of the objectives in a tetrahedron like shape	34
3.5	Mounting of the objectives, top view	36
3.6	Mounting of the objective lenses, bottom view	37
3.7	Cross section view and illustration of the sample holder	38
3.8	Filter combination together with the normalized absorption and emission of the dye	39
3.9	Excitation and detection beam paths	41
3.10	User interface for control of sample and bottom objective lens	43
3.11	User interface for continuous measurements	44
3.12	User interface for control of sample and bottom objective lens	44
5.1	Comparison of the theoretical and experimental PSF	56
5.2	Comparison of borosilicate glass and CYTOP cover glass	57
5.3	System stability on a short time scale	58
5.4	System stability on a long time scale	59
5.5	Measured focal shift of the bottom objective lens	60
5.6	EMCCD camera conversion factor	61

5.7	Simulation of the setup capabilities	62
5.8	Experimental characterization of the Stereo 3D-SMS setup	66
5.9	Capability of the setup with bright emitter	67
5.10	Exemplary tracks of $\varnothing = 200$ nm beads	68
5.11	Exemplary detection frame	73
5.12	Nuclear membrane, fluorescent labeled by anti-Limin B1	74
5.13	Cross-sections in different cartesian planes of the nuclear lamin	75
5.14	Vimentin filaments of a cell	76
5.15	Detailed subareas of the vimentin filament measurement	78
5.16	Network of mitochondrion organelles	79
5.17	Cross-sections of hollow mitochondria organelles	80
5.18	Nuclear pore complexes spread over the entire nuclear envelope	82
5.19	Annular structure of the gp210 protein within the nuclear pore complex	83
6.1	Transfer of the detection point by intermediate optical lenses	89

List of Tables

2.1	Solid angle and PSF characteristics for different NA	23
5.1	Results for tracking $\varnothing = 200$ nm beads	69
5.2	Results for tracking $\varnothing = 45$ nm beads	70

Bibliography

1. Verdet, M. E. *Leçons d'optique physique* (Victor Masson et fils, Paris, 1869).
2. Abbe, E. Beiträge zur Theorie des Mikroskops und der mikroskopischen Wahrnehmung. *Archiv für mikroskopische Anatomie* **9**, 413–468 (1873).
3. S., L. R. S. R. XV. On the theory of optical images, with special reference to the microscope. *Philosophical Magazine Series 5* **42**, 167–195 (1896).
4. Hell, S. W. & Stelzer, E. H. K. Fundamental improvement of resolution with a 4Pi-confocal fluorescence microscope using two-photon excitation. *Opt. Commun.* **93**, 277–282. ISSN: 0030-4018 (1992).
5. Gustafsson, M. G. L., Agard, D. A. & Sedat, J. W. Sevenfold improvement of axial resolution in 3D wide-field microscopy using two objective lenses. *Proc. SPIE* **2412**, 147–156 (1995).
6. Hell, S. W. Microscopy and its focal switch. *Nat. Methods* **6**, 24–32. ISSN: 1548-7105 (2009).
7. Hell, S. W. & Wichmann, J. Breaking the diffraction resolution limit by stimulated emission: stimulated-emission-depletion fluorescence microscopy. *eng. Opt. Lett.* **19**, 780–782 (1994).
8. Heintzmann, R., Jovin, T. M. & Cremer, C. Saturated patterned excitation microscopy – a concept for optical resolution improvement. *J. Opt. Soc. Am. A* **19**, 1599–1609 (2002).
9. Gustafsson, M. G. L. Nonlinear structured-illumination microscopy: Wide-field fluorescence imaging with theoretically unlimited resolution. *Proc. Natl. Acad. Sci. U. S. A.* **102**, 13081–13086 (2005).
10. Hell, S. W. Toward fluorescence nanoscopy. *Nat. Biotechnol.* **21**, 1347–1355. ISSN: 1087-0156 (2003).
11. Donnert, G. *et al.* Macromolecular-scale resolution in biological fluorescence microscopy. *Proc Natl Acad Sci U S A* **103**, 11440–11445 (2006).

Bibliography

12. Betzig, E. *et al.* Imaging Intracellular Fluorescent Proteins at Nanometer Resolution. *Science* **313**, 1642–1645 (2006).
13. Rust, M. J., Bates, M. & Zhuang, X. Sub-diffraction-limit imaging by stochastic optical reconstruction microscopy (STORM). *Nat. Methods* **3**, 793–796. ISSN: 1548-7105 (2006).
14. Geisler, C. *et al.* Resolution of $\lambda/10$ in fluorescence microscopy using fast single molecule photo-switching. *Appl. Phys. A: Mater. Sci. Process.* **88**, 223–226. ISSN: 1432-0630 (June 2007).
15. Foelling, J. *et al.* Fluorescence nanoscopy by ground-state depletion and single-molecule return. *Nat. Methods* **5**, 943–945. ISSN: 1548-7105 (2008).
16. Badieirostami, M., Lew, M. D., Thompson, M. A. & Moerner, W. E. Three-dimensional localization precision of the double-helix point spread function versus astigmatism and biplane. *Applied Physics Letters* **97**, 161103 (2010).
17. Aquino, D. *et al.* Two-color nanoscopy of three-dimensional volumes by 4Pi detection of stochastically switched fluorophores. *Nature Methods* **8**, 353–359. ISSN: 1548-7105 (2011).
18. Dertinger, T., Colyer, R., Iyer, G., Weiss, S. & Enderlein, J. Fast, background free, 3D super-resolution optical fluctuation imaging (SOFI). *Proc. Natl. Acad. Sci. U. S. A.* **106**, 22287–22292. ISSN: 1091-6490 (2009).
19. Keller, J., Schönle, A. & Hell, S. W. Efficient fluorescence inhibition patterns for RESOLFT microscopy. *Opt. Express* **15**, 3361–3371 (6 2007).
20. Harke, B., Ullal, C., Keller, J. & Hell, S. W. Three-Dimensional Nanoscopy of Colloidal Crystals. *Nano Lett.* **8**, 1309–1313 (May 2008).
21. Huang, B., Wang, W., Bates, M. & Zhuang, X. Three-Dimensional Super-Resolution Imaging by Stochastic Optical Reconstruction Microscopy. *Science* **319**, 810–813 (Feb. 2008).
22. Pavani, S. R. P. *et al.* Three-dimensional, single-molecule fluorescence imaging beyond the diffraction limit by using a double-helix point spread function. *Proc Natl Acad Sci U S A* **106**, 2995–2999 (Mar. 2009).
23. Juetten, M. F. *et al.* Three-dimensional sub-100 nm resolution fluorescence microscopy of thick samples. *Nat. Methods* **5**, 527–529 (June 2008).

24. Shtengel, G. *et al.* Interferometric fluorescent super-resolution microscopy resolves 3D cellular ultrastructure. *Proceedings of the National Academy of Sciences of the United States of America* **106** (Mar. 2009).
25. Huang, F. *et al.* Ultra-High Resolution 3D Imaging of Whole Cells. *Cell* **166**, 1028–1040 (Aug. 2016).
26. Valeur, B. & Berberan-Santos, M. N. *Molecular Fluorescence: Principles and Applications* 2nd (Wiley-VCH Verlag, 2013).
27. *Handbook of Biological Confocal Microscopy* 3rd (ed Pawley, J.) (Springer, 2006).
28. Lee, S.-H., Shin, J. Y., Lee, A. & Bustamante, C. Counting single photoactivatable fluorescent molecules by photoactivated localization microscopy (PALM). *Proc. Natl. Acad. Sci. U. S. A.* **109**, 17436–17441. ISSN: 1091-6490 (Oct. 2012).
29. Voliani, V. *et al.* Cis-Trans Photoisomerization of Fluorescent-Protein Chromophores. *J. Phys. Chem. B* **112**, 10714–10722 (2008).
30. Belov, V. N. *et al.* Masked Rhodamine Dyes of Five Principal Colors Revealed by Photolysis of a 2-Diazo-1-Indanone Caging Group: Synthesis, Photophysics, and Light Microscopy Applications. *Chem Eur J* **20**, 13162–13173 (2014).
31. Van de Linde, S. *et al.* Photoinduced formation of reversible dye radicals and their impact on super-resolution imaging. *Photochem. Photobiol. Sci.* **10**, 499–506. ISSN: 1474-9092 (2011).
32. Lukyanov, K. A., Chudakov, D. M., Lukyanov, S. & Verkhusha, V. V. Photoactivatable fluorescent proteins. *Nat. Rev. Mol. Cell Biol.* **6**, 885–890 (2005).
33. Fernández-Suárez, M. & Ting, A. Y. Fluorescent probes for super-resolution imaging in living cells. *Nat. Rev. Mol. Cell Biol.* **9**, 929–943 (2008).
34. Shroff, H., Galbraith, C. G., Galbraith, J. A. & Betzig, E. Live-cell photoactivated localization microscopy of nanoscale adhesion dynamics. *Nature Methods* **5**, 417–423. ISSN: 1548-7105 (2008).
35. Dempsey, G. T., Vaughan, J. C., Chen, K. H., Bates, M. & Zhuang, X. Evaluation of fluorophores for optimal performance in localization-based super-resolution imaging. *Nat. Methods* **8**, 1027–1036. ISSN: 1548-7091 (Dec. 2011).

Bibliography

36. Backlund, M. P., Lew, M. D., Backer, A. S., Sahl, S. J. & Moerner, W. E. The Role of Molecular Dipole Orientation in Single-Molecule Fluorescence Microscopy and Implications for Super-Resolution Imaging. *ChemPhysChem* **15**, 587–599 (Mar. 2014).
37. Richards, B. & Wolf, E. Electromagnetic Diffraction in Optical Systems. II. Structure of the Image Field in an Aplanatic System. *Proc. R. Soc. A* **253**, 358–379. ISSN: 1471-2946 (Dec. 1959).
38. Goodman, J. *Introduction to Fourier Optics* 2nd (McGraw-Hill, 1996).
39. Born, M. & Wolf, E. *Principles of Optics* 7th (Cambridge University Press, 1999).
40. Hess, S. T., Girirajan, T. P. K. & Mason, M. D. Ultra-High Resolution Imaging by Fluorescence Photoactivation Localization Microscopy. *Biophys. J.* **91**, 4258–4272. ISSN: 0006-3495 (2006).
41. Heilemann, M. *et al.* Subdiffraction-Resolution Fluorescence Imaging with Conventional Fluorescent Probes. *Angew. Chem., Int. Ed.* **47**, 6172–6176. ISSN: 1521-3773 (2008).
42. Geisler, C. *Fluorescence nanoscopy in three dimensions* PhD thesis (Georg-August-University Göttingen, 2009).
43. Van Vliet, L. J., Sudar, D. & Young, I. T. in *Cell Biology: A Laboratory Handbook* (ed Celis, J. E.) 109–120 (Academic Press, 1998).
44. Robbins, M. S. & Hadwen, B. J. The Noise Performance of Electron Multiplying Charge Coupled Devices. *IEEE Transactions on Electron Devices* **50**, 1227–1232 (May 2003).
45. Thompson, R. E., Larson, D. R. & Webb, W. W. Precise Nanometer Localization Analysis for Individual Fluorescent Probes. *Biophysical Journal* **82**, 2775–2783. ISSN: 0006-3495 (2002).
46. Huang, F. *et al.* Ultra-High Resolution 3D Imaging of Whole Cells. *Cell* **166**, 1028–1040 (4 Aug. 2016).
47. Bronstein, I. N., Semendjajew, K. A., Musiol, G. & Mühlig, H. *Taschenbuch der Mathematik* 6th (Harri Deutsch, 2005).
48. Egner. *Punktabbildungsfunktion von Objektiven hoher Apertur beim Fokussieren durch eine Grenzschicht* diploma thesis (Ruprecht-Karls-University Heidelberg, 1997).

49. Nelson, P. *Biological Physics: Energy, Information, Life* 1. ed. (W.H. Freeman and Company, 2004).
50. Saxton, M. Single-particle tracking: the distribution of diffusion coefficients. *Biophys. J.* **72**, 1744–1753 (4 1997).
51. Prescher, J. *Assembly and optimization of a super-resolution STORM microscope for nanoscopic imaging of biological structures* PhD thesis (Ludwig-Maximilians-Universität Munich, 2016).
52. Olivier, N., Keller, D., Göny, P. & Manley, S. Resolution doubling in 3D-STORM imaging through improved buffers. *PLoS One* **8** (July 2013).
53. Lide, D. R. *CRC Handbook of Chemistry and Physics* 84th (CRC Press, 2003).
54. Lagarias, L. C., Reeds, J. A., Wright, M. H. & Wright, P. E. Convergence Properties of the Nelder-Mead Simplex Method in Low Dimensions. *SIAM J Optim* **9**, 112–147 (1998).
55. Geisler, C. *et al.* Drift estimation for single marker switching based imaging schemes. *Opt. Express* **20**, 7274. ISSN: 1094-4087 (2012).
56. Cooper, G. M. *The Cell, 2nd edition* ISBN: 0-87893-106-6 (Boston University, 2000).
57. Schmidt, R. *et al.* Spherical nanosized focal spot unravels the interior of cells. *Nature Methods* **5**, 539–544. ISSN: 1548-7105 (2008).
58. Loschberger, A. *et al.* Super-resolution imaging visualizes the eightfold symmetry of gp210 proteins around the nuclear pore complex and resolves the central channel with nanometer resolution. *J. Cell Sci.* **125**, 570–575 (Feb. 2012).
59. Göttfert, F. *et al.* Coaligned Dual-Channel STED Nanoscopy and Molecular Diffusion Analysis at 20 nm Resolution. *Biophys. J.* **105**, L01–L03 (2013).
60. Cordes, V. C., Gajewski, A., Stumpp, S. & Krohne, G. Immunocytochemistry of annulate lamellae: potential cell biological markers for studies of cell differentiation and pathology. *Differentiation* **58**, 307–312 (1995).

Acknowledgments

Many people have contributed to the writing of this dissertation and I would like to express my sincere thanks to them.

First of all I would like to thank PD Dr. Alexander Egner as my supervisor, referee and source of ideas. You have given me a lot of freedom and confidence when dealing with this topic. In case of questions and problems you were always on the spot and helped me very constructively.

Many thanks also to Prof. Dr. Jörg Enderlein as co-referee for the discussions and the provision of laboratory resources.

I would like to thank Prof. Dr. Hans Hofsäss, Prof. Dr. Wolfram Kollatschny, Dr. Florian Rehfeldt and Prof. Dr. Tim Salditt as further members of the examination committee for their interest in the topic and the investment of time and effort.

Many thanks also go to Dr. Claudia Geisler for all the help with processing and writing the thesis as well as to all colleagues in optical nanoscopy for the good working environment. Here I would like to emphasize Dr. David Köhne as my office colleague, you have always brought me joy and motivation into the physical environment.

Finally, I would like to thank my beloved wife Angela and my family for their support and patience on the long road to my doctorate.

Eidesstattliche Erklärung

Hiermit erkläre ich, dass ich die vorliegende Arbeit selbstständig angefertigt, nicht anderweitig zu Prüfungszwecken vorgelegt und keine anderen als die angegebenen Hilfsmittel verwendet habe. Sämtliche wissentlich verwendeten Textausschnitte, Zitate oder Inhalte anderer Verfasser wurden ausdrücklich als solche gekennzeichnet.

Haugen Mittelstädt

Curriculum Vitae

Personal Information

Name: Haugen Mittelstädt, né Grefe
Date of birth: 02. April 1985
Place of birth: Martfeld, Germany
Nationality: German

Academic Career

since 03/2013 Doctorate student at the Georg-August-University Göttingen
Research is performed at the Laser-Laboratorium Göttingen e.V.

10/2009 – 11/2012 Master of Science in Physics
University Bremen, Germany

10/2005 – 10/2008 Bachelor of Science in Physics
University Bremen, Germany